DISSERTATION

THE RESPONSE OF A SIMULATED MESOSCALE CONVECTIVE SYSTEM TO INCREASED AEROSOL POLLUTION

Submitted by

Michal Clavner

Department of Atmospheric Science

In partial fulfillment of the requirements

For the Degree of Doctor of Philosophy

Colorado State University

Fort Collins, Colorado

Spring 2016

Doctoral Committee:

Advisor: William R. Cotton
Co-Advisor: Susan C. van den Heever

Sonia M. Kreidenweis
Steven C. Reising
Thomas Birner

ABSTRACT

THE RESPONSE OF A SIMULATED MESOSCALE CONVECTIVE SYSTEM TO INCREASED AEROSOL POLLUTION

Mesoscale Convective Systems (MCSs) are important contributors to rainfall in the High Plains of the United States and elsewhere in the world. MCSs are also producers of severe weather such as hail, tornados and wide-spread straight-line wind events known as derechos. It is therefore of interest to understand how different aerosols serving as cloud condensation nuclei (CCN) concentrations may impact these systems. This work focuses on the impacts of aerosols on the total precipitation amount, rates and spatial distribution of precipitation produced by an MCS, as well as the characteristics of a derecho event. Past studies have shown that the impacts on MCS-produced precipitation to changes in aerosol concentration are strongly dependent on environmental conditions, primarily humidity and environmental wind shear. Changes in aerosol concentrations were found to alter MCS-precipitation production directly by modifying precipitation processes and indirectly by affecting the efficiency of the storm's self-propagation. Observational and numerical studies have been conducted that have examined the dynamics responsible for the generation of widespread convectively-induced windstorms, primarily focusing on environmental conditions and the MCS features that generate a derecho event. While the sensitivity of the formation of bow-echoes, the radar signature associated with derecho events, to changes in microphysics has been examined, a study on a derecho-producing MCS characteristics to aerosol concentrations has not. In this study different aerosol concentrations and their effects on precipitation and a derecho produced by an MCS are examined by simulating the 8 May 2009 "Super-Derecho" MCS. The MCS was simulated using the Regional

Atmospheric Modeling System (RAMS), a cloud-resolving model (CRM) with sophisticated aerosol and microphysical parameterizations. Three simulations were conducted that varied in their initial aerosol concentration, distribution and hygroscopicity as determined by their emission sources. The first simulation contained aerosols from only natural sources and the second with aerosols sourced from both natural and anthropogenic emissions The third simulation contained the same aerosol distribution as in the second simulation, however multiplied by a factor of 5 in order to represent a highly polluted scenario. In all three of the simulations aerosol concentrations were derived from the output of GEOS-Chem, a 3D chemical transport model.

In the simulated MCS, the formation and propagation of the storm was not fundamentally modified by changes in the aerosol concentration, and the total MCS-produced precipitation was not significantly affected. However, the precipitation distribution (convective vs stratiform) and derecho-strength surface wind characteristics did vary among the simulations. The more polluted simulations exhibited higher precipitation rates, higher bulk precipitation efficiency, a larger area with heavier convective precipitation and a smaller area with lighter stratiform precipitation. These differences arose because aerosol pollution enhanced precipitation in the convective region while suppressing precipitation from the stratiform-anvil.

Higher aerosol concentrations led to the invigoration of convective updrafts which supported the formation of larger rain drops, and lofted more liquid cloud mass to higher levels, thereby increasing both collision-coalescence and riming processes. The presence of greater aerosol concentrations in the free troposphere, as well as in the boundary layer, reduced both collision-coalescence and riming within the stratiform-anvil region. As a consequence, the more polluted simulations produced the smallest precipitation from the MCS stratiform-anvil region.

In order to understand the impact of changes in aerosol concentrations on the derecho characteristics, the dynamical processes which produced the strong surface wind were determined by performing back-trajectory analysis during different periods of the simulated storm. The analysis showed that two main air flows contributed to the formation of the derecho winds at the surface; a rear-inflow jet and an up-down downdraft associated with a mesovortex at the gust font. The changes in aerosol concentrations impacted the simulated derecho event by altering the main flow contributing to the formation of the derecho winds though the amount of melting and evaporation of hydrometeors. Earlier in the storm, changes in melting and evaporation altered the intensity of the storm-produced cold pool. This, in turn, modified the balance between the horizontal relative vertical vorticity generated by the cold pool and that of the low-level environmental shear. The smaller hail and rain hydrometeors in the cleaner simulation exhibited higher melting and evaporation rates due to the larger surface area, which contributed to the formation of a stronger cold pool and led to the tilting of the convective updraft upshear. This, in turn, shifted the flow associated with the derecho event to be predominantly from a Rear-Inflow Jet (RIJ). An increase in aerosol concentration led to a weaker cold pool and therefore an upright convective updraft which promoted the formation of a stronger mesovortex, and subsequently shifting the flow to be predominantly from strong downdrafts following an up-down downdraft (UDD) trajectory. The shift from a RIJ flow to a UDD led to stronger surface winds over a smaller area. As the storm matured, the derecho winds were found to be associated with the formation of a mesovortex at the gust front. At this time, a non-linear trend between aerosol concentrations to derecho intensity was apparent and was attributed to the non-linear trend in mesovortex strength.

ACKNOWLEDGMENTS

I would like to thank Dr. William Cotton for giving me the opportunity to continue my studies in atmospheric science, introducing me to the world of modeling and guiding me through this project. I would also like to thank Dr. Susan van den Heever for her ongoing advice and guidance throughout my studies and research.

Dr. Lewis Grasso, who developed the back-trajectory model used in this study, provided suggestions regarding modeling and model syntax as well as encouraged me to find solutions by thinking outside the box. Thank you to Dr. Jeffery Pierce for the GEOS-Chem aerosol data used in this study and the input on how to activate aerosols within the model. I would like to thank Stephen Saleeby for his input regarding in getting RAMS to work and behave and also for implementing the heterogeneous soil moisture scheme used in this study. Thank you to Dr. Gustavo Carrio for his patience and advice on numerical simulations. This work would not be possible without Ammon Redman and Matthew Bishop, who saved my computer from certain death on several occasions, helped me juggle tens of terabytes of data from computer to computer and were always available to help out when needed.

I am also grateful to Drs. Sonia M. Kreidenweis, Steven C. Reising and Thomas Birner for serving on my committee. Thank you to the Cotton and van den Heever research groups for their support, input and moral, which made getting segmentation faults a little less painful. Finally, I would like to thank my husband, Yan Berk, for all his support and always being up to drive around to chase clouds. This work was funded by the National Science Foundation under grant AGS-1005041.

DEDICATION

This dissertation is dedicated to my mother, Hannah R. Clavner,

for her encouragement, support, and love.

TABLE OF CONTENTS

1. Introduction

Mesoscale convective systems (MCS) are the largest form of convective storms around the globe and are an important link between atmospheric convection and the larger-scale atmospheric circulation (Houze, 2004). An MCS is defined as a complex of thunderstorms organized on a scale larger than an individual thunderstorm, ranging in size from meso-β (20-200km) systems (Jirak et al., 2003) to the scale of a Mesoscale Convective Complex (MCC), the largest form of MCS (Maddox, 1980). Climatological studies have shown that MCSs are important contributors to regional rainfall and it has been observed that annual variation of MCS events impact the total annual rainfall producing regional conditions ranging from drought to flooding events (Fritsch et al., 1986; Anderson and Arritt, 1998, 2001). MCS storms are also producers of severe weather such as flash flooding, hail, tornadoes and severe wide-spread straight-line winds, known as Derechos (Maddox, 1980; Johns and Hirt, 1987).

MCSs have been a topic of ongoing research since the late 1970's. The focus of such research has been on the environmental conditions which support the evolution of MCS (e.g. Maddox, 1983), the evolution of the storms with time (e.g Cotton et al., 1989), the division of an MCS into convective and stratiform regions (e.g Leary and Houze, 1979) and the environmental conditions supporting the formation of severe weather (e.g Johns and Hirt 1987). Numerous numerical studies have examined the sensitivity of MCSs intensity, characteristics and longevity to both environmental conditions and the interaction between the storm generated flow and the environment (Rotunno et al., 1988). Furthermore, studies have investigated the sensitivity of MCS storms to changes in aerosol concentrations impacting both precipitation and storm longevity (Khain et al., 2005; Tao et al., 2007; Li et al., 2009; Seigel et al., 2013). Since MCSs are prolific producers of precipitation, the impact of changes in aerosol concentration on MCS-

produced precipitation is a topic of continuous research, primarily, the division of precipitation characteristics into convective and stratiform precipitation (e.g. Johnson and Hamilton, 1988). The heaviest precipitation produced by an MCS was found to occur in areas of meso-β scale intense convection embedded within the MCS (McAnelly and Cotton, 1986) and stratiform precipitation can account for ~30-45% of the storm produced precipitation, depending on the storm's environment (Tao et al., 1993; Alexander and Cotton, 1998). The partitioning of the storm's precipitation into convective and stratiform characteristics has been found to be sensitive to aerosol loading serving as cloud condensation nuclei (CCN), giant CCN (GCCN) and ice nuclei (IN). Precipitation formation processes were found to change directly due to the microphysical effect of aerosol loading on precipitation formation (Lynn et al., 2005; Seigel et al., 2013) and indirectly by modifying the storm self-propagation efficiency (Tao et al., 2007; Li et al., 2009; Lebo and Morrison, 2014).

The sensitivity of the characteristics of an MCS-produced severe wind event, such as a derecho, to aerosol loading has not yet been directly studied, however, past studies have found dynamical features associated with the formation of strong surface winds to be sensitive to ice microphysics. The radar signature of an MCS associated with strong surface winds was identified and named "bow-echo" by Fujita (1978) due to the bowed characteristic of the radar reflectivity. A bow-echo pattern evolves as a strong convective downdraft reaches the surface and creates a strong outflow which pushes the convective cells forward. For this reason, the apex of the bow signifies the location of the strongest winds (Fujita, 1978). Dynamical contributors to strong surface outflow include both strong downdrafts due to negative buoyancy created by evaporation of precipitation and the transfer of high momentum air to the boundary layer (Newton, 1950) by the rear inflow jet (RIJ) (Smull and Houze, 1987). The dynamical

characteristics of a storm, such as downdraft intensity, the formation of a bow-echo and the strength of the RIJ were found to be sensitive to ice microphysics. Changes in hail size (van den Heever and Cotton, 2004) can alter downdraft intensity and cold pool depth, the structure of a simulated bow-echo can depend on the changes within the ice microphysical scheme of the model (Adams-Selin et al., 2013) and the intensity of the RIJ was found to be sensitive to ice microphysics (Yang and Houze, 1995).

This dissertation is a numerical simulation study that examines the impact of changes in aerosol concentrations on a case study MCS and is divided into two sections. Chapter 2 examines the response of the MCS-produced precipitation intensity, distribution and efficiency to increased pollution. Chapter 3 examines the sensitivity of the simulated derecho event to changes in aerosol concentrations. Chapters 2 and 3 constitute a two part manuscript: Part I and Part II, respectively, to be submitted to the Journal of Atmospheric Research. A summary of the research and the results are given in Chapter 4.

2. The response of a simulated mesoscale convective system to increased aerosol pollution: Part I: Precipitation intensity, distribution and efficiency.

2.1. Introduction

An MCS is a complex of thunderstorms organized on a larger scale that have a shared stratiform-anvil (Cotton et al., 2010). MCSs can range in size from a multicellular thunderstorm having three or four cells to a Mesoscale Convective Complex (MCC), the largest form of MCSs (Cotton et al. 2010). Maddox (1980) defined an MCC as a long-lived circular MCS with specific characteristics according to infrared satellite imagery. Maddox's (1980) definition of an MCC is an MCS which (1) exhibits a cloud top temperature colder than -52^{o}C over an area exceeding 50,000 km^{2}, (2) that is embedded within a larger area of 100,000 km^{2} with cloud top temperatures colder than -32^{o}C, (3) these specifications need to be upheld for at least 6 hours, and (4) the MCS must exhibit an eccentricity of at least 0.7 at the time of maximum extent. Seeking a more dynamically based definition of an MCC, Cotton et al., 1989 and later Olsson and Cotton (1997a, 1997b), concluded that a mature MCC "represents an MCS that is in a nearly balanced dynamical state and whose horizontal scale is comparable to or greater than a locally defined Rossby radius of deformation".

Previous studies showed that MCS development, intensity and precipitation is dependent on environmental conditions such as the low level jet (LLJ) (Maddox, 1983), vertical wind shear (Rotunno et al., 1988), convective available potential energy (CAPE), and moisture (Tao et al. 1993). Only in recent years have numerical simulation studies examined the impacts of changing aerosol concentrations on MCS intensity and the precipitation produced by these systems. It has been found that increased concentrations of potential cloud condensation nuclei (CCN) can

impact MCS intensity, propagation and precipitation via their impacts on the microphysical processes and, in turn, the dynamical feedbacks to the system (Khain et al., 2005; Tao et al., 2007; Li et al., 2009;Seigel et al., 2013; Lebo and Morrison, 2014). Numerical simulations have suggested an increase in mid-latitude MCS-produced precipitation in a more polluted environment due to the enhancement of cold precipitation processes such as ice vapor deposition and riming (Khain et al., 2005), convective invigoration of the updrafts, and the production of larger rain drops which survived evaporation more readily below cloud base (Li et al., 2009). For a given amount of liquid water content, increased potential CCN concentrations nucleate more numerous and smaller cloud droplets (Twomey, 1974, 1977) leading to a suppression of warm rain formation by collision coalescence (Albrecht, 1989). In turn, more cloud water is lofted to higher levels and cold precipitation production is enhanced, thereby invigorating the convective updraft due to the latent heat release of freezing of supercooled drops, vapor deposition growth of ice particles, and riming (Andreae et al., 2004; van den Heever et al., 2006). Furthermore, enhanced riming within stronger updrafts produces larger hailstones which are found to shed more numerous and larger raindrops, contributing to the surface precipitation (Storer et al., 2010).

The effect of increased concentrations of potential CCN on MCS precipitation have been found to be dependent on environment conditions such as humidity (Khain et al., 2005; Tao et al., 2007) and vertical wind shear (Lebo and Morrison, 2014) due to the microphysical effects of increased aerosols and its dynamical feedback on the storm intensity. Furthermore, the impact of higher aerosol concentration on precipitation production from an MCS was found to be dependent also on the type of aerosol and its chemistry, size and distribution. For example, using only mineral dust as an aerosol, Seigel et al. (2013) identified a time dependent

precipitation response to an increase in aerosol concentration. This was attributed to the bi-modal nature of the dust distribution, whereby, the smaller mode served as CCN while the coarser mode served as Giant CCN (GCCN) and Ice Nuclei (IN). During the first couple of hours of the MCS simulation, the presence of dust increased the precipitation due to presence of dust serving as GCCN, thus, enhancing warm rain production by collision-coalescence. However, the early rainout led to a reduction of supercooled water aloft which reduced the riming rates and the contribution of riming to the latent heat release. This, in turn, led to weaker updrafts, suppressed convective mass flux, and a reduction in total precipitation.

In this study, we seek additional insight into the impact of enhanced CCN concentrations on a mid-latitude MCS by investigating a MCC-like MCS case study using a 3D model configuration in which GEOS-Chem (Bey et al., 2001) estimates of aerosol concentrations are utilized. The case chosen for this study is the 8 May 2009 "Super Derecho" MCS and has been analyzed in several past papers (Przybylinksi et al. 2010; Coniglio et al. 2011; Coniglio et al. 2012; Keene & Schumacher 2013; Weisman et al. 2013; Evans et al. 2014; Xu et al. 2015a; Xu et al. 2015b). However, none of these studies examined the potential sensitivity of the storm characteristics to changes in aerosol concentrations. This study adds to the current body of work by examining the impacts of increased aerosol concentrations on the precipitation production of the 8 May 2009 MCS. The case study is described in Section 2.2. The numerical model set up and aerosols serving as CCN in this study are described in Sections 2.3.1 and 2.3.2, respectively. The results of changing aerosol concentration on the precipitation produced by the case study storm are presented in Section 2.4. In Part II the impact of aerosols on the severe winds produced by this storm is examined.

2.2 Case Study- The 8th May 2009 MCS

The 8 May 2009 event has been characterized in previous studies (Coniglio et al., 2011; Weisman et al., 2013) as a leading-line, trailing stratiform (Houze et al., 1989; Parker and Johnson, 2000) bow-echo (Fujita, 1978) MCS which developed a warm-core meso-β-scale vortex in its later stage (Weisman et al., 2013; Evans et al., 2014). The MCS developed in western Kansas and moved south-southeastward to the southern Appalachians, traveling over a thousand miles in under 24 hours (Coniglio et al. 2011; Storm Prediction Center (SPC)). Further details of the environment of the 8 May 2009 MCS and the evolution of the storm can be found in previous studies (Coniglio et al., 2011;Keene and Schumacher, 2013; Weisman et al., 2013).

In order to determine the MCS lifespan (genesis, mature, decay) and the convective structure of the MCS, satellite infrared cloud top temperature from the Geostationary Operational Environmental Satellite 12 (GOES-12) imagery and Weather Surveillance Radar, 1988, Doppler (WSR-88D) mosaic radar images of composite reflectivity were analyzed (Figure 2.1). The first convective clouds prior to the MCS genesis stage occurred on May 8 shortly after 0300 UTC along the eastern slopes of the Rockies, which is a common location for MCS genesis in the High Plains of the United States (Cotton et al., 1983; Maddox, 1983; Velasco and Fritsch, 1987; Augustine and Caracena, 1994). The initial convective clouds then propagated eastward into Kansas, into a region with high precipitable water (PW), which was found to be anomalously high in comparison to other mid-latitude MCS environments (Coniglio et al., 2011). The region of high PW (>30 kg m^{-2}), which at first is confined to eastern Kansas, grew in extent and covered most of Kansas by 0600 UTC, most likely in association with the formation of the LLJ (Figure 2.2) that supplied the region with moisture as well as appropriate wind shear.

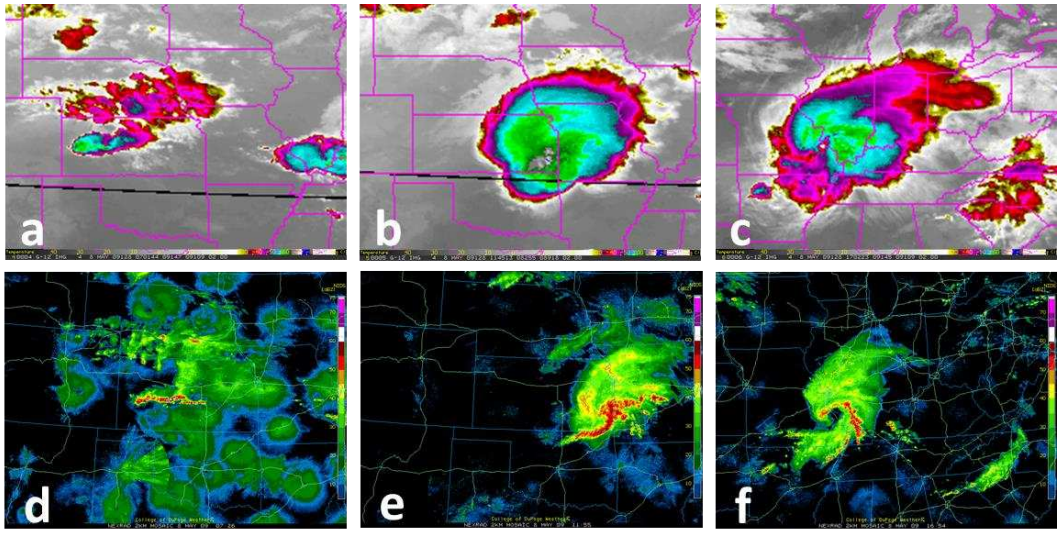

Figure 2.1: Top: Satellite infrared cloud top temperature from the Geostationary Operational Environmental Satellite 12 (GOES-12) at 0701 UTC (a), 1145 UTC (b) and 1702 UTC(c). Bottom: Weather Surveillance Radar, 1988, Doppler (WSR-88D) mosaic radar images of composite reflectivity at 0726 UTC (d), 1155 UTC (e) and 1654 UTC (f).

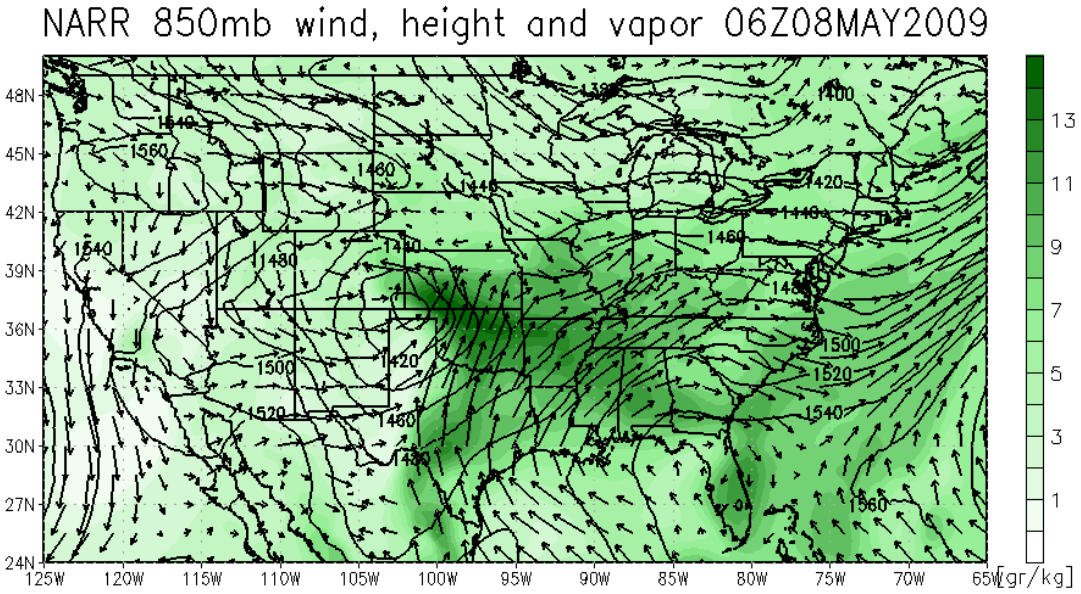

Figure 2.2: NARR 850 mb plot of horizontal wind (vectors) geopotential heights [m] (black contours) and specific humidity [g kg^{-1}] (shaded) for 8 May 2009 at 0000 UTC.

By 0700 UTC (Figure 2.1a) the individual convective cells merged and deepened, signifying the genesis stage of the MCS (McAnelly & Cotton 1986). The orientation of the initial MCS convection (Figure 2.1d) was on the cold side of a surface boundary, also a common characteristic in an MCS environment (Cotton et al., 1989; Maddox, 1983).

During the next several hours the storm progressed eastwards while it grew in size both horizontally and in depth, and entered Missouri by 1000 UTC. The storm's size was at its maximum at ~1200 UTC (Figure 2.1b), signifying the storm's mature stage (Maddox 1983). It was during this time when the MCS exhibited a pronounced bow echo (Figure 2.1e). As the storm exited Missouri at ~1700 UTC, the cloud top temperatures began to increase indicating that the convective cells within the MCS were beginning to dissipate (Figure 2.1c). From the analysis of the IR imagery, the 8 May 2009 MCS embodies MCC-like characteristics by being more circular than linear; however, it does not exhibit a defined inner core of temperatures below -52C, and therefore does not comply with Maddox's criteria for a classic MCC.

The observed precipitation from the 8 May 2009 MCS was assessed according to the National Weather Service Advanced Hydrological Prediction Service (NWS-AHPS) River Forecast Centers (RFCs) gridded observation of accumulated 24 hour precipitation [mm]. Data from 7 May 1200 UTC until 9 May 1200 UTC were plotted in order to capture the precipitation produced by the 8 May MCS (Figure 2.3). The 8 May MCS produced large amounts of precipitation in both Kansas and Missouri, with areas receiving up to 115 mm of accumulated precipitation (Figure 2.3). In this study we examine how changes in the environmental aerosol concentrations can alter the precipitation produced by this system. A key feature of the 8 May 2009 system was the strong straight-line winds (Derecho) (Johns and Hirt, 1987) produced by

the storm. The sensitivity of the dynamics of the 8 May 2009 MCS, specifically the derecho strength, to changes in aerosols concentrations is examined in Part II.

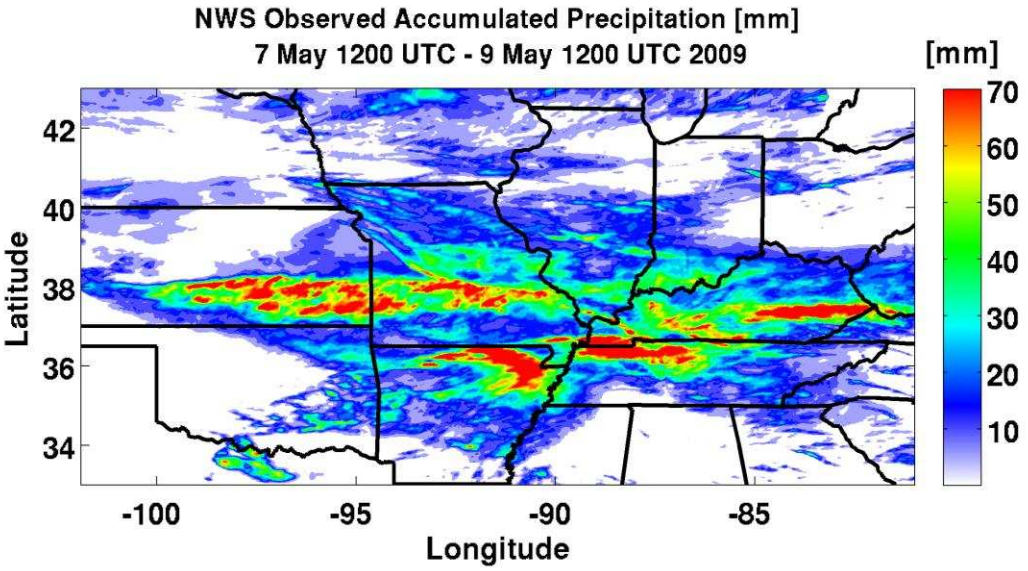

Figure 2.3: National Weather Service Advanced Hydrological Prediction Service (NWS-AHPS) River Forecast Centers (RFCs) gridded observation of accumulated 24 hour precipitation [mm] from 8 May at 1200 UTC - 9 May at 1200 UTC 2009.

2.3. Numerical Model and Experiment Setup

2.3.1. Model Configuration

The case study of the 8 May 2009 was simulated using the Colorado State University Regional Atmospheric Modeling System (RAMS) version 6 (Cotton et al., 2003; Saleeby and van den Heever, 2013). The RAMS model simulation was set up as a cloud resolving mesoscale model with three interactive model grids (Figure 2.4). Grids 1 and 2's spatial areas were determined in order to simulate the synoptic and mesoscale environments, respectively. Grid 3's spatial area covers the entire domain of the simulated MCS from genesis to decay. All three grids were set up with 55 vertical levels and a model top height extending to 19 km above ground level (AGL) with a vertical grid spacing of 50m at the lowest vertical grid level stretched to a

maximum of 500 m. The simulation duration was 24 hours from 0000 UTC May 8 2009 until 0000 UTC May 9 2009 and was initialized with North American Regional Reanalysis (NARR) data from 8 May 2009 at 0000 UTC. RAMS soil moisture in all 3 grids was also initialized with NARR surface soil moisture. Further information on the RAMS simulation set up is presented in Table 1.

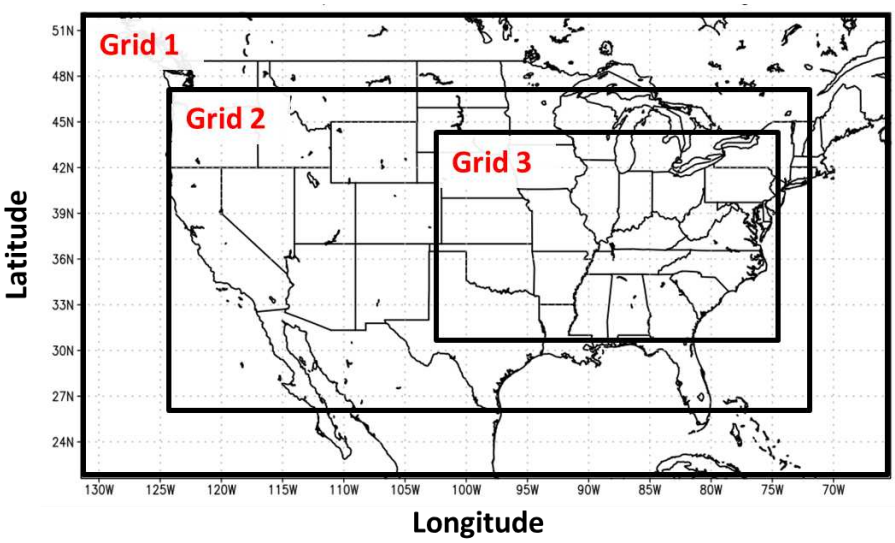

Figure 2.4: Regional Atmospheric Modeling System (RAMS) nested grid set up locations for the parent grid (Grid 1) and the nested grids: Grid 2 and 3.

RAMS uses a sophisticated two-moment, bin-emulating, bulk microphysics scheme that prognoses both mass and number concentration for eight hydrometeor classes: cloud, drizzle, rain, pristine ice, snow, aggregates, graupel, and hail (Meyers et al., 1997; Saleeby and Cotton, 2004, 2008; Saleeby and van den Heever, 2013). The RAMS microphysical scheme was set up with the option of budget tracking of microphysical processes, which is critical in analyzing the precipitation microphysics and processes within the simulation (Saleeby and van den Heever, 2013). Aerosol data from the 3D chemistry transport model, Goddard Earth Observing System Chemistry (GEOS-Chem) v9.01.03 (Bey et al., 2001) were incorporated into RAMS. The

GEOS-Chem model and GEOS-Chem simulations are described in Section 2.3.2. The implementation of GEOS-Chem aerosols as potential CCN and IN into RAMS is described in Section 2.3.3.

Table 2.1: RAMS configuration and options

Model Aspects	Settings
Grid	Arakawa C grid (Mesinger and Arakawa 1976) Three grids Horizontal grid: Grid 1: $\Delta x = \Delta y = 40$km 120x80 points Grid 2: $\Delta x = \Delta y = 8$km 507x267 points Grid 3: $\Delta x = \Delta y = 1.6$km 1422x822 points Vertical grid: 55 levels, 12 below 1 km AGL Δz=variable Minimum Δz=50m, maximum Δz= 500m Vertical stretch ratio= 1.09 Model top ≈ 19km
Time step	Grid 1: 20 s Grid 2: 10 s Grid 3: 3.33 s
Simulation durations	24 hours: 8th May 0000 UTC - 9th May 0000 UTC
Initialization	North American Regional Reanalysis (NARR)
Boundary conditions	Radiative lateral boundary (Klemp and Wilhelmson, 1978) Lateral and top model nudging from NARR
Microphysics scheme	Two-moment bulk microphysics (Meyers et al., 1997) Eight hydrometeor classes (Saleeby and Cotton, 2004) DeMott et al. (2010) ice nucleation parameterization Microphysical budget tracking (Saleeby and van den Heever, 2013)
Turbulence scheme	Smagorinsky (1963) deformation *K* closure scheme with stability modifications by Lilly (1962) and Hill (1974)
Radiation scheme	Two-stream radiation parameterization (Harrington, 1997; Harrington et al., 1999)
Surface scheme	Land Ecosystem- Atmospheric Feedback (LEAF-3) (Walko et al., 2000) with soil moisture from the NARR data
Aerosol treatment	12 aerosol species from the Goddard Earth Observing System Chemistry (GEOS-Chem)

2.3.2. GEOS-Chem Model and Simulations

GEOS-Chem is a global/regional three-dimensional chemical transport model driven by the assimilated meteorological observations from the Goddard Earth Observing System (GEOS) of the NASA Global Modeling Assimilation Office (GMAO), the GEOS-5 product. In this study, GEOS-Chem simulations were set up at 0.5°x0.667° resolution over North America. Initial and boundary conditions were generated from a global 4°x5° GEOS-Chem simulation. Both grids include 47 vertical sigma-pressure levels from the surface up to 0.01 hPa.

GEOS-Chem simulates the emission, chemical interactions, transport and removal of 64 gas and particle-phase species. Emissions fields are described in detail in Stevens and Pierce (2014). Twelve aerosol species were used in this study: three inorganic aerosols (sulfate, nitrate and ammonia) and eight organic aerosols (primary hydrophilic organic carbon, primary hydrophilic black carbon, primary hydrophobic organic carbon and primary hydrophobic black carbon as well as 5 secondary organic aerosol (SOA) groups). The SOA groups represent GEOS-Chem oxidation products of different parent hydrocarbons according to absorptive partitioning following the framework by Chung and Seinfeld (2002) and Henze et al., (2008). For this study, two GEOS-Chem simulations were performed: the first (both the global and nested simulations) with anthropogenic emissions included and the second with anthropogenic emissions turned off, thereby creating two separate aerosol concentration data sets for North America. Therefore, the first data set included aerosols from only natural emissions while the second data included emissions from both natural and anthropogenic sources. The nested North American GEOS-Chem simulation included one week of spin-up prior to May 1 2009 from the initial conditions set by the global simulation.

2.3.3. Implementation of GEOS-Chem aerosols into RAMS

GEOS-Chem model output of 8 May 2009 0000Z, corresponding to the RAMS simulation initialization time, was used in order to represent "realistic" horizontally heterogeneous aerosol concentrations with varying hygroscopicity. All 12 of the aerosol species were assumed to have a lognormal distribution with a geometric mean radius of 60 nm and a geometric standard deviation of 1.8. The twelve aerosol species were introduced into RAMS as three different internally-mixed aerosol groups based on similar aerosol hygroscopicity, represented by their Kappa value (Petters and Kreidenweis, 2007). The grouping of the twelve aerosol species into three groups was motivated by reducing the RAMS computation time while still representing different aerosols types which differ in their nucleation potential. The first group contains the inorganic aerosols (sulfate, nitrate and ammonium) and was set to have a characteristic kappa value of 0.6. The second group contains hygroscopic organic aerosols (hydrophilic black carbon, hydrophilic organic carbon and the five SOA species) with a kappa value of 0.12. The third group contains hydrophobic aerosols (hydrophobic black carbon and hydrophobic organic carbon) and has a kappa value of 0.0. The GEOS-Chem aerosol data were interpolated into each of the three RAMS grids using a three dimensional linear inverse distance weighted interpolation. Each of the aerosol groups was set to be radiatively inactive and hence, the direct effect of these aerosols was not represented in the model simulations. This configuration was chosen in order to isolate the effects of changes in aerosol quantities on cloud microphysics and on the simulated MCS dynamics and precipitation.

RAMS' two-moment, bin-emulating, bulk microphysics scheme activates aerosols to serve as CCN according to a lookup table which calculates the fraction of the aerosol concentration within a supersaturated grid volume that can serve as CCN (Saleeby and Cotton,

2004; Saleeby and van den Heever, 2013). The fraction is calculated according to five parameters: aerosol median radius, aerosol concentration, aerosol hygroscopicity (represented by kappa), as well as vertical velocity and temperature. In order to represent nucleation competition among the three aerosol groups, at the time of aerosol activation the three groups are assumed to be internally mixed and a concentration-weighted kappa is calculated. The fraction of activated aerosols from the total aerosol concentration at a given grid point is then calculated using a lookup table which was created offline using Lagrangian parcel model runs with internally mixed aerosols (Ward et al., 2010; Ward and Cotton, 2011; Letcher and Cotton, 2014). Aerosol concentrations serving as IN were based on the DeMott et al. (2010) IN activation scheme which calculates the concentration of IN based on the total number of non-sea salt aerosols greater than 0.5 micron diameter of each of the three aerosol groups, separately.

2.3.4. Experimental design: RAMS simulations

In order to examine the impact of the presence of anthropogenic aerosols concentrations and increased aerosol concentrations on the RAMS simulated case study MCS, a set of three sensitivity simulations were performed (Table 2.2). The differences among the three simulations were the GEOS-Chem aerosol concentration and spatial distribution at the time of the RAMS model initialization. The first RAMS simulation was initialized with aerosol concentrations from the GEOS-Chem simulation containing aerosols from only natural emissions (no anthropogenic sources). This RAMS simulation is labeled as the "CLEAN Simulation". The second simulation was initialized with aerosol concentrations from the GEOS-Chem containing aerosols from both anthropogenic and natural emissions. This RAMS simulation is labeled as the "POLLUTED Simulation". In order to examine a more highly polluted scenario, the third simulation was initialized with the same aerosol distribution as the RAMS POLLUTED simulation, however, the

GEOS-Chem aerosols were multiplied by a factor of five. This simulation is labeled as the "5xPOLLUTED Simulation", and was motivated by past studies which looked at the impact of increased aerosol concentration greater than 6000 cm^{-3} (Storer et al., 2010; Carrio and Cotton, 2011). A summary of the three simulations performed are presented in Table 2.2.

Table 2.2: RAMS Simulations

Simulation	Simulation Name	Characteristics
1	CLEAN	Initialized with a heterogeneous aerosol distribution using output from the GEOS-Chem simulation with only natural emissions.
2	POLLUTED	Initialized with a heterogeneous aerosol distribution using output from the GEOS-Chem simulation with both anthropogenic and natural emissions.
3	5xPOLLUTED	Initialized with GEOS-Chem aerosols with 5 times as much aerosols as in the Polluted simulation.

Figure 2.5 presents the vertical profiles of the average total aerosol concentrations [cm^{-3}] and the concentration weighted kappa value at the time of the MCS genesis (0630 UTC) in the three simulations. Since the aerosol distribution is initially horizontally heterogeneous, Figure 2.5 also shows the vertical profiles of the upper and lower 10^{th} percentile of the total aerosol concentration and estimated kappa values for each of the simulations. Differences in the aerosol distribution between the GEOS-Chem data containing both anthropogenic emission and natural emission in comparison to just natural emissions is most evident in lower levels, as the difference between the Clean and Polluted simulation's total aerosol concentrations decreases as a function of height. It is important to note that for the 5xPOLLUTED, at 0630 UTC, the aerosol concentrations were larger by a factor of 5 at all vertical levels. Surface total aerosol concentration maps of the CLEAN and POLLUTED simulation and vertical cross section along

38N (the latitude which represents the meridional location of the MCS) are given in the appendix, Figure A1. The GEOS-Chem aerosols were incorporated in all three of the RAMS grids (Figure 2.4) at the time of model initialization, after which, the only sources of aerosols are the advection of aerosols from the coarser to finer grids as well as the formation of aerosols due to the evaporation of cloud droplets.

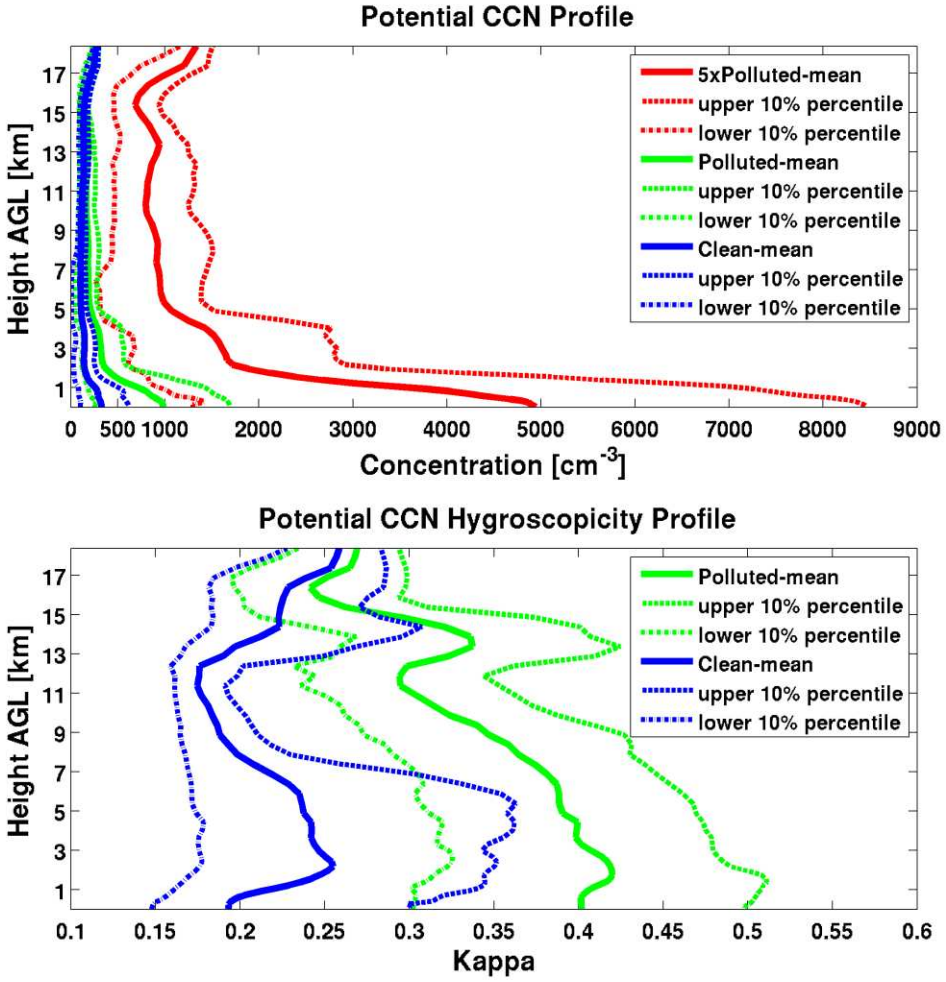

Figure 2.5: Top: Vertical profile of the mean (solid line) aerosol concentration for the three simulations at the time of the MCS genesis (0630 UTC): Clean (blue), Polluted (green) and 5xPolluted (red). Bottom: Vertical profile of the estimated concentration weighted mean (solid line) kappa values for the two simulations: Clean (blue) and Polluted (green). The 5xPOLLUTED featured the same kappa value estimates as that of the POLLUTED simulation due to the multiplication of all aerosols species by a factor of five. For both panels, the vertical profile of the upper and lower 10th percentiles are represented in the dash-dotted and dashed line, respectively.

2.4. Simulation Results

2.4.1. Isolating the Simulated MCS

In all three RAMS simulations, convective elements not associated with the MCS developed in the analyzed grid (Grid 3). In order to perform statistical analysis, such as computing the precipitation produced solely from the MCS, data from the other convective elements were numerically filtered out. The filtering technique used in this study was motivated by past studies that separated a region into cloudy and clear sky using cloud top temperature from infrared satellite imagery. Similar to Igel et al. (2014), cloud objects were identified using a binary function, labeling a continuous area of the domain as cloudy or clear according to prescribed cloud property thresholds. In this study, only cloudy pixels that could be considered a part of the MCS were of interest, therefore, a dominant criterion for labeling a grid column as cloudy was set according to cloud top temperature, a salient feature in MCSs (Maddox, 1980; Jirak et al., 2003). The filtering technique also incorporated the two dimensional parameters of precipitation rate [$mmhr^{-1}$] and vertically-integrated total condensate (VITC) [$kg\ m^{-2}$]. In this study, data analyzed from the RAMS simulated MCS were taken from MCS genesis at 0630 UTC until 1730 UTC, after which the method for isolating the MCS broke down due to the fragmented stratiform-anvil shield and close proximity of neighboring convection.

2.4.2. Comparisons with observations

VITC was analyzed in order to identify the geographic location, evolution, spatial extent and temporal timing of the simulated MCS. Plots of VITC for the three simulations (CLEAN, POLLUTED and 5xPOLLUTED) are presented for 0700 UTC, 1200 UTC and 1700 UTC (Figure 2.6).

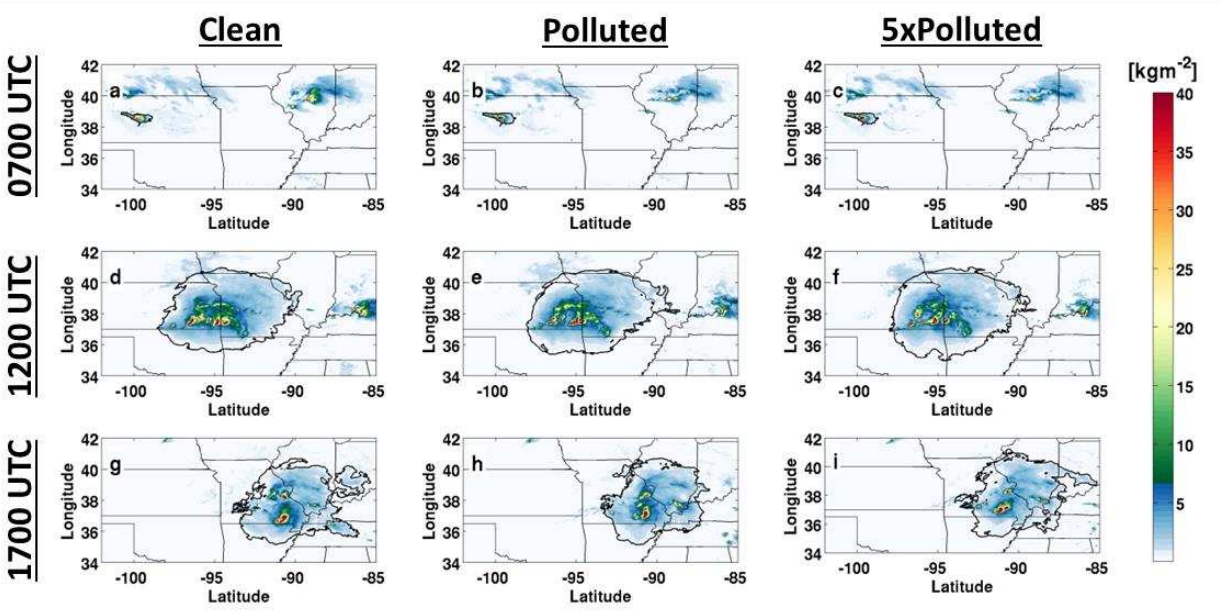

Figure 2.6: RAMS vertically integrated total condensate [kg m^{-2}] at 0700 UTC (top row), 1200 UTC (middle row) and 1700 UTC (bottom row) for the three simulations: Clean (left column), Polluted (middle column) and 5xPolluted (right column). Contoured in black is the region which is considered to be part of the MCS following the isolation guidelines described in section 2.4.1.

Qualitatively, the three simulations produced similar MCS genesis times, storm sizes, propagation locations and life spans. In all three of the simulations, MCS development occurred in western Kansas at 0630 UTC and quickly organized under a shared stratiform-anvil at 0700 UTC (Figure 2.6, top row). The convective cores exhibited a west-east orientation, similar to the observed composite radar reflectivity. As the convective cores propagated east-southeastward with time, the stratiform-anvil spread out and grew to a horizontal scale comparable to an MCC (~1200 UTC) (Figure 2.6, middle row), similar to the observed infrared satellite imagery (Figure 2.1b). At 1200 UTC, the higher VITC values, indicative of the presence of convective cores, were located in the southeastern corner of Kansas, similar to the composite radar reflectivity (Figure 2.1e). Synthetic satellite imagery has also been found to be a useful tool for validating

simulated cloud fields with observations from GOES imagery (Grasso and Lindsey, 2011; Jankov et al., 2011; Grasso et al., 2013). Synthetic imagery was produced by coupling RAMS output data with a radiative transfer numerical model in order to simulate a cloud top temperature for a given wavelength. In this study the wavelength of 10.7 μm was chosen in order to compare the synthetic satellite imagery to GOES-12 infrared cloud top temperature. Figure 2.7 presents the synthetic GOES-12 imagery at 1200 UTC from the three simulations. A comparison between the synthetic satellite imagery and the observed GEOS-12 image at 11:45 (Figure 2.1b) shows that RAMS was successful in simulating the MCSs location, size, and values of infrared cloud top temperatures. The onset of MCS dissipation occurred shortly after 1430 UTC in all three simulations as the MCS stratiform-anvil became fragmented and the MCS horizontal scale began to decrease in size (Figure 2.6, bottom row).

The simulated total accumulated precipitation from the entire analysis period for the three simulations is illustrated in Figure 2.8. All three simulations produced similar surface precipitation distributions to that observed (Figure 2.4). The heaviest accumulated precipitation occurred over central Kansas, south-central Kansas and central Missouri, coinciding with the observations.

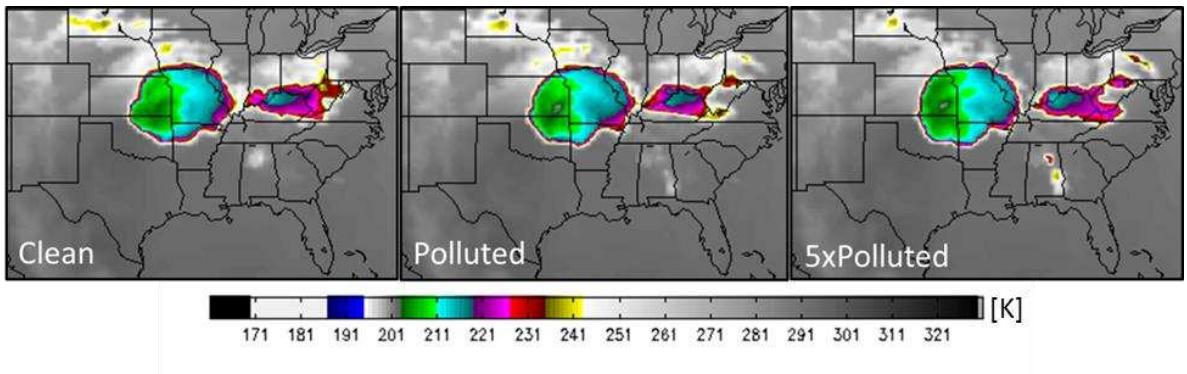

Figure 2.7: Synthetic GOES-12 Cloud top temperature imagery [K] at 10.7 μm at 1200 UTC calculated from the three RAMS model simulations: Clean (left), Polluted (middle) and 5xPolluted (right).

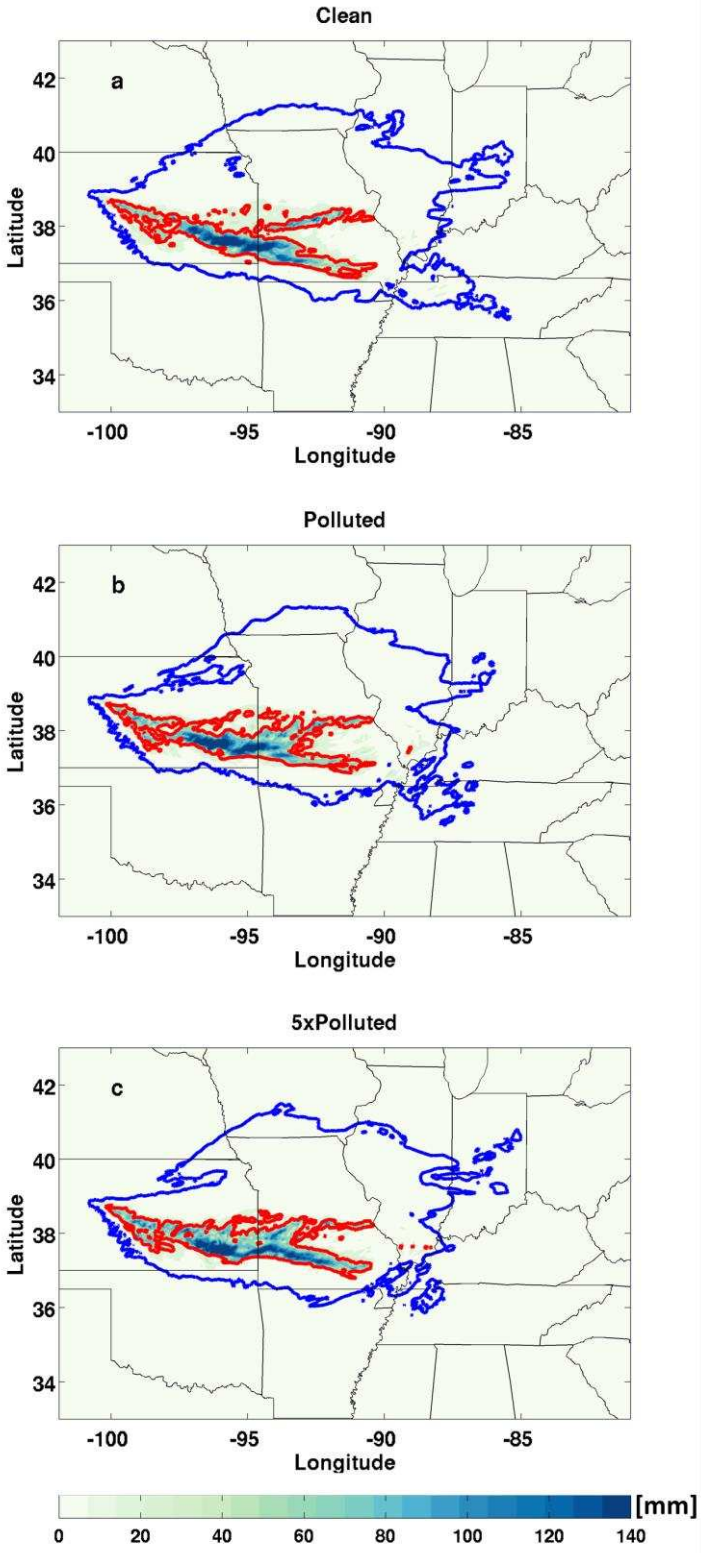

Figure 2.8: Total accumulated precipitation (shaded) [mm], 0.05 mm isopleth (contoured in blue) and the 50 mm isopleth (contoured in red) from the three MCS simulations:(a) Clean, (b) Polluted and (c) 5xPolluted.

The difference in the spatial distribution of accumulated precipitation amongst the simulations due to aerosol impacts is discussed in Section 2.4.3.

2.4.3. Response of simulated MCS precipitation to changes in aerosol concentrations

2.4.3.1 Total Precipitation

By the end of the analysis period (0630-1730 UTC), all three of the simulations produced similar amounts of volumetric precipitation (~$8 \cdot 10^9$ m^3), with differences of less than 1% among the simulations. Although the total volumetric precipitation did not differ substantially, the spatial distribution of accumulated precipitation among the three simulations did change. An increase in aerosol concentration produced heavier precipitation over a larger area while lighter precipitation over a smaller area as seen in the number of grid points containing precipitation totals above thresholds between 0 to 140 mm (99% of the data) in 5mm precipitation intervals (Figure 2.9). Relative to the CLEAN simulation, the 5xPOLLUTED exhibited a smaller number of grid points with lighter accumulated precipitation (0-25mm) and more numerous grid points with heavier accumulated precipitation amounts (30-135mm). These findings indicate that increased aerosol number concentrations led to a shift in precipitation from lighter to heavier precipitation rates. A similar trend is seen between the CLEAN and the POLLUTED simulation, however, the differences were smaller in magnitude. This shift is further indicated in figure 2.8, where the area of total MCS precipitation (contoured in blue in Figure 2.8) was 8% and 9.5% less in the POLLUTED and 5xPOLLUTED simulations relative to the CLEAN simulation, respectively. However, the spatial extent of the area with accumulated total precipitation greater than 50mm (90^{th} percentile, contoured in red in Figure 2.8) was greater in the POLLUTED and 5xPOLLUTED simulations by 9.6% and 21.8%, respectively.

Precipitation efficiency is an indication of how efficient a storm is in converting water vapor into precipitation. The precipitation efficiency of the simulated MCS was calculated using two methods: (1) calculating the ratio between the differences in hydrometeor mass gain and loss to hydrometeor mass gain (Khain et al. 2005), and (2) determining the ratio between the surface rainfall rate to the rate of condensation and deposition (the Cloud Microphysics Precipitation Efficiency (CMPE) (Sui and Li, 2005). Both calculations showed a shift to higher precipitation efficiencies in the more polluted simulations throughout the analysis period (not shown). The differences in precipitation rates, area of precipitation and precipitation efficiency are now explained by analyzing the contributions of the convective and stratiform precipitation to the total precipitation.

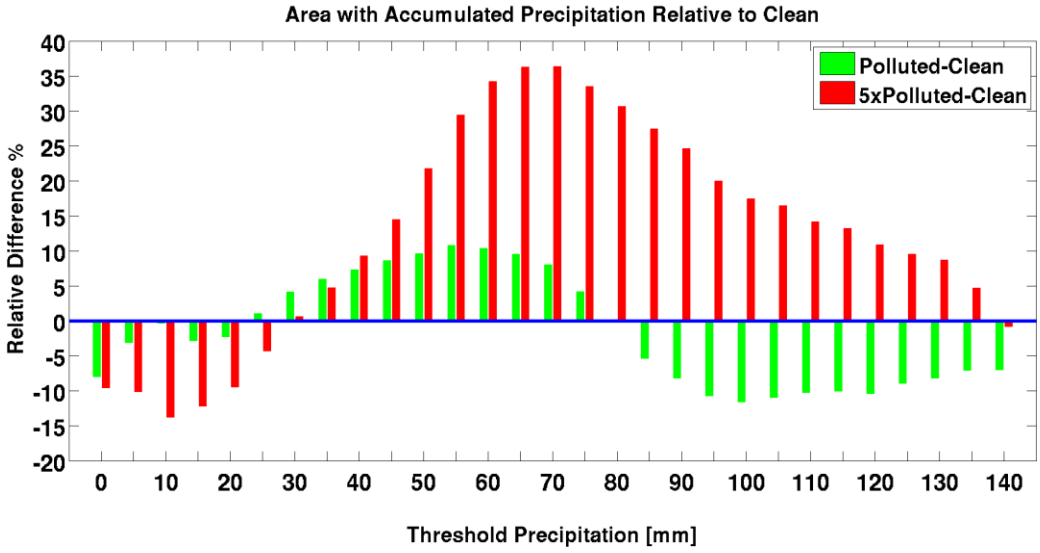

Figure 2.9: Relative difference in the areas containing accumulated precipitation above a given value [mm] in the polluted (green) and the 5xpolluted (red) simulation in comparison to the Clean simulation.

2.4.3.2. Convective and Stratiform Precipitation

MCS precipitation can be characterized into two regions, convective and stratiform, which differ in dynamical properties, microphysical processes and precipitation rates (Leary and Houze, 1979). The division utilized here was based on two parameters: surface precipitation rate [mm hr^{-1}] and the column maximum vertical velocity [ms^{-1}], which was adapted from the criteria set by Churchill and Houze (1984), Tao et al. (1993) and Alexander & Cotton (1998). The MCS partitioning into convective and stratiform-anvil regions was done as follows. A grid column is defined as convective if ANY of the following are true: (1) the precipitation rate is two times the average background precipitation rate with an added criterion that the precipitation rate must be greater than 10 $mmhr^{-1}$ in order to eliminate stratiform precipitation that exhibits the same trend; (2) precipitation rates are greater than 25 $mmhr^{-1}$; (3) all grid columns adjacent to a flagged convective column (according to either (1) or (2)) are also flagged convective; or (4) the maximal vertical velocity exceeds 5 ms^{-1}.

The background average precipitation rate was calculated from an area around the grid column of interest using 6 grid points in each direction, which corresponds to an area of ~370 km^2 and is similar to the background area size defined in Churchill & Houze (1984). A third region referred to as "mixed" for cumulative variables such as accumulative precipitation was defined as a grid column which was defined as convective (stratiform-anvil) at analysis file output time t, but as stratiform-anvil (convective) in the previous output file time, t-1. The relative contributions to the total volumetric precipitation rate [m^3s^{-1}] from the three regions (Figure 2.10) show that the convective region is the dominant contributor to the total volumetric precipitation rate during the first half of the analysis period (0630-1230 UTC). After 1230 UTC, the highest contributor to the precipitation shifts from convective to stratiform-anvil in the

CLEAN and POLLUTED simulations. This shift from convective to stratiform-anvil precipitation as the system matures is in agreement with previous findings of MCC precipitation characteristics (McAnelly and Cotton, 1986). A shift to a larger contribution from the stratiform-anvil region to the total volumetric precipitation also occurs in the 5xPOLLUTED simulation, however 2 hours later than both the CLEAN and POLLUTED simulations, indicating that the 5xPOLLUTED simulation had the highest precipitation yield from convective precipitation throughout the analysis period.

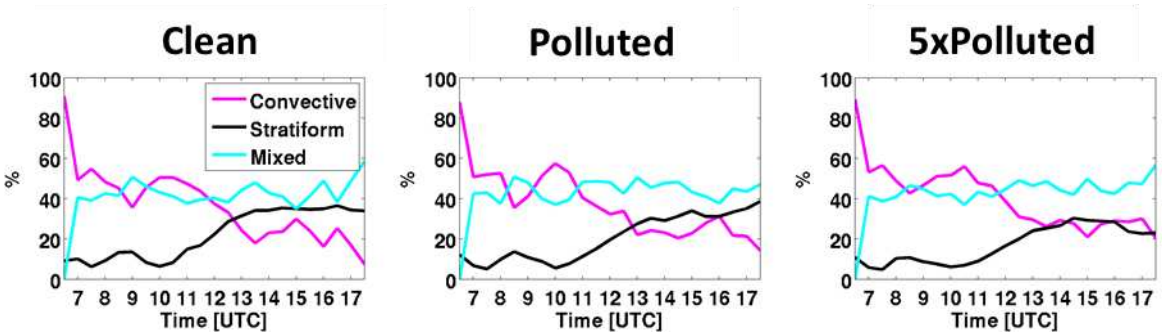

Figure 2.10: Relative contribution of the volumetric precipitation rate [km^3s^{-1}] from the each of the regions: convective (magenta), mixed (cyan) and stratiform-anvil (black) to the total volumetric MCS precipitation in the Clean simulation (left), Polluted simulation (middle) and 5xPolluted simulation (right).

The comparison of the accumulated volumetric precipitation among the regions shows that enhanced aerosol concentrations led to an increase in convective precipitation, a decrease in stratiform precipitation and negligible change in the mixed region throughout the analysis period (Figure 2.11). By the end of the analysis period, the POLLUTED and 5xPOLLUTED simulations produced 2.43% and 15% more convective precipitation, 3.5% and 5% more mixed precipitation and 10% and 25% less stratiform precipitation in comparison to the CLEAN simulation, respectively. Therefore, even though changes in the aerosol concentrations among the three simulations had little effect on the total amount of accumulated volumetric

precipitation, it did change the precipitation contributions from the different regions (Figure 2.11). The differences among the simulations in the mixed region were found to be negligible in comparison to the convective and stratiform regions, and therefore, are not discussed further.

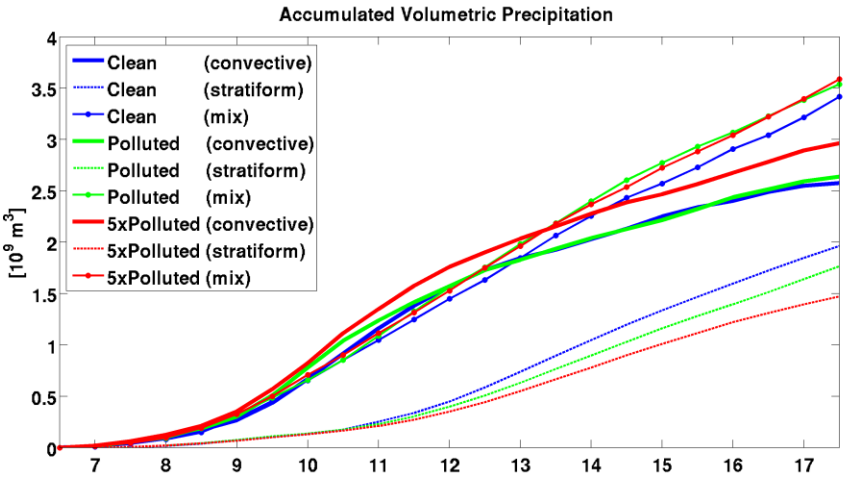

Figure 2.11: Accumulated Volumetric Precipitation from the convective (solid), stratiform (dashed) and mixed region (dotted) for the three simulations: Clean (blue), Polluted (green) and 5xPolluted (red) as a function of time.

The trends in volumetric precipitation are a function of both the precipitation area as well as precipitation rates (Kane et al., 1987). In order to examine the aerosol impacts on the two components of volumetric precipitation, the mean precipitation rates [mm hr^{-1}], and the total precipitation area of each region [km^2] are compared (Figure 2.12). Furthermore, Figure 2.12 also features the area of the non-precipitating points, in order to examine the fraction of the each region which is precipitation. The higher convective volumetric precipitation in 5XPOLLUTED is predominantly attributed to the precipitation rates (Figure 2.12a) and not the areal extent of the convective region (Figure 2.12c). The higher volumetric precipitation in the stratiform-anvil of the CLEAN simulation is attributed to both higher precipitation rates (Figure 2.12b) as well as a larger area of precipitating anvil (Figure 2.12d). It is important to note the non-monotonic trend

between the area and the precipitating area of the stratiform-anvil region (Figure 2.12d) with the increase in aerosol concentrations. While the precipitating region of the stratiform-anvil was the largest in the CLEAN simulation (solid lines, Figure 2.12d), the 5xPOLLUTED simulation produced the largest stratiform-anvil (dashed lines, Figure 2.12d). This emphasizes that the larger area of the precipitating stratiform-anvil in the CLEAN case is due the microphysical processes that contributed to a larger fraction of the stratifrom-anvil that produced precipitation.

In order to understand why enhanced aerosol concentrations in the POLLUTED and 5xPOLLUTED simulations caused an increase in the convective precipitation and decreased the stratiform precipitation formation mechanisms, the precipitation formation mechanisms for the two regions are now examined.

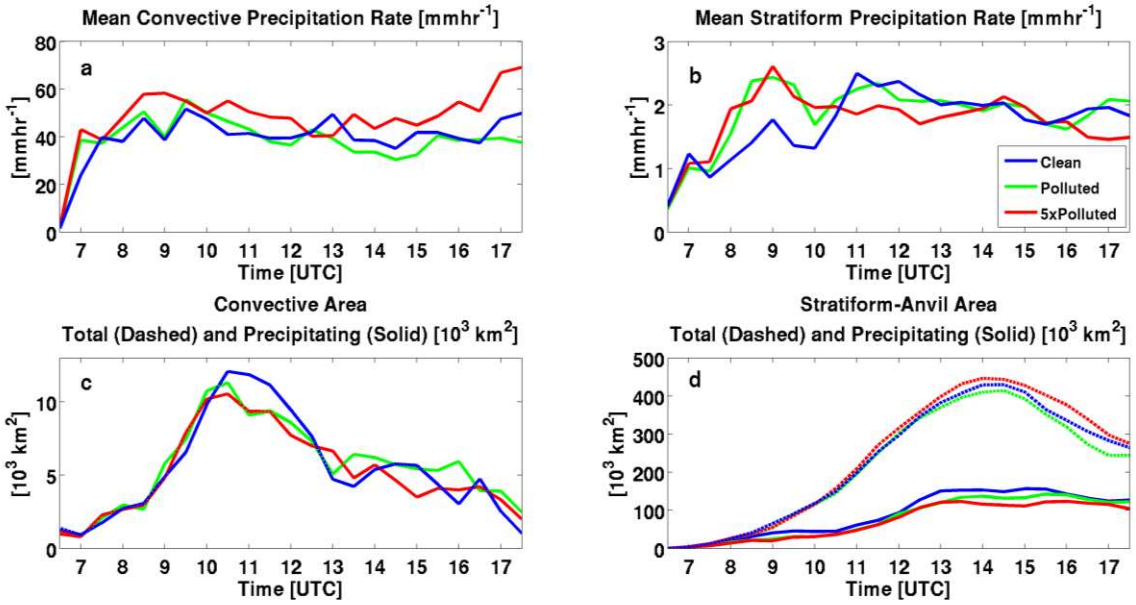

Figure 2.12: For the three simulations Clean (blue), Polluted (green) and 5xPolluted (red) simulations: (a) Mean convective precipitation rate [mm hr^{-1}] as a function of time. (b) Mean stratiform precipitation rate [mm hr^{-1}] as a function of time. (c) Total area of the convective region [km^2] (dashed) and area with convective precipitation (solid). (d) Total area of the stratiform-anvil region [km^2] (dashed) and area with stratiform precipitation (solid). Note, nearly 100% of the convective region was precipitating, therefore, in panel c, the dashed and solid lines overlap.

2.4.3.3 Precipitation Processes: warm versus cold microphysics

The column integrated mean collision coalescence and riming rates [kg s^{-1}] were calculated in the convective and stratiform-anvil region for each simulation as a function of time. Within each simulation, in both the convective and stratiform-anvil regions, the rates of riming and collision coalescence were of similar magnitude indicating that both processes were important in producing precipitation in the two regions of the storm (not shown). The enhanced precipitation from the convective region and the reduction from the stratiform-anvil region are attributed to changes in both the warm rain processes of collision-coalescence as well as cold precipitation formation via riming (Figure 2.13) and are discussed in the following sections.

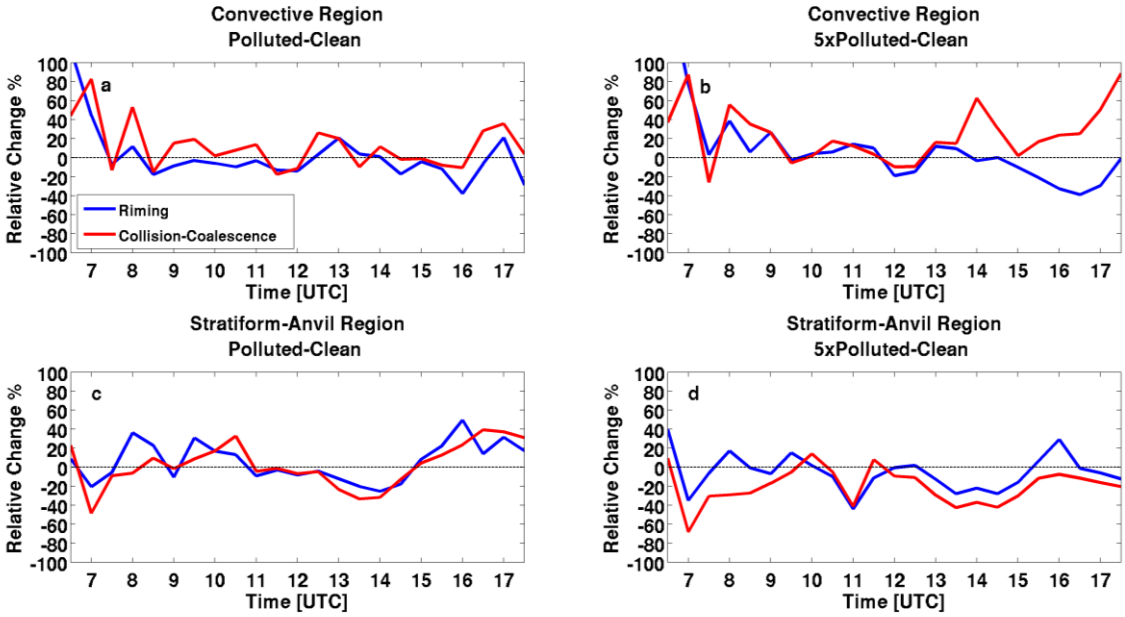

Figure 2.13: Relative differences in the mean column integrated riming and collision coalescence (C-C) rates [kg s^{-1}] in the polluted simulations relative to CLEAN: for the POLLUTED simulation in the (a) convective region and (c) stratiform-anvil region and for the 5xPOLLUTED simulation in the (b) convective region and (d) stratiform-anvil region.

a. Convective Region

The 5xPOLLUTED convective region exhibited both higher collision coalescence and riming rates in comparison to both the POLLUTED and CLEAN simulations (Figure 2.13b). While enhanced riming rates in the convective region of the 5xPOLLUTED simulation was apparent only during the first 5 hours of the storm, enhanced collision coalescence was evident throughout the entire analysis period (Figure 2.13b). In the POLLUTED simulation, throughout the majority of the analysis period, only collision coalesce was enhanced in comparison the CLEAN simulation (Figure 2.13a).

Past studies have shown that for a given liquid water content, higher aerosol concentrations nucleate more numerous yet smaller cloud droplets with smaller collection efficiencies (Twomey, 1974, 1977). In this study, the decrease in collision coalescence efficiency of the smaller cloud droplets within the polluted simulations led to the formation of fewer rain drops (Figure 2.14b). The fewer rain drops exhibited a reduction in the collection competition of cloud droplets onto rain drops which led to the formation larger rain drops (Figure 2.14a). In addition, the higher aerosol concentrations in the polluted simulations nucleated more cloud droplets which, in turn, underwent greater condensation rates (owing to their greater integrated net surface area). The enhanced latent heat release due to the larger condensation rates led to higher updraft velocities (Figure 2.15) which enabled the transport of more liquid cloud mass to higher levels within the convective region. Therefore the enhanced warm rain production within the more polluted simulations may be explained by two processes: first, a greater number of cloud droplets made available to be collected by fewer rain drops, and the second may be attributed to the increased residence time of the collecting rain drops within the cloud. The latter may be explained by the simple Bowen (1951) model: larger aerosol concentrations led to more

cloud droplet nucleation which, in turn, produced stronger vertical velocities due to enhanced latent heat release. The stronger updrafts lofted the liquid cloud mass to higher levels within the cloud which enhanced the collection rates of cloud droplets by rain occurring at higher levels as well as exposed the rain drops to deeper liquid water paths, as seen by the larger rain drop diameters in the 5xPOLLUTED simulation at all vertical levels (Figure 2.15a). Furthermore, the stronger vertical velocities are able to suspend the larger rain drops within the updrafts, thus allowing rain drops to grow to larger diameters before descending to the surface. This, in turn, produced larger rain drops which reduced the potential for evaporation below cloud base (Figure 2.14c) owing to their net reduction in surface area (van den Heever and Cotton, 2004).

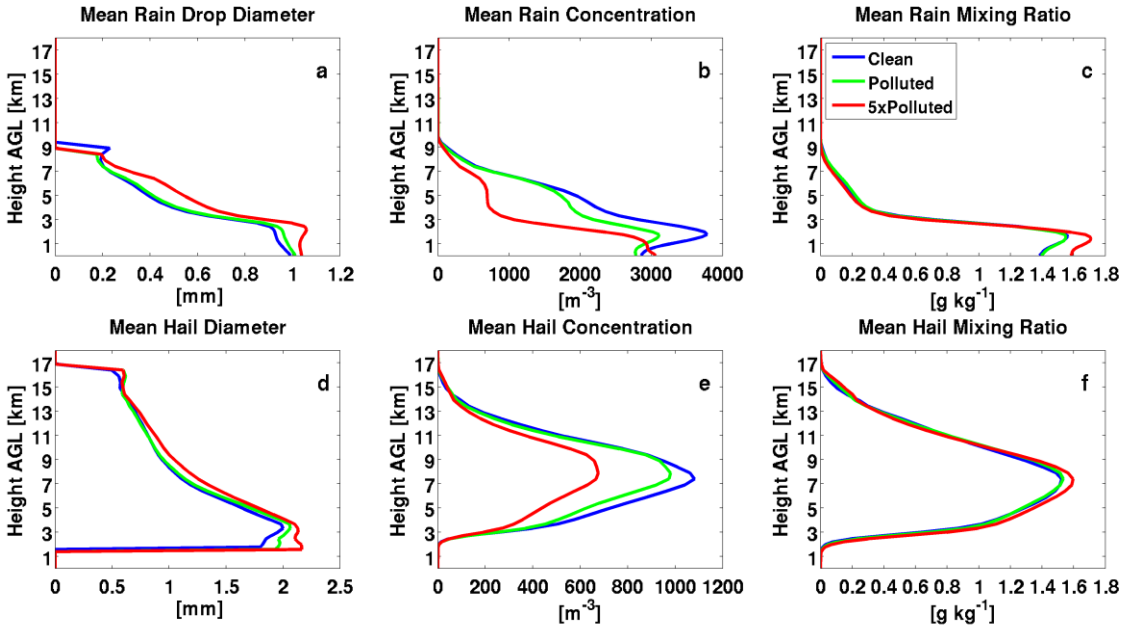

Figure 2.14: Spatial and temporal means in the convective regions, of rain (top row) and hail (bottom row) diameter, concentration and mixing ratio, during 0630-1730 UTC and 0630-1130, respectfully: (a) rain drop diameter [mm], (b) rain concentration [m^{-3}], (c) rain mixing ratio [g kg^{-1}], (d) hail diameter [mm], (e) hail concentration [m^{-3}] and (f) hail mixing ratio [g kg^{-1}].

The time dependent increase in riming rates within the 5xPOLLUTTED in comparison to the CLEAN simulation during the first 5 hours of the storm (Figure 2.13b) corresponds to the time in which the LLJ supplied the region with elevated moisture from the Gulf of Mexico. In the 5xPOLLUTED simulation, the added aerosol concentration in the moist environment enabled nucleation of more numerous cloud droplets, which were able to reach higher altitudes, despite the enhanced collision-coalescence process. In the POLLUTED simulation, due to lesser aerosol concentrations in comparison to the 5xPOLLUTED, enhanced collision-coalescence depleted the cloud mass concentration at higher levels (e.g. Seigel et al. 2013) and therefore, produced smaller riming rates to that of the CLEAN simulation. The greater riming rates in the 5xPOLLUTED simulation are further supported in Figure 2.14d which shows that the 5xPOLLUTED simulation produced larger hailstones and greater hailstone mass throughout the convective column during the first 5 hours of the simulation.

Within the convective region of the polluted simulations, updrafts were stronger throughout the vertical column in comparison to the CLEAN simulation (Figure 2.15). This increase is attributed to enhanced latent heat release of condensation at lower levels and freezing and vapor deposition aloft attributed to higher amounts of cloud mass and the smaller cloud droplet diameters, respectfully (e.g., Khain et al. 2005; van den Heever et al. 2006; van den Heever and Cotton 2007; Lynn et al. 2007; Ntelekos et al. 2009). The stronger updrafts in the 5xPOLLUTED simulation suspended the larger hail stones and increased their residence time within the updraft. Similar to the collection processes within the warm cloud layer, fewer hail stones in the 5xPOLLUTED introduced less competition for the riming cloud droplets, thereby producing larger hail stones. Therefore in the 5xPOLLUTED simulation, the reduced

competition of collection overwhelmed the reduction on the collection efficiency, producing a net increase in riming rates.

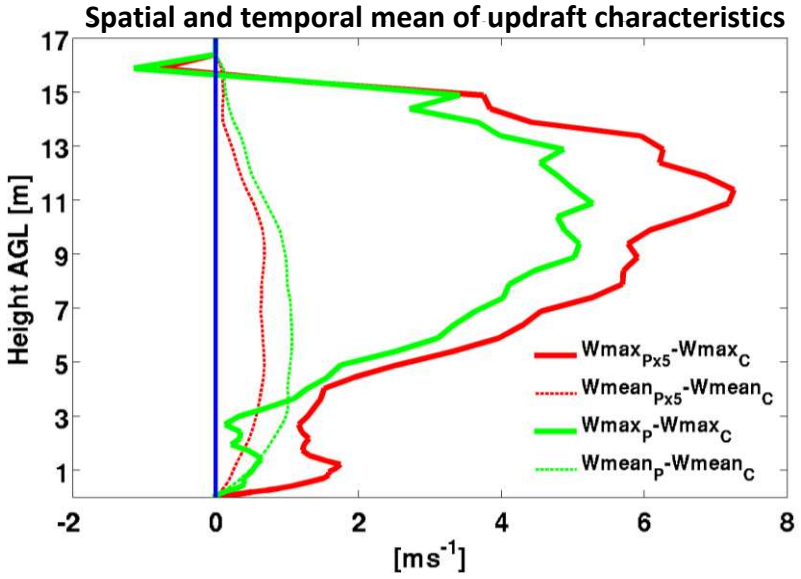

Figure 2.15: Spatial and temporal mean during 0630-1730 UTC of the maximum updraft velocity (solid) and mean updraft velocity (dashed) differences relative to the CLEAN simulation of POLLUTED (green) and 5xPOLLUTED (red).

b. Stratiform-Anvil Region

Increased aerosol concentrations led to a decrease in total volumetric stratiform precipitation (Figure 2.11), primarily due to a smaller fraction of the stratiform-anvil which produced precipitation (Figure 2.12d). During the majority of the analysis period, the 5xPOLLUTED simulation exhibited reduced collision-coalescence and riming rates [kg s^{-1}] in the stratiform-anvil region in comparison to the CLEAN simulation (Figure 2.13d). The POLLUTED simulation alternated from having higher and lower rates of precipitation formation in comparison to the CLEAN simulation (Figure 2.13c) throughout the analysis period, thus, suggesting that the microphysical perturbations induced by changes in aerosol concentration led

to temporal changes in the lifecycle of stratiform elements. This suggests why the 5xPOLLUTED simulations produced 25% less stratiform precipitation by the end of the analysis period, while the POLLUTED simulation only exhibited a deficiency of 10%.

Initially the polluted simulations exhibited higher stratiform precipitation rates (Figure 2.12b), however, the precipitation occurred over a smaller fraction of the stratiform-anvil (Figure 2.12d), thereby reducing the volumetric precipitation from that region (Figure 2.11). In order to understand the hydrometeor components in the stratiform-anvil, vertical profiles were examined in regions subjectively placed around the convective cores at time 1230 UTC (Figure 2.16). This time was chosen since 1230 UTC was the time where the MCS stratiform-anvil was fully developed (Figure 2.12d) and the stratiform-anvil became an important contributor to the MCS precipitation (Figure 2.10). Each region (Figure 2.16) represented a grid volume with an area of 10x10 km^2 with approximately 35 vertical profiles.

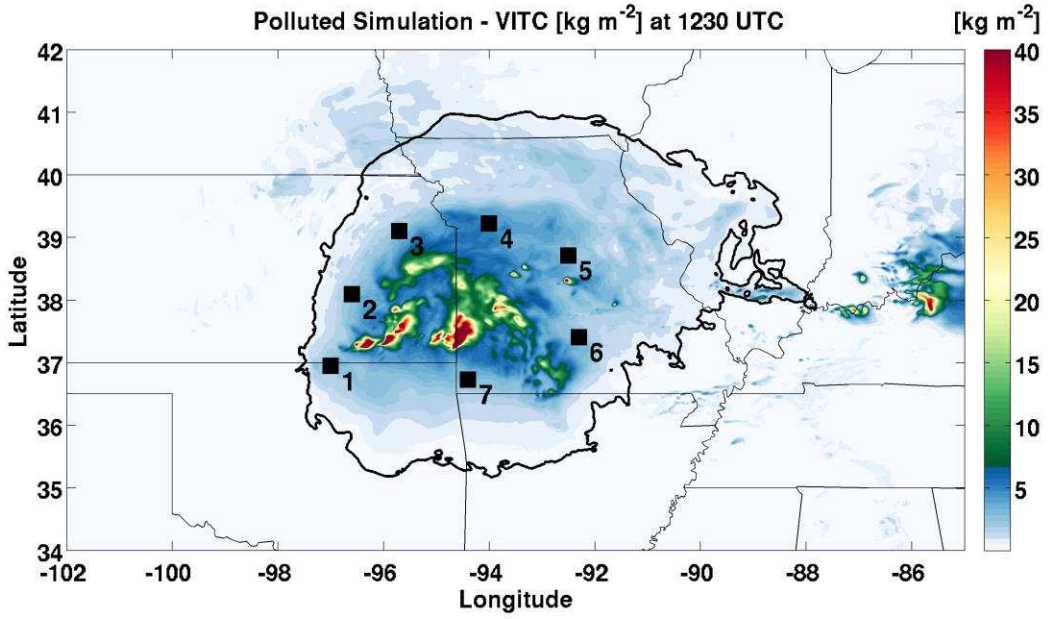

Figure 2.16: Polluted simulation Vertically Integrated Total Condensate (VITC) at 1230 UTC with the locations of the 10x10 km^2 grid volumes within the stratiform-anvil (locations 1-7).

The vertical profiles within the stratiform-anvil region indicate three different cloud structures, depending on the location relative to the convective region. Upstream, the stratiform-anvil clouds were composed primarily of upper-level stratiform clouds (example: Region 2, Figure 2.17a). North of the convective region, thicker stratiform clouds with cloud bases as low as 3 km AGL were evident (example: region 4 Figure 2.17b). Downstream of the convective region, thin stratiform clouds with cloud bases of 3km AGL and cloud top heights below 6 km AGL, below a shallow stratiform-anvil (for example region 6 Figure 2.17c). The hydrometeors within the elevated stratiform cloud consist of only ice-phase hydrometeors (Figure 2.17a and 2.17c), the low-level stratus cloud of only liquid-phase hydrometeors (Figure 2.17c), and the deep stratiform cloud of mixed-phase hydrometeors (Figure 2.17b). Therefore, in order to understand aerosol impacts on precipitation formation in the MCS stratiform-anvil region, all three cloud types are examined here. At this time, the CLEAN, POLLUTED and 5xPOLLUTED simulation exhibited the same trend in cloud structure within the stratiform-anvil (not shown). For brevity, analysis of the POLLUTED simulation for regions 2, 4 and 6 are shown here.

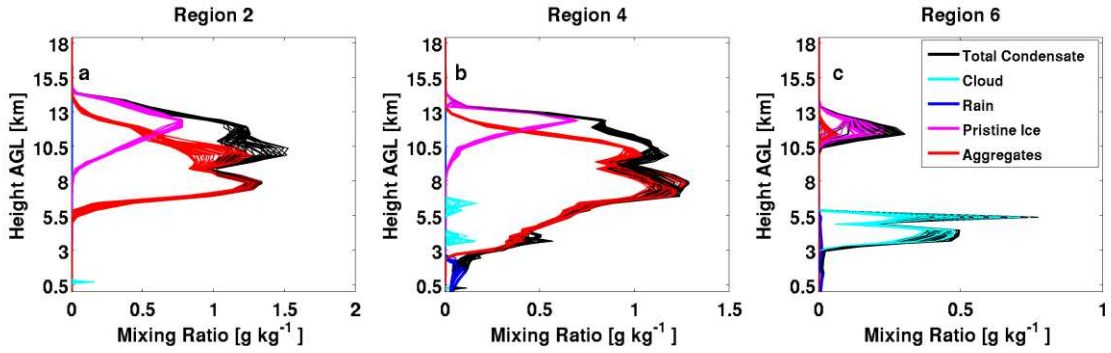

Figure 2.17: Vertical profiles (~35) within three of the regions: region 2(a), region 4(b) and region 6(c) of total hydrometeor mixing ratio (black) as well as the individual mixing ratios of the dominant hydrometeors: cloud (cyan), rain (blue), pristine ice (magenta) and aggregates (red).

Past studies have shown that the hydrometeor source in an MCS anvil is initially only from the outflow of hydrometeors from the deep convective cells. As the storm matures, slowly ascending mesoscale updrafts develop, which form the stratiform-anvil of the MCS (Cotton et al., 1995, 2010; Houze, 2004). These studies have shown that this slow ascent was found to be present in the middle and upper troposphere in a broad region surrounding the convective cores, and it is formed due to the deep convergence layer associated with the diabatic heating profile of an MCS (e.g Cotton et al. 1989). To determine the source of the hydrometers (slow ascent or convective outflow) in each of the regions (Figure 2.16), a Lagrangian model (LM) (Grasso, 1996) was used to compute the backwards parcel trajectories from each of the seven regions presented in Figure 2.16. From the 7 locations, parcels from 28 vertical levels from 3 to 16km AGL within cloudy grid boxes (total condensate $\geq 0.01 g\ kg^{-1}$) were inputted into the LM. RAMS was rerun for the period of 90 minutes from 1100-1230 UTC and the 3D wind components (u,v and w) from the Eulerian RAMS Grid 3 at each time step were saved. These data were then used in the LM in order to perform a tri-linear interpolation in space to the new parcel location. The parcel's movement was solved by the 4^{th} order Runge-Kutta method. The time interval of 90 minutes was chosen in order to be able to examine the presence of the slow ascending mesoscale updrafts which travel over a hundred kilometers horizontally at slow ascent speeds.

Data from all the parcels in each region were used to calculate characteristics along the parcel trajectories and are represented by scatter plots as a function of the height of the parcel AGL at 1230 UTC. Figure 2.18 presents the characteristics of the parcels along its 90 minute trajectory within region 2 (Figure 2.18, top row), region 4 (Figure 2.18, middle row) and region 6 (Figure 2.18, bottom row). These characteristics include the change in the parcel's height (Figure 2.18a, d and g), mean vertical velocity (Figure 2.18b, e and h) and changes in the total

condensate mixing ratio (Figure 2.18c, f and i). The analysis shows that in all the regions hydrometeors at the higher altitudes (above 12 km AGL in regions 2 and 4 and above 10 km AGL in region 6) originate in the outflow of the convective region. This is seen according to the parcel trajectories (not shown), the change in the height of the parcels between 1100-1230 UTC (Figure 2.18a,d,g) , the higher mean vertical velocities (Figure 2.18b,e,h), as well as the loss in hydrometeor mass due to the diverging outflow (Figure 2.18c,f,i).

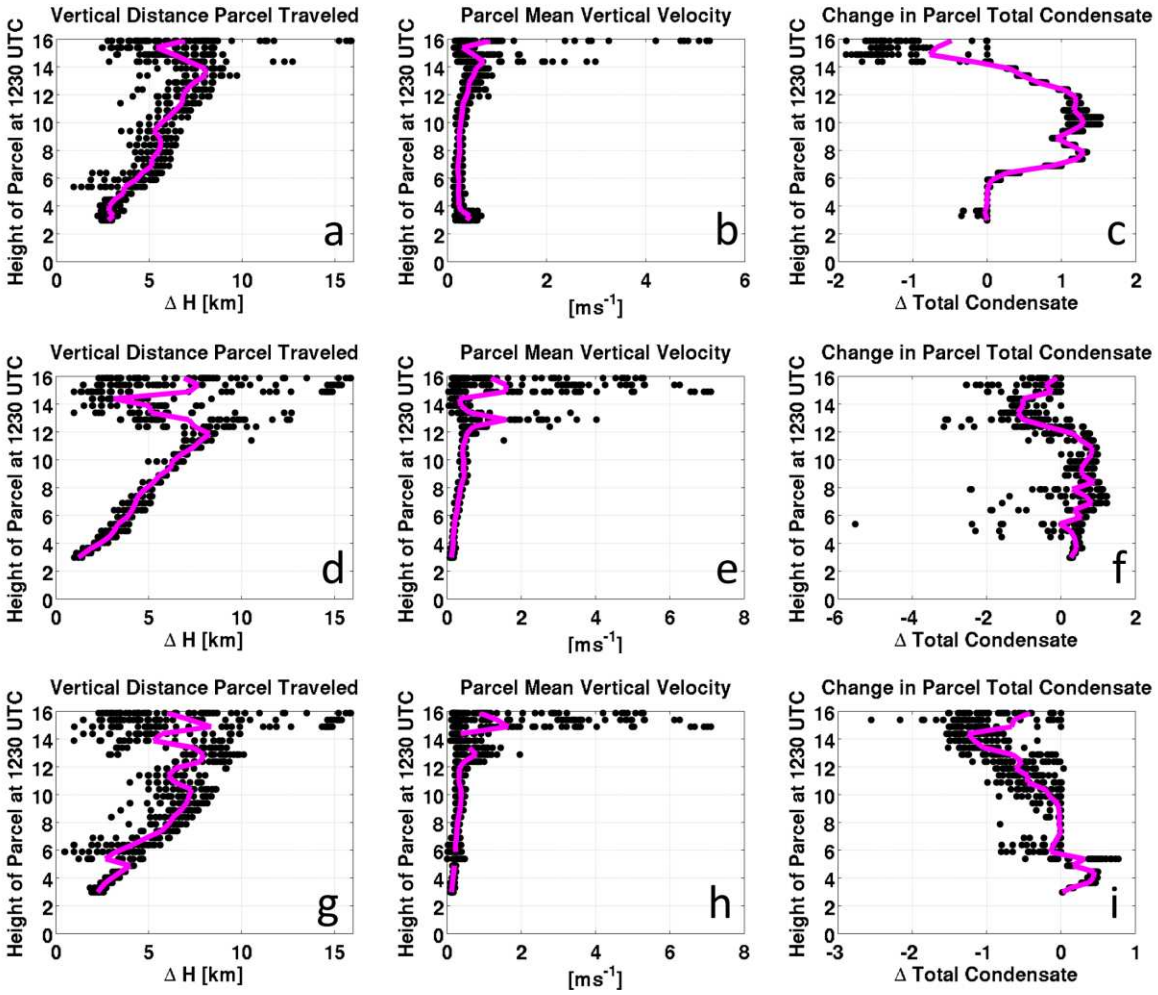

Figure 2.18: Scatter plots (from left to right) of parcel change in height, mean vertical velocity and change in parcel's condensate mass as a function of height of parcel at 1230 (y-axis) for the three regions: region 2(top row), region 4 (middle row) and region 6 (bottom row) for each of the back trajectories. The mean value of each scatter plot is plotted in magenta.

The shallow liquid-phase stratiform cloud in region 6 is due to slow ascent from the south, originating within the boundary layer (now shown). The deeper stratiform cloud represented in region 4 is constructed of two air sources: slantwise slow ascending mesoscale updrafts and diverging outflow from the convective cores. The slow ascending updrafts were found to originate from 1-4 km AGL (Figure 2.18a, d, g). These two air sources are included in the scatter plots, which show that for higher altitudes there is condensate loss with higher vertical velocities, while at lower levels there is condensate gain with lower vertical velocities, consistent with slantwise ascent. Independent of the origin height, the slantwise ascent was similar in all levels, where air slowly ascended with vertical velocities averaged to be below 1 ms^{-1} gaining condensate mass during the ascent.

The trajectory analysis indicates that outflow from the convective cores does not produce precipitation until the stratiform cloud deepens due to the interaction with the slantwise slow ascent. Therefore, interaction between the two air sources determines the potential for precipitation production within the stratiform-anvil region. The 5xPOLLUTED simulation contained higher aerosol concentrations both within the boundary layer and within the free troposphere (Figure 2.5). Therefore, collision coalescence was hampered in both the mesoscale updrafts and in the low level liquid-phase stratiform cloud due to the larger number of aerosol particles nucleating smaller cloud droplets. The slower vertical velocities in the mesoscale ascent produced lower supersaturations, in comparison to that in the deep convective region, thereby introducing more competition in cloud nucleation in the simulations with higher aerosol concentrations, thus producing smaller cloud droplets and hence reduced both collision-coalescence and riming in the simulations with higher aerosol concentrations. Although there was a decrease in warm rain production in the 5xPOLLUTED case, (Figure 2.13d), which lofted

more cloud water mass to higher levels, riming was not enhanced (Figure 2.13d). This was attributed to the formation of more numerous but smaller aggregates, the dominant hydrometeor to rime cloud droplets within the stratiform-anvil region (not shown). In the 5xPOLLUTED simulation, aggregation rates among the ice hydrometeors were reduced while sublimation rates were increased relative to the CLEAN simulation due to the smaller sizes of ice hydrometeors.

Above the boundary layer, the aerosol concentration in the CLEAN and POLLUTED simulations was similar (Figure 2.5), since the additional anthropogenic aerosols, in the POLLUTED simulation, mainly increased the aerosols concentrations near the surface in comparison to CLEAN. Therefore, between the CLEAN and POLLUTED simulation, the air in the mesoscale updrafts sourced above the boundary layer feeding the deep stratiform-anvil contained similar aerosol concentrations. Due to the similarities in aerosol concentration above the boundary layer, the differences between the precipitation in the stratiform-anvil in the CLEAN and POLLUTED simulations are attributed to aerosol concentrations near the surface impacting the convective outflow. This is further supported in the negative correlation in the trends of the riming rate differences between the two simulations within the two regions (Figure 2.13a,c). During times when riming rates were smaller in the convective region in the POLLUTED simulation (Figure 2.13a), the stratiform-anvil region exhibited higher riming rates (Figure 2.13c) and vice versa. This supports the finding that changes in the hydrometeor distributions within the convective outflow are the main reason for changes in riming between the CLEAN and POLLUTED simulations.

2.5. Discussion

In this study, higher aerosol concentration were found to increase the size of the area with heavier accumulated precipitation and decrease the area with lighter accumulated precipitation. This shift was attributed to an increase in convective precipitation and a decrease in stratiform precipitation. Enhanced convective precipitation resulting from an increased number concentration of aerosols has been found in past numerical simulations of deep convection due to enhanced warm rain production (Seigel et al., 2013), formation of larger raindrops with reduced low level evaporation rates (Berg et al., 2008; Li et al., 2009; Storer et al., 2010; Storer and van den Heever, 2013) as well as more efficient cold rain production (Khain et al., 2005; van den Heever and Cotton, 2007). However in this study, in the 5xPOLLUTED simulation, both warm and cold precipitation formation processes were enhanced. For a more moderate increase in aerosols (POLLUTED simulation), enhanced warm rain processes reduced the cloud water available for riming, thus limiting the contributions made by cold precipitation processes, and is similar to the findings of Seigel et al. (2013).

The higher volumetric precipitation was attributed to the precipitation formation within the convective region due to the humid environment of the storm, similar to the findings of Lynn et al. (2005) and Wang (2005), rather than to an increase in the area of convective precipitation. While previous studies of isolated convection have attributed an increase in convective precipitation due to a larger area of convection (Lee et al., 2008; Storer and van den Heever 2013), in this study only the convective precipitation increase was attributed to the microphysical processes and not changes to dimensions of the convective area.

The enhanced convective precipitation in this study may be explained by the unusually moist environment of the 8 May 2009 MCS. This moist environment reduced the evaporation of

cloud droplets aloft as well as the competition for water vapor among nucleating aerosols and growing cloud droplets. The higher liquid water contents enhanced the magnitude of condensate mass that participated in collision-coalescence and riming in the convective region. Therefore, the enhanced amount of cloud water available to be collected overwhelmed the reduction in the collection efficiency associated with the aerosol-induced production of smaller cloud droplets, leading to a net increase in the conversion of cloud droplets to precipitation.

Enhanced stratiform precipitation due to the presence of higher CCN concentrations have been seen in previous studies, however, they are usually accompanied by a decrease in convective precipitation (e.g Tao et al. 2007). In this study, the opposite was found, where the increased aerosol pollution led to a reduction in stratiform precipitation and an increase in convective precipitation (e.g. Seigel and van den Heever, 2013). The difference between these two studies demonstrates the impact of a less humid environment (Tao et al., 2007) versus an extremely moist environment of the 8 May 2009. The impact of aerosols depending on the environmental moisture was also seen in a previous study which examined the impacted of increased aerosol concentrations in a maritime versus continental squall lines (Tao et al., 2007). In this study, the reduction in stratiform precipitation was found to be due to the impact of aerosols on hydrometeors within the two flows composing the stratiform-anvil; convective outflow and slow mesoscale ascent. The latter was determined by performing back-trajectory analysis from locations within the stratiform-anvil. Increased aerosol pollution led to smaller diameters of cloud droplets as well as a decrease in aggregation rates and an increase in sublimation rates at higher levels within both the stratiform-anvil and convective regions. In the moderately polluted simulation, precipitation in the stratiform-anvil was hampered mainly due to the decrease in hydrometeor diameters within the convective outflow due to similar aerosol

concentrations above the boundary layer. In the highly polluted simulation, the decrease in stratiform precipitation was attributed to a reduction in hydrometeor diameters in both flows.

2.6. Conclusions

In this study, the microphysical effect of increased aerosol concentrations on the precipitation produced by a simulated case study MCS, the 8 May 2009 "Super-derecho" MCS, was examined. A set of three RAMS simulations were conducted: CLEAN, POLLUTED and 5xPOLLUTED, in which the initial aerosol distribution, concentration and chemical composition differed based on the output of a 3D chemical model, GEOS-Chem. The CLEAN simulation contained only aerosol concentration from non-anthropogenic sources, the POLLUTED of aerosols from both anthropogenic and non-anthropogenic sources and the 5xPOLLUTED the same distribution as in the POLLUTED simulation, but multiplied by a factor of five.

All three of the simulations produced an MCS that is comparable to that observed in terms of the MCS location, genesis time, propagation, the formation of a bow-echo at the leading line and total precipitation quantities. While the total amount of precipitation did not differ substantially among the simulations, changes in aerosol concentrations altered the precipitation characteristics within the three simulations:

- Greater aerosol concentrations were shown to decrease the total area of the MCS precipitation while increasing the area with heavier accumulated precipitation.
- Greater aerosol concentrations shifted the major precipitation formation regions from the stratiform-anvil regions to the convective regions within the MCS, thereby, increasing the storm precipitation efficiency of this MCS.

- In the convective region, enhanced updrafts in the polluted simulations condensed more cloud water and transported greater amounts of supercooled cloud water to higher levels which enhanced collision-coalescence and riming rates. Therefore, the more polluted simulations yielded populations of fewer but larger raindrops and hailstones which reduced melting and evaporation at lower levels, thereby enhancing the convective precipitation.
- Precipitation within the stratiform-anvil was found to decrease due to the presence of higher aerosol concentration near the surface as well as in the free troposphere, both of which impacted the cloud droplet distribution and in turn precipitation production processes.
- Higher aerosol concentrations within the free troposphere led to more numerous smaller cloud droplets within the region of slow mesoscale ascent, which decreased collision-coalescence as well as riming rates within the anvil, and therefore the accumulated stratiform precipitation amounts.
- These simulations have shown that MCS precipitation formation characteristics are sensitive to the number of aerosols serving as potential CCN, in both the convective and regions of mesoscale ascent.

The findings in this paper are specific to the case study of the 8 May 2009 MCS's environmental characteristics. The enhanced convective precipitation with increased aerosol concentration is attributed primarily to the anomalously humid environment of the 8 May 2009, similar to the findings of other MCS studies within a highly humid environment.

3. The response of a simulated mesoscale convective system to increased aerosol pollution: Part II: Derecho characteristics and intensity.

3.1. Introduction

In the High Plains of the United States, MCSs produce a large portion of warm season precipitation as well as severe weather including flash flooding, hail, tornadoes and strong straight line winds. The meteorological phenomenon of convectively induced straight line winds was discovered by Gustavus Detlef Hinrichs in 1888, who named the phenomena "derecho", a Spanish word which can be interpreted as "straight ahead". Johns and Hirt (1987) reintroduced the term “derecho” to describe convectively induced severe wind as "any family of downburst clusters produced by an extratropical mesoscale convective weather system". Based on operational forecasting experience and the definition of a family of downburst clusters (Fujita and Wakimoto, 1981; Johns, 1982), Johns and Hirt (1987) set the criteria for a severe wind event to be classified as a derecho based on the following spatial, temporal, and wind speed constraints:

- Concentrated area of reports consisting of convectively induced wind damage and/or convective gusts $\geq$26 ms^{-1} (50 knots). This area must have a major axis length of at least 400 km. In this paper derecho-strength (DS) winds will hereafter be referred to as DS winds.
- The severe wind events must be caused by the same MCS and show a pattern of chronological progression.
- Within the derecho area there must be at least three severe wind reports separated by 64 km or more of either 18 -33 ms^{-1} and/or convective gusts of 33 ms^{-1} (65 knots) or greater.

The criterion of "a pattern of chronological progression" refers to the two types of derechos: progressive and serial. These two types are distinguished by the organization of the parent MCS storm producing the severe wind as seen from radar echos (Johns and Hirt, 1987). The radar signature associated with downbursts and microbursts was identified and named "bow-echo" by Fujita (1978) due to the bowed characteristic of the radar reflectivity. A bow-echo pattern evolves as a convective downdraft reaches the surface and creates an enhanced outflow, which subsequently propagates the convective cells forward. For this reason, the apex of the bow signifies the location of the greatest wind speeds near the surface (Fujita, 1978).

Dynamical contributors to enhanced surface outflow include both enhanced downdrafts due to negative buoyancy created by the evaporation of precipitation, and the transfer of high momentum air to the boundary layer (Newton 1950) by the rear inflow jet (RIJ) (Smull and Houze, 1987). The formation of the RIJ occurs as a part of the mesoscale circulation within an MCS which consists of an ascending branch of front-to-rear flow from the leading convective line to the stratiform region and a descending rear-to-front flow within and below the stratiform-anvil (Houze et al., 1989). The rear-to-front flow develops and is accelerated due horizontal vorticity generated by a horizontal buoyancy gradient between the storm-generated cold pool and the buoyant convective updraft (Lafore and Moncrieff, 1989; Weisman, 1992). Factors contributing to the rear-to-front flow include blocking by the upshear anvil outflow, particularly by upshear propagating internal gravity waves (Schmidt and Cotton, 1990) and intensification of descent by evaporation and melting of stratiform precipitation (Cotton et al 2010). Prior to reaching the surface, the flow is further accelerated horizontally towards low pressure associated with the convective updraft (Lafore and Moncrieff, 1989). Long-lived damaging surface winds were also found to be associated with supercell-like convective cells within an MCS. These cells

aid in the intensification of the RIJ (Schmidt and Cotton, 1989) and produce strong downdrafts that form due to the transport of negatively buoyant boundary layer air within an "up-down" downdraft (Knupp, 1987; Bernardet and Cotton, 1998). Furthermore, meso-γ-scale mesovortices (2-20km, Orlanski 1975) which form at the gust front were found to produce DS surface winds (Wakimoto et al., 2006; Atkins and St. Laurent, 2009a). Therefore, one or more of the above dynamical processes may contribute to the formation and sustenance of a derecho event. Recently, Corfidi et al. 2015 proposed a revision to the definition of a derecho event to one that focuses on the dynamics that include the role of both mesovortices and the rear inflow jet in association with a bow-echo radar signature.

The sensitivity of a derecho event to changes in aerosol concentrations will depend on the potential impacts that aerosols may have on the parent MCS, particularly the formation of strong convective downdrafts throughout the lifetime of the storm. Past numerical and observational studies have found that increased aerosol concentrations may lead to the invigoration of deep convective storms due to the indirect effect of aerosols serving as Cloud Condensation Nuceli (CCN) (e.g Andreae et al., 2004; Khain et al., 2005; van den Heever and Cotton, 2007; Lee et al., 2008; Rosenfeld et al., 2008; Storer and van den Heever, 2013; Fan et al., 2013). These studies have shown that for increased amounts of CCN, smaller cloud droplets form leading to a reduction in the collision coalescence efficiency. This, in turn, reduces the warm rain production, increases the amount of liquid water within the cloud which is subsequently lofted to form ice hydrometers, thereby releasing additional latent heat and intensifying the updrafts. MCS precipitation and dynamics sensitivity to aerosol loading is the subject of ongoing observational and numerical research (e.g Khain et al. 2005; Tao et al. 2007; Li et al. 2009; Seigel et al. 2013; Lebo and Morrison 2014). Past studies have found that the RIJ intensity is sensitive to ice

microphysics (Yang and Houze, 1995) and that the structure of a simulated bow-echo can strongly depend on the manner in which microphysical processes are parameterized within CRMs due to the impacts of such schemes on the cold pool intensity (Adams-Selin et al., 2013). Seigel et al. (2013) found that changes in hail size may introduce a positive feedback on RIJ intensity within a squall line via the recirculation of hydrometeors between the convective and stratiform regions. Smaller hail stones were found to be more effectively transported from the convective region to the stratiform region and as the hail hydrometeors descended below the freezing level up shear of the convective core, they encountered the RIJ that transported them back towards the midlevel convective updraft. This, in turn, promoted additional latent heat release of condensation and deposition within the convective updraft which enhanced the buoyancy thereby, increasing the horizontal buoyancy gradient between the storm-generated cold pool and convective updraft and further invigorated the velocity of the RIJ. These findings further emphasize the importance of changes microphysics on the dynamical feedback within an MCS.

Aerosol concentrations have been found to change the hydrometeor size distribution and characteristics, specifically the diameter of hydrometeors, which alters the potential for the melting and/or evaporation of hydrometeors (van den Heever and Cotton, 2004; Bryan and Morrison, 2012; Adams-Selin et al., 2013). This, in turn, can modify the intensity of cold pools (van den Heever and Cotton, 2004; Tao et al., 2007; Li et al., 2009). The balance between the horizontal vorticity generated within a cold pool to that of the low-level (0-3km) environmental wind shear is known as RKW-theory (Rotunno et al., 1988). Changes in this balance were found to impact the intensity of the RIJ by altering the tilt of convective cores (Weisman, 1992, 1993) and may also impact the formation of mesovortices along the outflow boundary by modifying the

amount of horizontal vorticity tilted into the vertical (Weisman & Trapp 2003). The balance between the horizontal vorticity of the cold pool to the horizontal vorticity arising due to environmental shear affects the intensity of storms via the upward mass flux of hydrometeors and the self-propagation mechanism of secondary convective formation along the gust front (Rotunno et al., 1988).

Previous studies have found that changes in aerosol concentrations impact the longevity and precipitation of MCSs but that this depends on the characteristics of the environment such as humidity (Khain et al., 2005; Tao et al., 2007) and vertical wind shear (Fan et al 2013; Lebo and Morrison, 2014). Thus, changes in aerosol concentrations might be expected to impact the generation and maintenance of a derecho by impacting the intensity of the characteristics of the parent MCS through changes within the cold pool and convective downdrafts.

In this study the impact of enhanced anthropogenic aerosols on the case study of 8 May 2009 "Super derecho" MCS is investigated. The derecho event of the 8 May 2009 storm was analyzed in several past studies (Przybylinksi et al., 2010; Coniglio et al., 2011, 2012; Keene and Schumacher, 2013; Weisman et al., 2013; Evans et al., 2014; Xu et al., 2015a, 2015b). However, these studies did not examine the potential sensitivity of the storm to changes in aerosol concentrations. This study adds to the current body of work on the 8 May 2009 storm by examining the impacts of increased anthropogenic aerosol concentrations on the storm's characteristics. In Part I, higher aerosol number concentrations serving as Cloud Condensation Nuclei (CCN) led to convective invigoration, enhanced convective precipitation, and a decrease in stratiform precipitation. In this chapter, the sensitivity of the simulated derecho to enhanced aerosol number concentrations is examined. The chapter is organized as follows: the case study is presented in section 3.2 and the model set up and aerosol sensitivity tests are given in Section

3.3. The results of changing aerosol concentration on the derecho produced by the case study storm are presented in Section 3.4. A discussion and conclusion are given in section 3.5 and 3.6, respectively.

3.2 The 8th May 2009 MCS

The 8 May 2009 event has been characterized in previous studies (Coniglio et al., 2011; Weisman et al., 2013) as a leading-line, trailing stratiform (Houze et al., 1989; Parker and Johnson, 2000) bow-echo (Fujita, 1978) MCS which developed a warm-core meso-β-scale (20-200km) vortex in its later stage (Weisman et al., 2013; Evans et al., 2014), as well as numerous meso-γ-scale (2-20km, Orlanski 1975) vortices (Xu et al., 2015a, 2015b). The MCS developed in western Kansas at ~0600 UTC and moved south-southeastwards to the southern Appalachians, traveling over a thousand miles in under 24 hours (Coniglio et al., 2011; Storm Prediction Center (SPC)). The 8 May 2009 MCS developed in an environment characterized by a strong Low Level Jet (LLJ) and high precipitable water (PW) content along a west-east oriented surface boundary. A more detailed description of the MCS environment, evolution, structure and propagation is found in Part I. SPC reports of strong surface winds were documented along the entire storm track of the MCS, from western Kansas to the region of the storm's dissipation, west of the Appalachians (Figure 3.1).

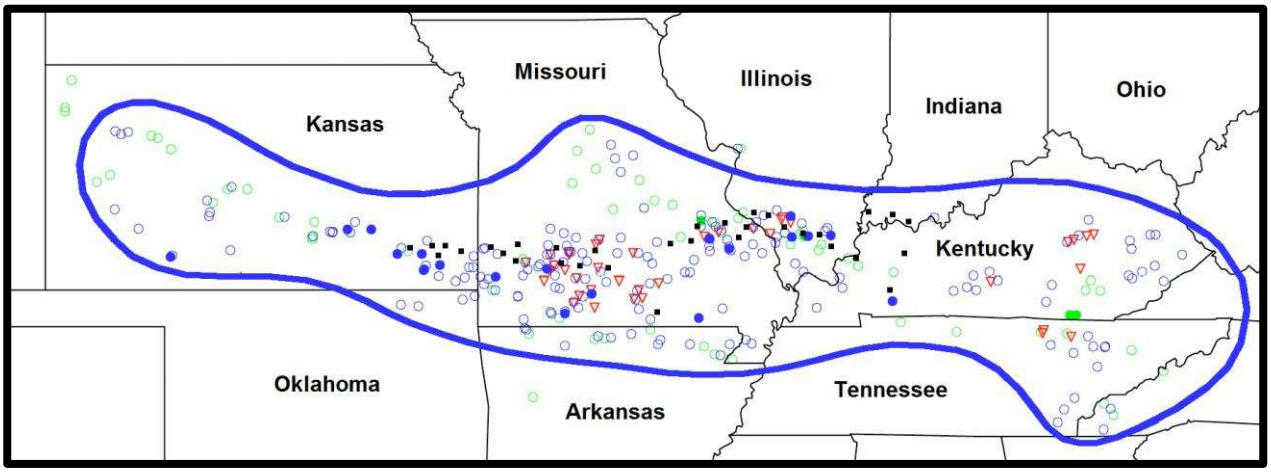

Figure 3.1: The area affected by the May 8, 2009 "Super Derecho" convective system and the severe weather reports associated with it (www.spc.noaa.gov). Area affected is outlined in blue. Severe reports are for the period from 0300-2300 UTC May 8,2009. Wind damage or wind gusts ≥ 50 kts (58 mph) (open blue circles); estimated or measured wind gusts ≥ 65 kts (74 mph)(filled blue circles); hail ≥ 0.75 inches (open green circles); hail ≥ 2.0 inches (filled green circles); and tornadoes (red triangles) are all shown. Flash flooding (by county) is denoted by black squares. Area of most intense wind damage is approximated by band of filled blue circles extending from southeast Kansas through southern Missouri into southern Illinois.

Coniglio et al. (2011) accredited the formation of the strong surface winds during the initial stages of the storm, to intense upward mass flux resulting from a strong and deep LLJ, steep large lapse rates and anomalously high PW. They found that the high PW of the storm's environment reduced the evaporation potential of the hydrometeors, emphasizing the importance of the melting of frozen hydrometers and water loading in the generation of the strong downdrafts in the 8 May 2009 storm. As the storm moved from Kansas into Missouri, a large scale bow-echo developed and several cyclonic mesovortices formed near the apex of the bow-echo on the low-level convergence zone (Pryzybylinksi et al., 2010). Analysis of reflectivity and Doppler velocity over southwest Missouri showed that the three mesovortices occurred simultaneously at ~1330 UTC and that the strongest mesovortex formed in the region where the

cold pool and low level shear were balanced, resulting in vertically erect towers (Przybylinksi et al., 2010). The evolution of the meso-γ-scale vortices within the 8 May 2009 MCS was examined numerically by Xu et al. (2015a; 2015b).

As the storm matured, the north end of the bow echo occluded forming a warm core meso-β vortex (Weisman et al. 2013; Evan et al. 2014) apparent in radar imagery as a comma shape echo (see Figure 2.1f). At the time of the evolution of the meso-β vortex (~1700 UTC) the storm generated cold pool weakened, which allowed the meso-β vortex to deepen to the surface due to the decrease in the near surface pressure, thereby producing strong surface winds (Weisman et al. 2013; Evan et al. 2014). The evolution of the meso-β vortex in the 8 May 2009 in described in detail in Evan et al. (2014).

In summary, the 8 May 2009 MCS, DS winds were found to be generated due to enhanced convective downdrafts (Coniglio et al., 2011), in association with the storm generated cold pool (Weisman et al., 2013) and a descending RIJ (Xu et al. 2015a). Furthermore, strong surface winds were found to be enhanced due to the formation of meso-γ vortices along the gust front and in association with a warm core meso-β vortex during the later stages of the 8 May 2009 MCS, (Weisman et al., 2013). These past studies show that there are several dynamical avenues in which changes in aerosol concentrations may impact the formation of strong surface winds and these form the focus of this study.

3.3 Numerical Model and Experiment Setup

3.3.1 Model Configuration

The 8 May 2009 case study was simulated using the Colorado State University Regional Atmospheric Modeling System (RAMS) version 6 (Cotton et al., 2003; Saleeby and van den Heever, 2013). The RAMS model simulation was set up as a heterogeneous, cloud resolving mesoscale model with three interactive model grids (see Figure 2.4, Part 1). Grids 1 and 2 were set up with a horizontal grid spacing of 40 and 8 km, respectively. The finest nested grid covers the entire domain of the simulated MCS from genesis to decay and was set up with a horizontal grid spacing of 1.6 km. Detailed information on the RAMS model setup is described in section 2.3.1 of Part I.

3.3.2 RAMS simulations

In order to examine the impact of increased aerosol concentrations on the derecho characteristics of this simulated MCS, a set of three numerical simulations were performed: CLEAN, POLLUTED and 5xPOLLUTED. The three simulations utilized the same RAMS model set up as described in Section 3.3.1, however they differed in the initial aerosol concentrations and spatial distribution. Aerosol concentrations were derived from the output of a 3D global chemistry model, GEOS-Chem (Bey et al., 2001). GEOS-Chem model details are given in section 2.3.2 of Part 1, while the model output used in this study and the method of the implementation of aerosols within the RAMS nucleation schemes are given in section 2.3.4. Figure 2.5 (Part 1) presents the vertical profiles of the average total aerosol concentrations [cm^{-3}] at the time of genesis of the MCS (0630 UTC) in the three simulations: CLEAN, POLLUED, and 5xPOLLUTED. The "CLEAN" and "POLLUTED" RAMS simulations were initialized with aerosols derived from only natural emissions (no anthropogenic sources) and both natural and

anthropogenic emissions, respectively. The "5xPOLLUTED" was initialized with the same aerosol distribution as the POLLUTED simulation, however multiplied by a factor of five, in order to examine the impacts of a highly polluted scenario.

3.3.3 Back Trajectory Analysis

In order to understand the impact of changes in aerosol concentrations on the derecho characteristics, the dynamical processes that produced the strong surface winds were first determined. The dynamical processes in this study were analyzed by performing back-trajectory (BT) analysis from grid points with DS winds for the three aerosol simulations. A Lagrangian model (LM) (Grasso 1996) was used to compute the backwards parcel trajectories from grid points with DS winds in each of the three simulations. The BTs were run for duration of 60 minutes, in each of the three simulations, during 2 separate periods of the storm: early evolution and onset decay of the storm. The DS wind grid points were determined according to surface winds at the second vertical model level above the ground (~75m AGL). Wind speed magnitudes of at least 26 ms^{-1} were considered to be potentially part of the simulated derecho event, following the minimum wind speed criteria set by Johns and Hirt (1987). RAMS was rerun for 60 minutes during the two periods of the storm, during which the 3D wind components (u, v and w) from the Eulerian RAMS Grid 3 were written out at each time step (3.33 seconds), as well as virtual potential temperature and total condensate mixing ratio. These data were then used in the LM in order to perform a tri-linear interpolation in space to the parcel's location. The parcel's movement was calculated solving the 4^{th} order Runge-Kutta method. The time step of the LM was also 3.33 seconds, corresponding to the output time of RAMS velocity data, and therefore interpolation in time was not needed. The trajectories were analyzed along with various instantaneous fields outputted from RAMS every 30 minutes (output time interval of Grid 3 data

for all three simulations) around the parcel's location including budget tracking of microphysical processes and cold pool characteristics. The number of BT performed depended on the number of grid points with DS winds within each simulation and varied from 50-300 trajectories.

3.4 Simulation Results

In all three RAMS simulations, convective elements not directly associated with the MCS also developed in Grid 3. In order to isolate the strong surface winds produced by the simulated 8 May 2009 case study, data from the other convective elements were numerically filtered out. The filtering technique, described in detail in Section 2.4.1 of Part I, incorporated parameters such as estimated cloud top temperature [C], precipitation rate [$mmhr^{-1}$] and vertically-integrated total condensate (VITC) [kgm^{-2}]. In this study, data analyzed from the RAMS simulated MCS were taken from MCS genesis at 0630 UTC until 1730 UTC, after which the method for isolating the MCS broke down due to the fragmented stratiform-anvil shield and close proximity of neighboring convection.

In order to assess the simulated derecho event, a map of surface wind magnitudes during the entire analysis period is presented in Figure 3.2, for each of the three RAMS aerosol sensitivity simulations: CLEAN (Figure 3.2a), POLLUTED (Figure 3.2b) and 5xPOLLUTED (Figure 3.2c). Each figure contains the maximum wind speed at each RAMS output time (30 minutes) during the analysis period (0630-1730 UTC), superimposed on the same figure to represent a map of the simulated derecho event as a function of space and time.

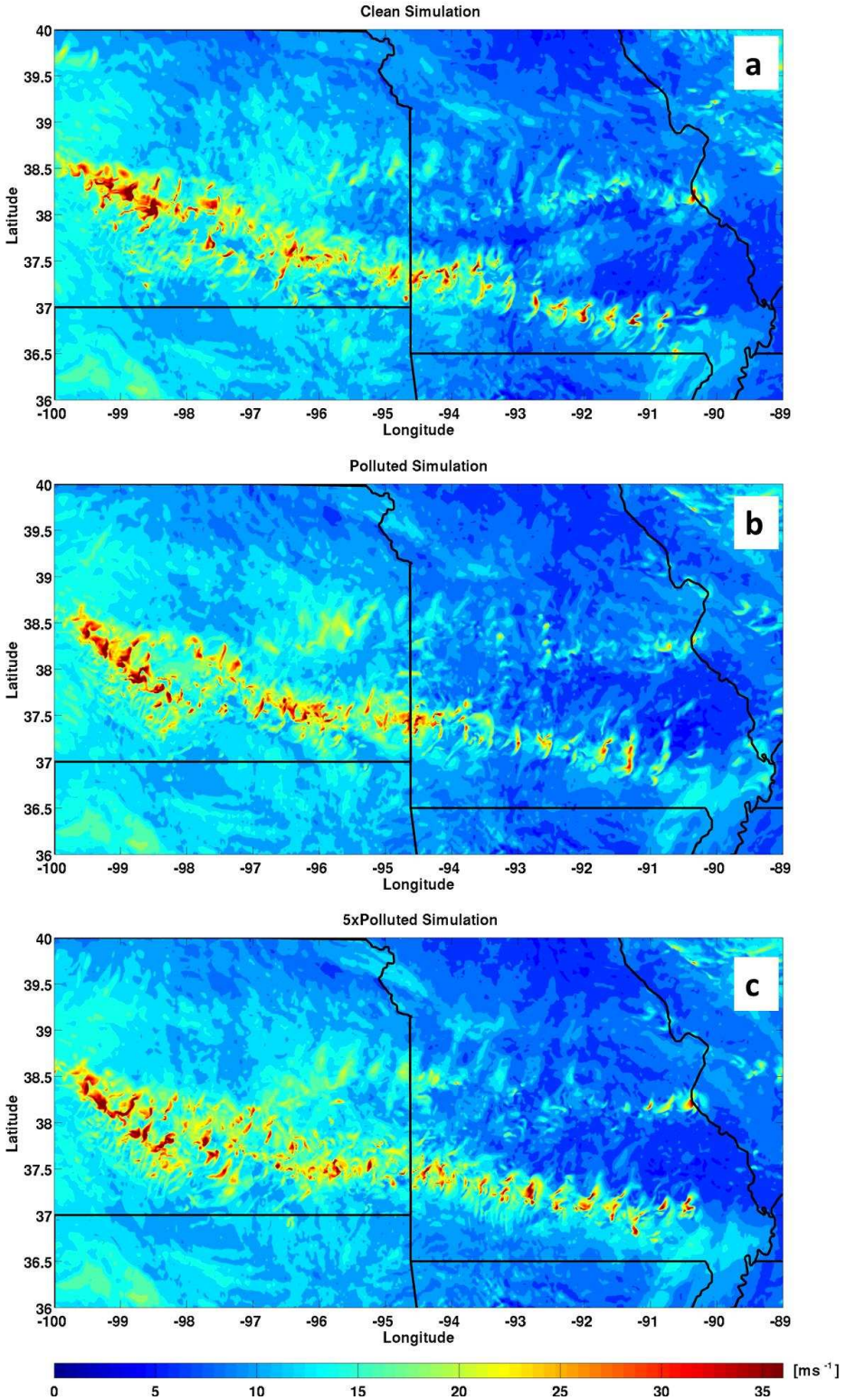

Figure 3.2: Maximum surface wind speed [ms^{-1}] of the simulated MCS every 30 minutes during the analysis period (0630-1730 UTC) for the three simulations: (a) Clean, (b) Polluted and (c) 5xPolluted.

All three of the simulations produced swaths of derecho strength surface winds along a corridor from west Kansas progressing south southeastwards through southeast Kansas and the southern portion of Missouri. After the storm entered Missouri, two paths of derecho strength winds are visible within the southern portion of Missouri and central Missouri. The southern branch covers a larger area with stronger winds in all three of the simulations. These cumulative maps compared favorably with the locations of the SPC reports of strong wind gusts (Figure 3.1) including the location of the two separate branches of DS winds.

We now investigate if changes in aerosol concentrations altered the derecho event by examining its occurrence and strength (defined here as both intensity of the surface wind speeds and area with DS wind) as a function of time during the analysis period. A quantitative comparison of the mean DS wind speed and the number of grid points with DS wind speeds in each of the three simulations are presented in Figure 3.3. The analysis of the number of grid points with DS winds (Figure 3.3a) shows that earlier in the MCS life the area with DS wind was the largest and decreased with time. This suggests that as the storm weakened, different dynamical mechanisms may be responsible for the generation of the strong surface winds. Unlike the changes in the number of derecho grid points (Figure 3.3a), the mean derecho wind speed for both the CLEAN and 5xPOLLUTED simulations are similar throughout the analysis period (Figure 3.3b). Only the POLLUTED simulation shows a decrease in mean derecho-strength wind speeds as a function of time.

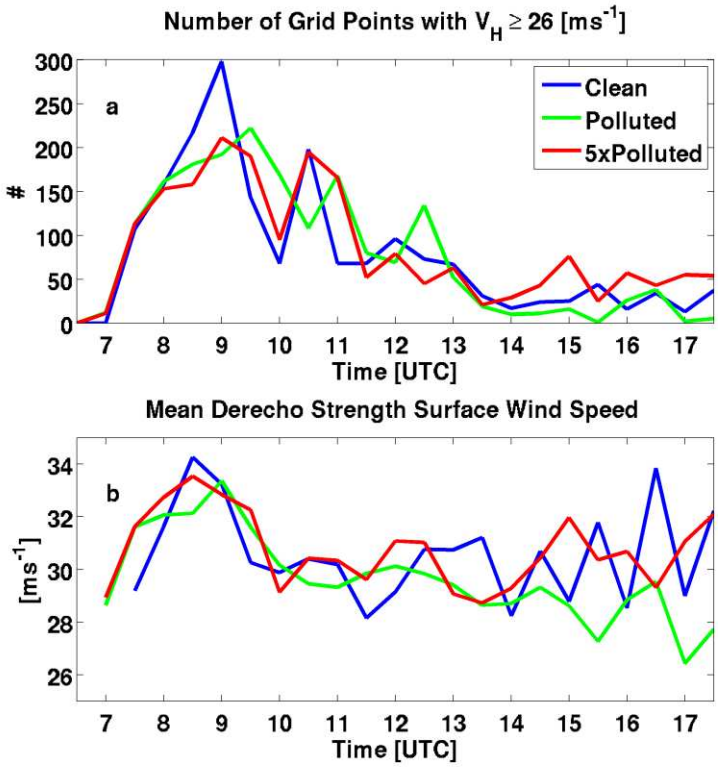

Figure 3.3: Simulated (a) number of grid points with DS wind and (b) mean DS wind speed (b) as a function of time for the Clean (blue), Polluted (green) and 5xPolluted (red) simulations.

The intensity of the DS winds was further investigated by calculating the distribution of the DS wind magnitudes during different periods of the storm: intensification, mature and decay which corresponding to the changes in number of grid points with DS winds (Figure 3.3a). The number of grid points within three ranges of DS winds were examined: weak (26-30ms^{-1}), moderate (30-34 ms^{-1}) and strong (>34 ms^{-1}) normalized by the total number of grid points with DS winds within each simulation for the three periods (Figure 3.4), determined according to changes in the number of grid points with DS winds (Figure 3.2). From Figure 3.4, different trends within the intensity of the DS winds are evident for the different periods. For the first

period (Figure 3.4a), a monotonic trend is apparent where increasing aerosol concentrations led to stronger surface DS winds during the first hours of the storm .

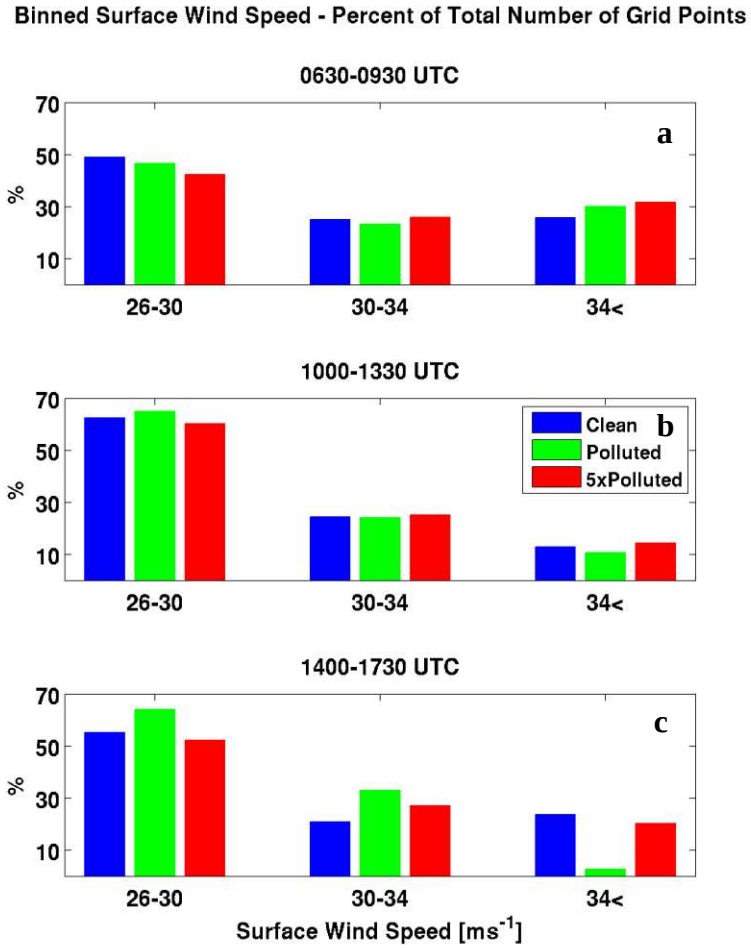

Figure 3.4: Number of grid points with DS wind strength binned and normalized relative to the total number of DS wind grid points with within each simulation: Clean (blue), Polluted (green) and 5xPolluted (red) during the three periods: (a) 0630-0930, (b)1000-1330 and (c) 1400-1730 UTC.

This trend is opposite to that of the area with the DS winds which decreased with increased aerosol concentrations (Figure 3.3a). For the second period the intensity of the DS winds slightly decreases for the POLLUTED simulation, however, this decrease is even more prevalent within the third period (Figure 3.4c).

In order to understand why these trends occurred, the BT analysis was conducted for 60 minutes within the first and third periods for the three simulations, corresponding to the development and onset decay of the MCS. Findings of the derecho characteristics and results from BT analysis are presented for these two periods in the following sections. The BT of parcels which originated from grid points with DS winds are analyzed and compared among the simulations along with RAMS fields which include the density potential temperature (Emanuel, 1994). This metric was chosen since, the relative difference between the cold pool density potential temperature and that of the environment is a measure of cold pool buoyancy (Tompkins 2001; Seigel et al. 2013) and indicates the location of the gust front of the storm.

3.3.1. Simulated Derecho at 0900 UTC

The locations of the region which contained DS winds and for which the BT analysis has been conducted are contoured and superimposed on a map of an estimated 1km AGL radar reflectivity (Figure 3.5). At 0900 UTC, all three of the simulations produced convection along the east-west surface frontal boundary (not shown) organized within a shared stratiform-anvil cloud. The dominant region with DS winds (boxed area in Figure 3.5) occurred for all three simulations within the upstream region of the convective line in association with a Cell Bow Echo (Klimowski et al., 2004), embedded within the bowed convective line. Cell Bow Echoes are described as strong thunderstorms on the scale of 10-25 km which have bowed out due to strong outflow (Klimowski et al., 2004).

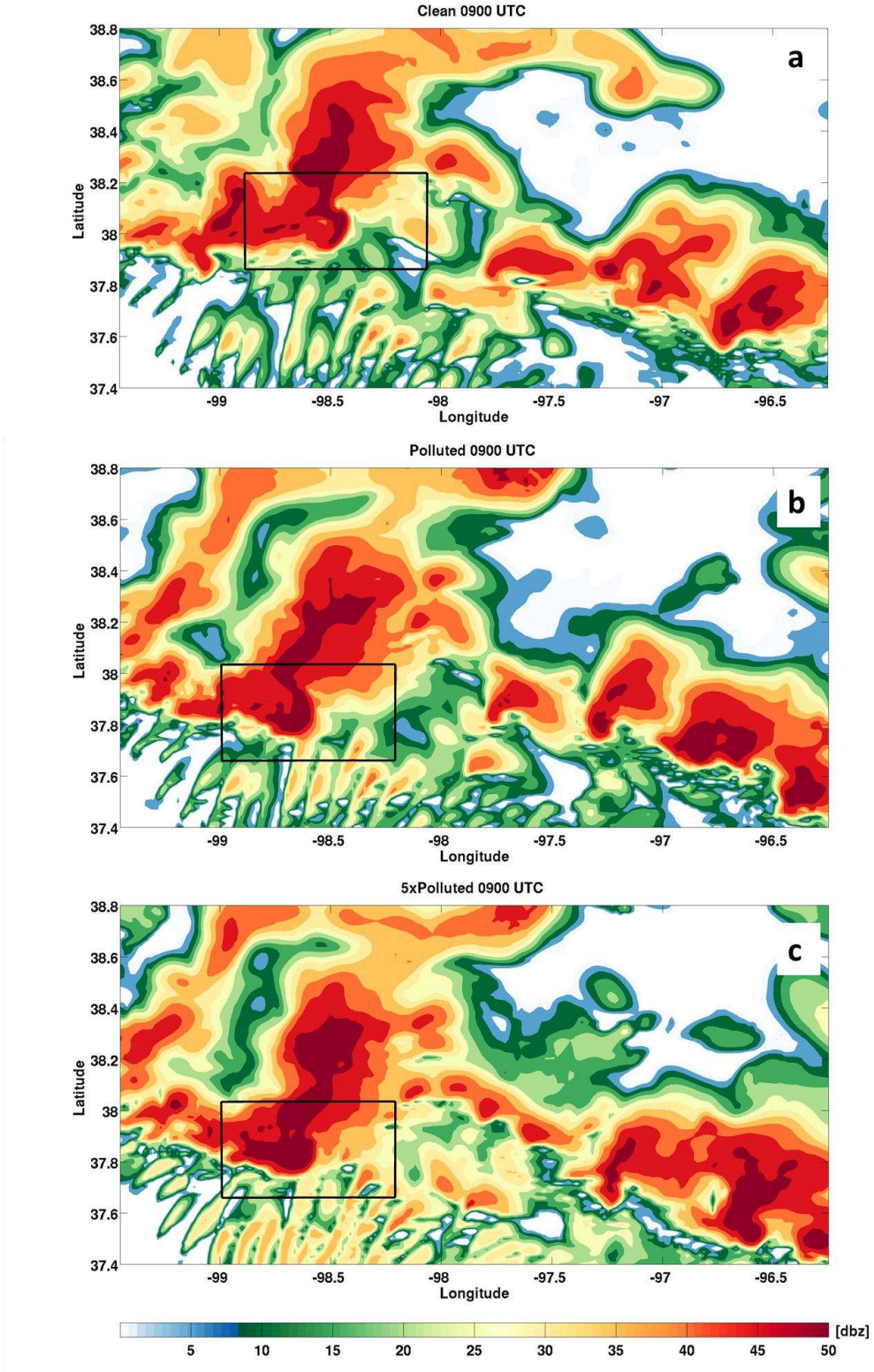

Figure 3.5: Simulated radar reflectivity at 1km (Seigel and van den Heever, 2013) at 0900 UTC for the three simulations: Clean (a), Polluted (b) and 5xPolluted (c). The analyzed region is enclosed within a black rectangle.

The regions enclosed in Figure 3.5 are enlarged in Figures 3.6a, Figure 3.7a and Figure 3.8a for the CLEAN, POLLUTED and 5xPOLLUTED simulations, respectively, and show the surface density potential temperature (shaded), area with DS winds (contoured in red) and the location of the back-trajectory (BT) parcel locations. Our BT airflow (Figure 3.6a, Figure 3.6b and Figure 3.7c) shows that the parcels within the area of the DS winds originated from two main upper-level flows: a descending RIJ and an up-down downdraft (UDD), however, their importance in the generation of the strong surface winds differs among the simulations. The importance of each flow to the generation of DS winds was determined by the fraction of the BT from near surface grid points with DS winds that followed each of the two flows. The dominant BT airflow in the CLEAN simulation was the RIJ (Figure 3.5c), which accelerated towards the leading convective line at higher elevations (~3000m AGL) in comparison with that of the RIJ within the POLLUTED (Figure 3.6c) and 5xPOLLUTED (Figure 3.7c) simulations. In the 5xPOLLUTED simulation (Figure 3.7c), the dominant flow consisted of air entering the storm on the downstream side of the storm. The air originated near the surface (consisting of the UDD) east (upstream) of the storm, slowly ascended with weak vertical velocities (~4-7 ms^{-1}) toward the leading convective cell, turning cyclonically following the mesovortex and then rapidly descending as the parcels encounter the precipitating downdraft on the upstream side of the convective updraft (Figure 3.7c). A third flow is apparent in the 5xPOLLUTED simulation which originated at 4 km AGL from the south-south west (similar to the midlevel downdraft branch described in Knupp, 1987). Within the POLLUTED simulation (Figure 3.6c), BT flow indicates that both the RIJ and the UDD contributed in the formation of the DS winds.

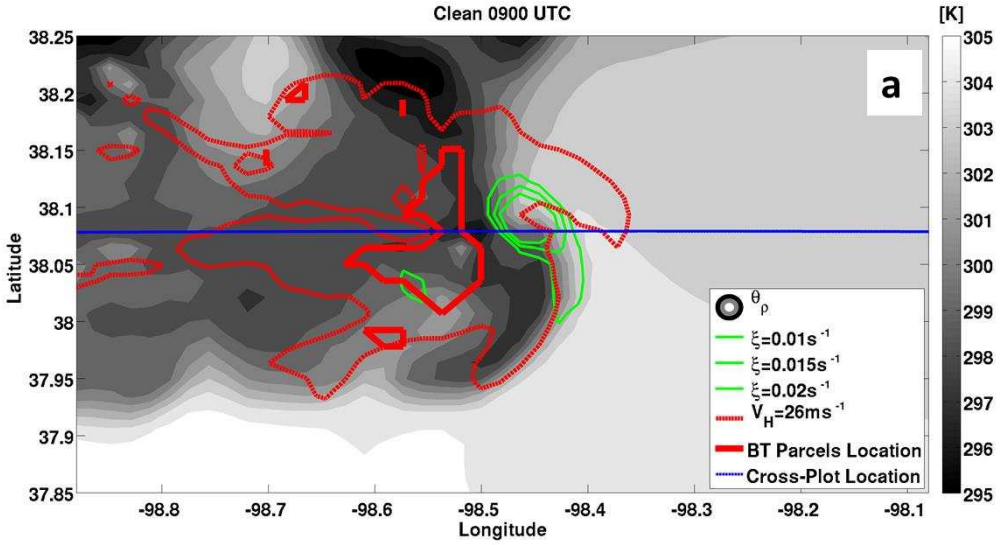
Clean 0900 UTC
[K]
a
Latitude
Longitude
θρ
ξ=0.01s-1
ξ=0.015s-1
ξ=0.02s-1
VH=26ms-1
BT Parcels Location
Cross-Plot Location

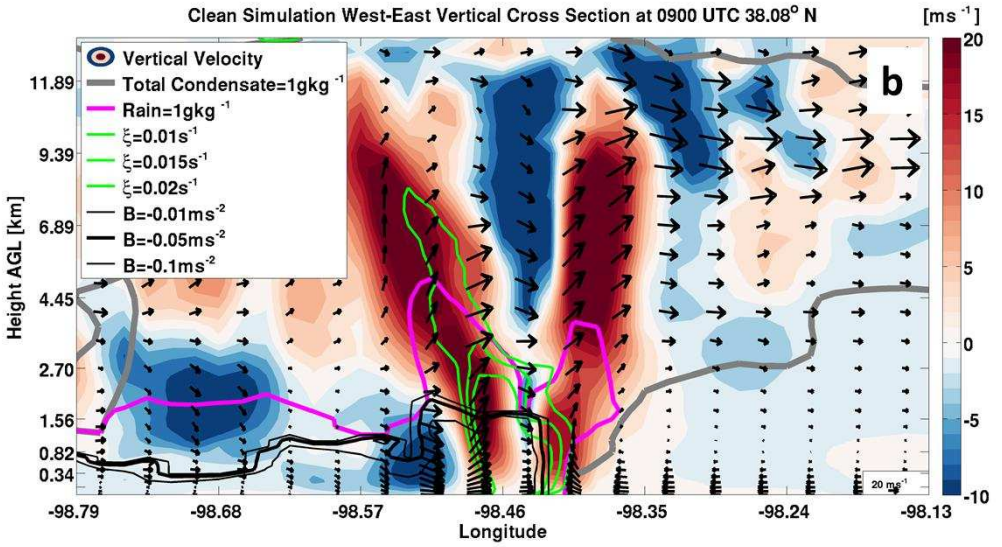
Clean Simulation West-East Vertical Cross Section at 0900 UTC 38.08° N
[ms-1]
b
Height AGL [km]
Longitude
Vertical Velocity
Total Condensate=1gkg-1
Rain=1gkg-1
ξ=0.01s-1
ξ=0.015s-1
ξ=0.02s-1
B=-0.01ms-2
B=-0.05ms-2
B=-0.1ms-2

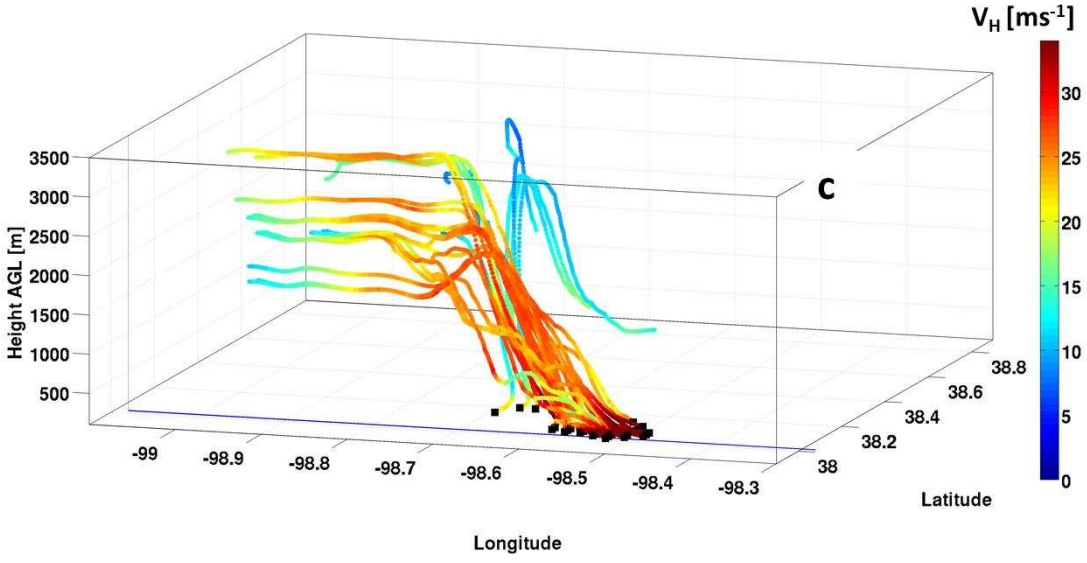
VH [ms-1]
c
Height AGL [m]
Longitude
Latitude

Figure 3.6: Clean simulation at 0900 UTC: (a) Surface density potential temperature $\theta\rho$ [K] (shaded) of the area enclosed by the black rectangle in figure 3.5a. Superimposed are contours of vertical relative vorticity at 1km AGL ($0.01s^{-1}$, $0.015s^{-1}$ and $0.02s^{-1}$ isopleths) representing the location of the mesovortex at the gust front (green lines). The area with DS winds is contoured in red and the region with the location of the back trajectories contoured in the thicker red line. The blue line across the figure presents the location of the cross plot within figure b. The location of this cross section was chosen as the mean location of the DS winds at the gust front. (b) Vertical cross section along the blue line shown in figure (a) of the vertical velocity [ms-1] (shaded), with the (u,w) wind vectors and the mesovortex represented in green contours of $0.01s^{-1}$, $0.015s^{-1}$ and $0.02s^{-1}$ relative vertical vorticity isopleths. The outline of the system is represented by the 1 g/kg contour of the total condensate (grey) and the precipitation by the 1 g/kg rain mixing ratio isopleth (magenta). The gust front is represented by the buoyancy value (B) of the cold pool contoured in black, as calculated according the density potential temperature. The edge of the cold pool is defined according to the isopleth of -0.05 $ms^{-}2$ (thicker black line), a value representative of mid-latitude cold pools (Seigel et al. 2013). Additional buoyancy value of -0.01 m s^{-2} and -0.1 m s^{-2} are also plotted to show the cold pool magnitude. (c) 30 minute back trajectories (a sample size of 30 - according to maximum parcel elevation) of the parcels within the region contoured in thicker red (figure a) and their relative location to the cross plot (figure b) (represented by the blue contour).The trajectories are color contoured according to the horizontal wind speed of the parcel along the trajectories. The vertical extent of the plot is 3500 meters AGL.

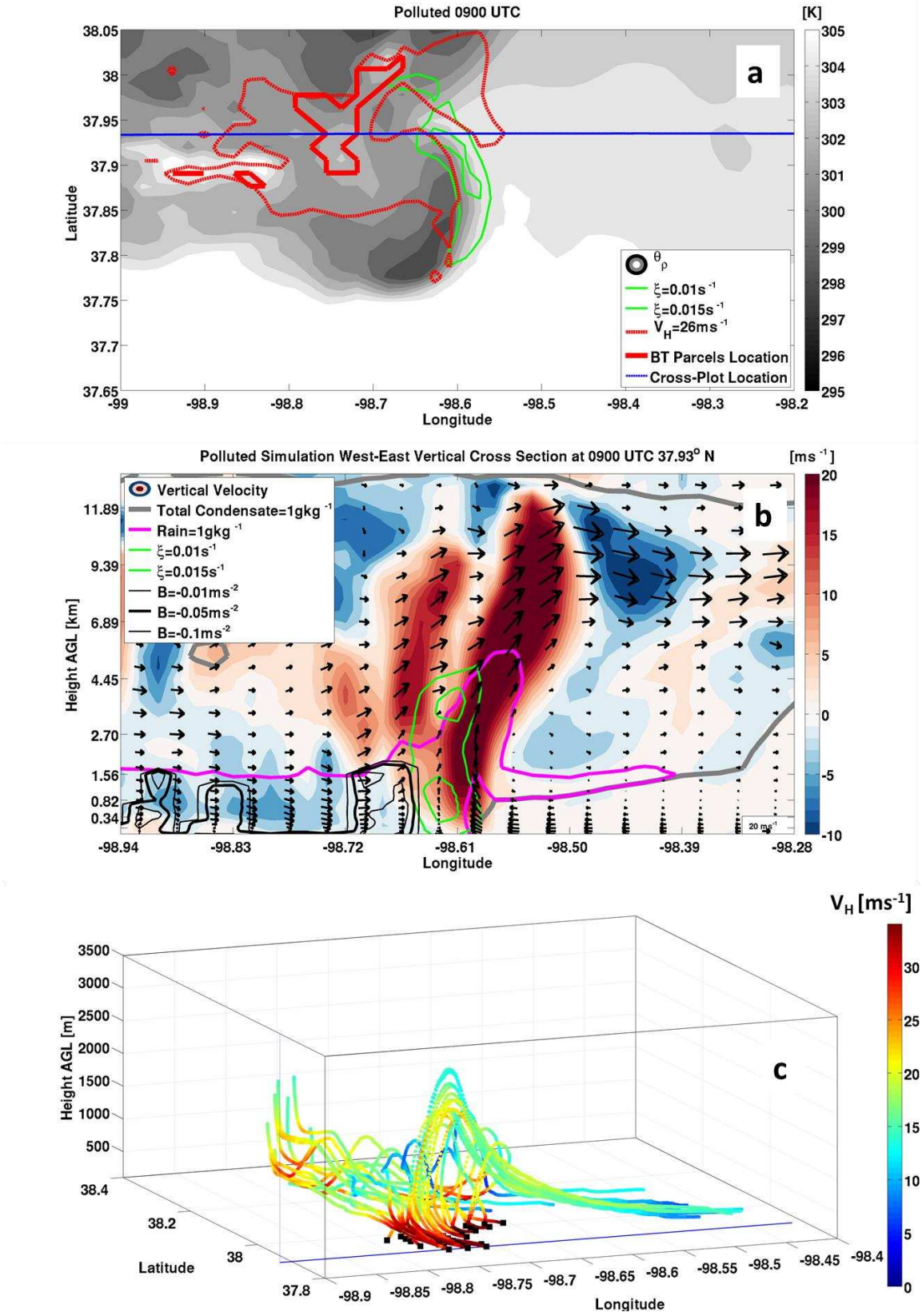

Figure 3.7: Same as Figure 3.6, for the Polluted simulation at 0900 UTC.

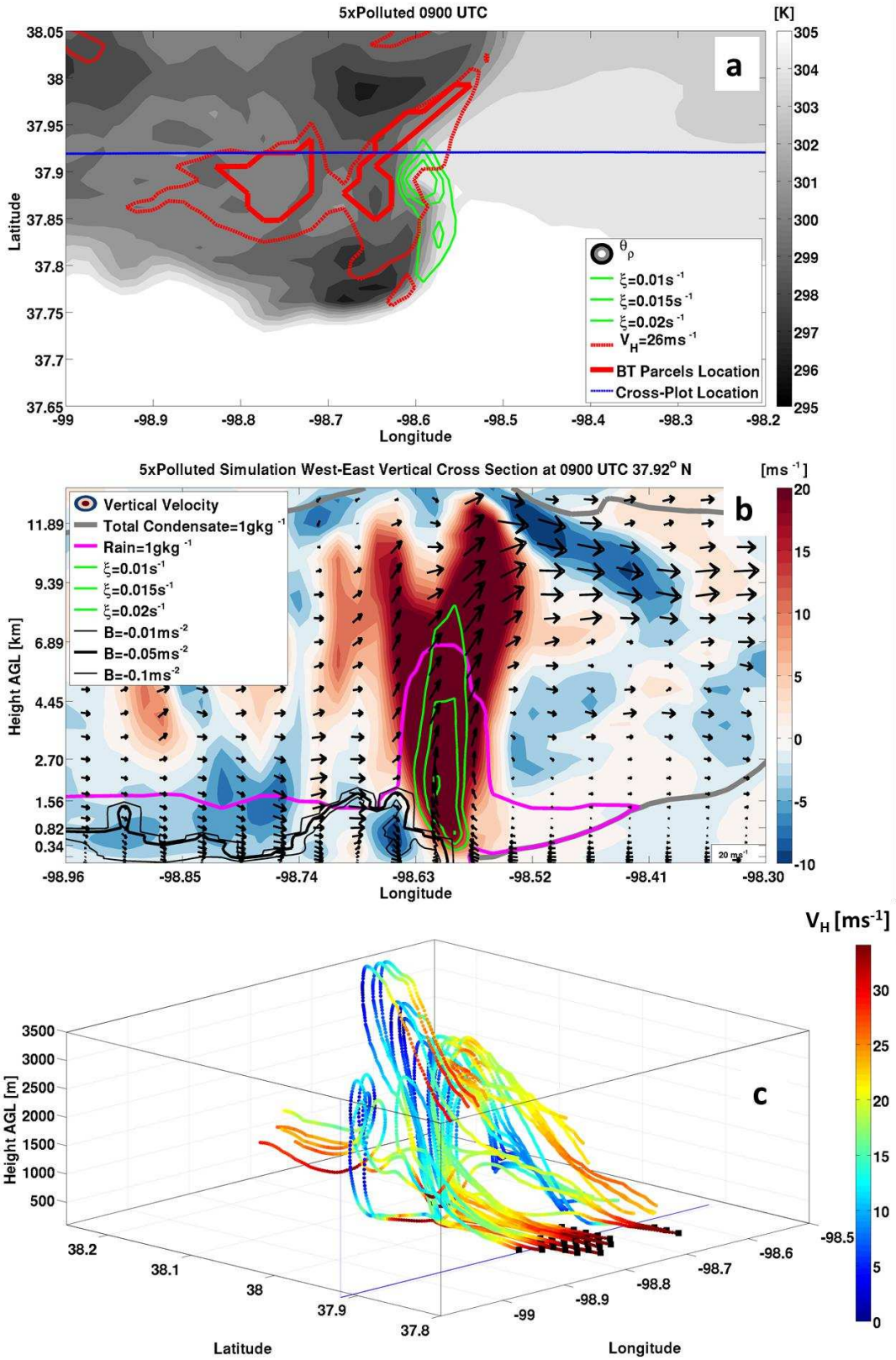

Figure 3.8: Same as Figure 3.6, for the 5xPolluted simulation at 0900 UTC.

The findings of air parcels sourced within the boundary layer contribution to the formation of DS following a trajectory of an UDD is consistent with previous findings (Knupp, 1987; Bernardet and Cotton, 1998). Bernardet and Cotton (1998) performed back trajectory analysis using a similar LM utilized in this study and found that the upward displacement of the parcels within the UDD trajectory was caused by an upward-directed perturbation-pressure gradient force (PGF) due to a midlevel meso-low or as part of a mesocyclone. A comparison between the BT flows among the three simulations is presented in Figure 3.9.

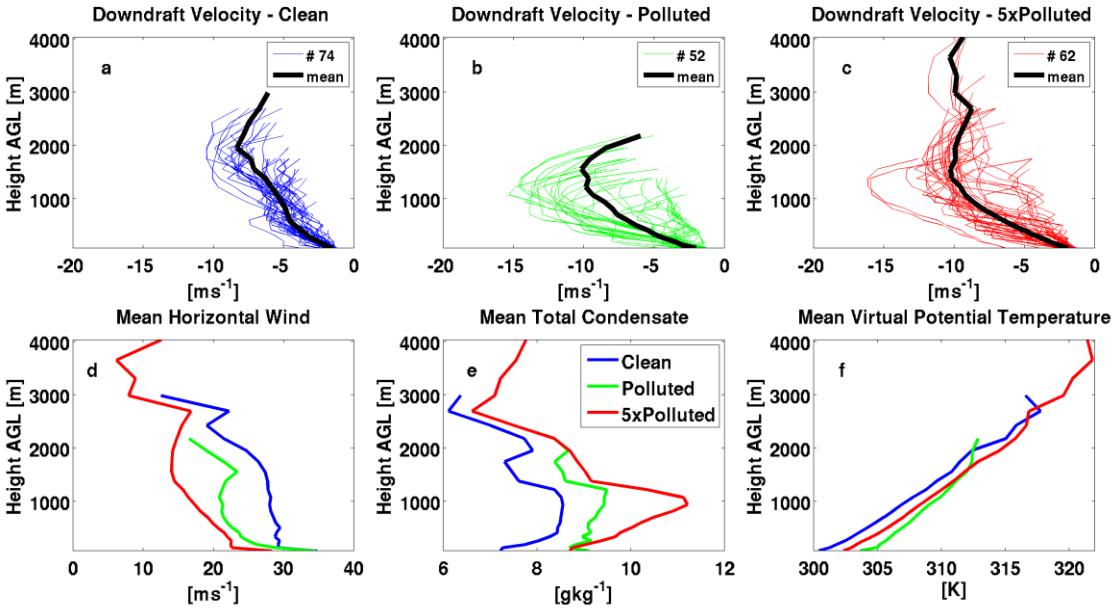

Figure 3.9: Downdraft vertical velocity as a function of height for individual descending parcels that follow either the RIJ or the UDD and the mean vertical velocity for the (a) Clean, (b) Polluted (c) and 5xPolluted back trajectory analysis. The number in parenthesis represents the number of BT parcels in each of the simulations. Mean characteristics of the descending parcels of horizontal wind speed [ms^{-1}] (d), condensate loading [gkg^{-1}] (e) and mean virtual potential temperature [K] (f) for the Clean (blue), Polluted (green) and 5xPolluted (red) simulations are plotted as a function of height for the downdraft trajectories.

Figure 3.9 shows that increasing the aerosol concentration led to a shift in the dominant BT flow from a prevalent RIJ in the CLEAN simulation, categorized by the stronger horizontal velocities at higher levels (Figure 3.9d) to a dominant UDD flow within the 5xPOLLUTED simulation, defined by stronger downdraft speeds (Figure 3.9c) which reach downburst intensities of greater than $-10ms^{-1}$ (Fujita, 1978).

The shift in the flow from the RIJ to UDD with increased aerosol pollution may be explained by the response of the convection orientation at the gust front to changes in the cold pool characteristics produced by the storm, following the RKW theory (Rotunno et al., 1988).
A RIJ forms when the main updraft is tilted upshear, forming a horizontal vorticity gradient between that of the cold pool and the tilted updraft (Weisman, 1992), as seen for the CLEAN simulation (Figure 3.6b). A UDD will form in association with the low pressure within a mesovortex (Bernardet and Cotton, 1997). A stronger mesovortex will develop when the horizontal vorticity generated by the cold pool is in balance with that of the environmental shear (Atkins and St. Laurent, 2009b), leading to a more upright updraft, as seen in the 5xPOLLUTED simulation (Figure 3.8b). Such a balanced state promotes the generation of relative vertical vorticity by the tilting of horizontal vorticity as well as by stretching of the vortex tube (Atkins and St. Laurent, 2009b).

An increase in aerosol concentration led to a non-monotonic trend within the cold pool temperature, as seen in the BT virtual potential temperature (Figure 3.9f) as well as the surface plots of the density potential temperature (Figures 3.5a, 3.6a and 3.7a). Changes in aerosol concentrations were found to alter the strength of the cold pool (both temperature and depth) due to the changes they induce in the precipitating hydrometeor characteristics. In part I, we found that at this time, higher aerosol concentrations enhanced both cold and warm rain formation in

the 5xPOLLUTED simulation and warm rain formation in the POLLUTED simulation, leading to the formation of larger raindrops near the surface in both cases. Therefore, changes in precipitation formation mechanisms impacted both the rates of evaporation and melting of the hydrometeors, which in turn, altered the cold pool strength. Due to the enhanced cold rain formation in the 5xPOLLUTED simulation, melting rates were the largest in that simulation, followed by the CLEAN simulation. However, the smaller raindrops within the CLEAN simulation increased the evaporation rates near the surface owing to their net increase in surface area thus producing a colder cold pool (van den Heever and Cotton, 2004). The downdrafts were the warmest in the POLLUTED simulation due to a decrease in evaporation, as seen in the near constant value of mean total condensate below 1 km AGL, indicating smaller amounts of total condensate loss within the downdraft in comparison to both CLEAN and 5xPOLLUTED (Figure 3.8e). This decrease in evaporation is explained by both larger raindrops in comparison to CLEAN as well as smaller rain rates in the POLLUTED case in comparison to the 5xPOLLUTED simulation. These changes in evaporation and melting led the cold pool to be the strongest in the CLEAN simulation followed by the 5xPOLLUTED simulation and the warmest in the POLLUTED simulation.

The orientation of the convection at the leading line shows that in the CLEAN simulation, for which the cold pool is the strongest, the updraft is tilted upshear which results in the BTs being predominantly from the RIJ (Figure 3.5b). For the 5xPOLLUTED simulation, the cold pool is slightly weaker in comparison to the CLEAN simulation, leading to a more upright convective updraft, which enhanced the intensity of the mesovortex. In the POLLUTED simulation, the cold pool was the weakest among the simulations at 0900 UTC, and the

convection at the leading line is seen to be tilted downshear, which limits the amount of vertical vorticity generated by stretching and produces a weaker mesovortex (Figure 3.7c).

Despite the weaker cold pool and the shallower mesovortex in the POLLUTED simulation, the downdraft speeds within the UDD were comparable to that of the 5xPOLLUTED simulation, emphasizing that the accelerations contributing to the stronger downdrafts occurred at lower levels below 2 km AGL, consistent with the characteristics of an UDD (Knupp, 1987). The shift of the BT flow from a RIJ (CLEAN) to a UDD associated with the mesovortex (5xPOLLUTED) explains why DS winds were stronger and occurred over a smaller region at 0900 UTC for the more polluted simulations and may explain the trend within the entire first period of the storm.

3.3.2. Simulated Derecho at 1500 UTC

After 1400 UTC, the convective region began to diminish and the MCS became dominated by stratiform precipitation (Figures 2.10 and 2.12), indicating the onset of MCS decay. During this time the area with DS winds also decreased. At 1500 UTC the region with DS surface winds encompassed the smallest area relative to the entire analysis period (Figure 3.3a) for both the CLEAN and POLLUTED simulations. During the first period (0630-0930 UTC) of the storm, a monotonic response occurred where an increase in aerosol concentrations produced stronger DS winds over a smaller region. In contrast, at 1500 UTC, the increase in aerosol concentrations led to a non-monotonic response in both DS strength and area. Relative to the CLEAN simulation, a moderate increase in aerosols (POLLUTED) decreased the DS wind area by 36% (Figure 3.3a) as well as the magnitude of the DS winds (Figure 3.3b and Figure 3.4c) while a greater increase in aerosol concentration (5xPOLLUTED) produced DS winds over an area 200% larger (Figure 3.3a) with similar DS wind intensity (Figure 3.3b and Figure 3.4c).

The location of the DS winds at 1500 UTC are presented in Figure 3.10 for the CLEAN (Figure 3.10a), POLLUTED (Figure 3.10b) and 5xPOLLUTED (Figure 3.10c), superimposed on the surface density potential temperature, which is representative of the location of the cold pool and hence the gust front. At this time, all three simulations produced DS winds in in close proximity to a mesovortex (outlined in green contours of relative vertical vorticity in Figure 3.10) at the leading edge of the gust front. The formation of a mesovortex at the gust front in this study is supported by observations in general (Weisman and Trapp, 2003), observations for the 8 May 2009 MCS in particular (Przybylinksi et al., 2010), and a recent numerical simulation of the MCS (Xu et al., 2015b). In addition, the simulated mesovortex produced in these simulations compare favorably to that presented in Xu et al. (2015b) both in location and time. Both the intensity of the mesovortex and area at 1500 UTC differ between the aerosol sensitivity simulations (Figure 3.10), which may explain the non-monotonic trend between aerosol concentration and the derecho winds at this time. The intensity of the mesovortex was compared among the simulations by examining the maximum relative vertical vorticity within the mesovortex (Figure 3.11a), identified as a 3D volume where values of vertical relative vorticity are at least $0.01s^{-1}$, in keeping with previous studies (e.g. Weisman and Trapp 2003). Within this volume, both the maximum updraft velocity and minimum perturbation Exener function were examine in Figure 3.11b and 3.11 c, respectfully.

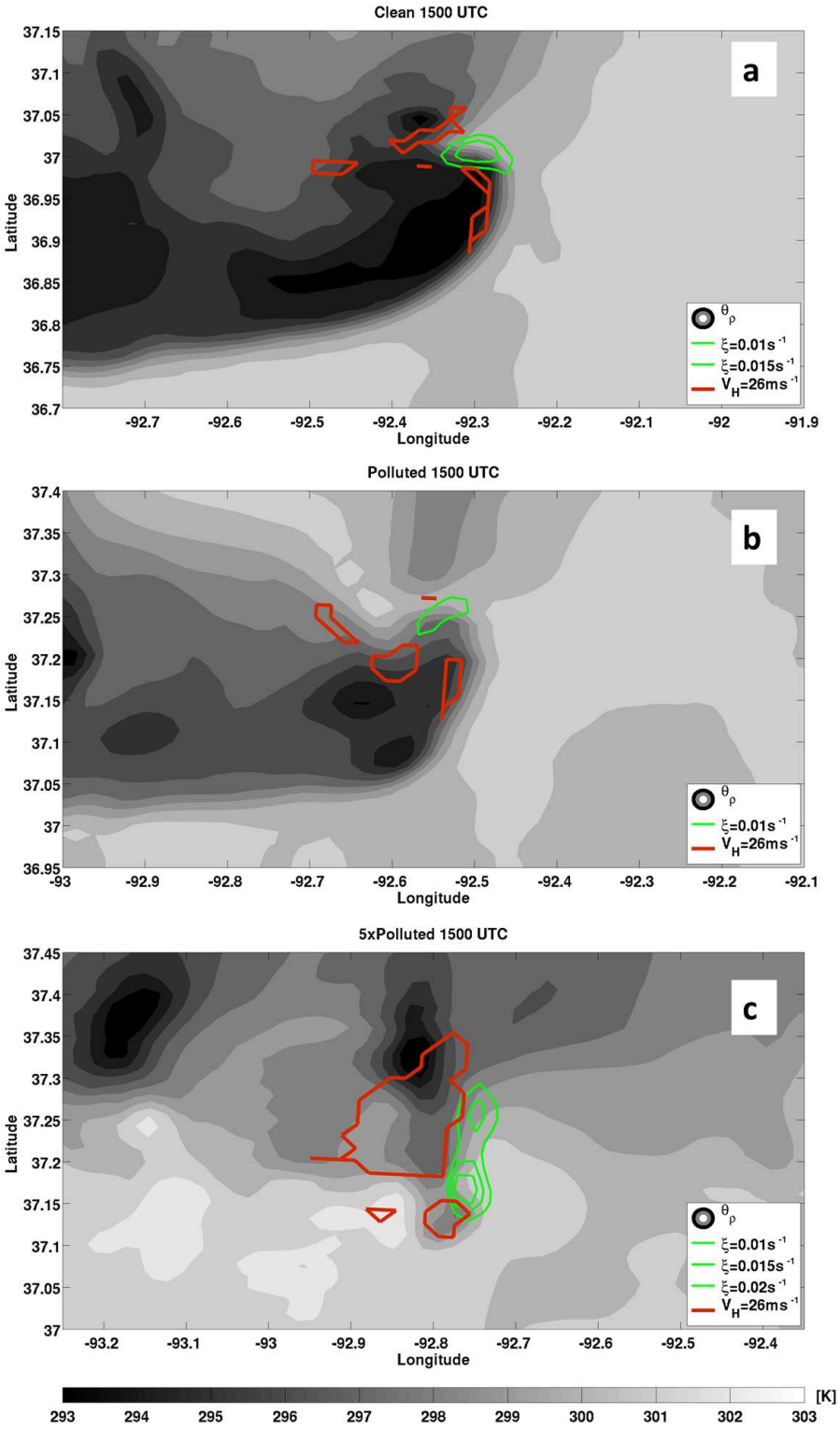

Figure 3.10: Surface density potential temperature (shaded), locations of DS winds (contoured in red) and the mesovortex at 1km AGL (contoured in green) are presented for the Clean (a), Polluted (b) and 5xPolluted (c) simulations at 1500 UTC.

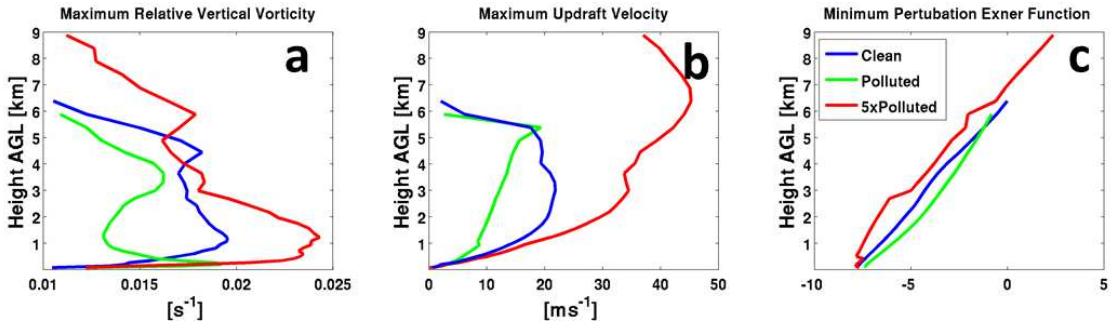

Figure 3.11: Characteristics of the Mesovortex (within a region of relative vertical vorticity greater than 0.01 s^{-1}(a) maximum relative vertical vorticity, (b) maximum updraft velocity and the (c) minimum Exner perturbation function with height for the three simulations: Clean (blue), Polluted (green) and 5xPolluted (red).

The strongest mesovortex (Figure 3.11a) occurred in the 5xPOLLUTED simulation, followed by the CLEAN, and the weakest mesovortex occurred in the POLLUTED simulation.

In general, changes in aerosol concentration affect the redistribution of latent heat within the storm and subsequently updraft speeds (Andreae et al., 2004; Khain et al., 2005; Koren et al., 2005; van den Heever et al., 2006; Li et al., 2008; Rosenfeld et al., 2008; Storer et al., 2010; Tao et al., 2012; Storer and van den Heever, 2013). Furthermore, changes in hydrometeor diameters impact the intensity of the storm generated cold pool (Li et al., 2009; Seigel et al., 2013; Lebo and Morrison, 2014) thereby potentially affecting the amount of baroclinically-generated horizontal vorticity which is made available to be tilted into the vertical (e.g van den Heever and Cotton 2004). Changes in aerosols may also impact the amount of vertical relative vorticity through their impacts on updraft speeds and in turn, vertical relative vorticity generated by stretching within a rotating updraft (Atkins and St. Laurent, 2009a). Here, the maximal relative vertical vorticity (Figure 3.11a) follows the same trend as the maximum vertical velocity (Figure 3.11b), therefore stretching might have contributed to the amplification of the relative

vertical vorticity. However, a dynamical feedback between the vertical relative vorticity and updraft speed may occur since a stronger mesovortex incurs stronger updrafts speeds as a rotating updraft experiences less entrainment (Snow, 1982). Furthermore, the cold pool environments of each of the mesovortices in each of the simulations were different in terms of density potential temperature (Figure 3.10). Therefore, differences in baroclinically-generated horizontal vorticity might also have played a role in explaining the nonlinear trend in mesovortex intensity. In order to understand how changes in aerosol concentrations led to the non-monotonic trend in the development of the mesovortices, vorticity budget analyses needs to be conducted which is beyond the scope of this study.

A stronger mesovortex can impact a derecho event by intensifying the flow within the RIJ (Schmidt and Cotton, 1989) as well as promoting the formation of an UDD (Bernardet and Cotton, 1998). The 3D trajectories of parcels which ascended to higher levels above the surface were plotted at 1500 UTC for the three simulations (Figure 3.12).

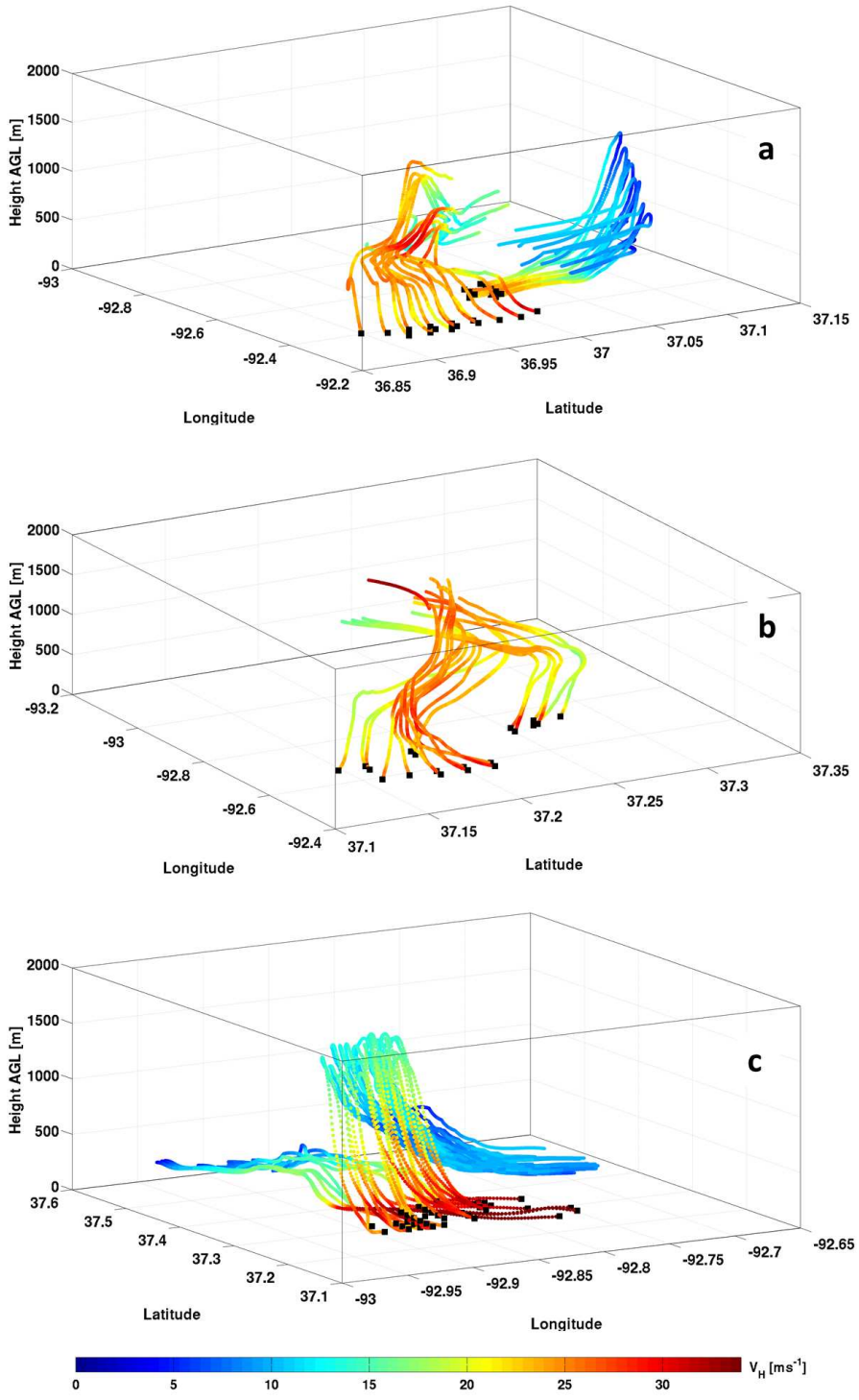

Figure 3.12: 1500 UTC sample 3D back-trajectory plots during 30 minutes for the (a) Clean, (b) Polluted and (c), 5x Polluted simulations. Trajectories are colored according to the parcel's horizontal wind speeds. Origins of the back-trajectories (at 1500 UTC, near the surface) are noted by the black square marker.

For both the CLEAN and 5xPOLLUTED simulations, two main BT flows are apparent: the RIJ and the UDD, while for the POLLUTED simulation, the BT flow only follows a RIJ. Comparisons among the characteristics of the RIJ in the three simulations are examined in Figure 3.11 featuring the mean values of RIJ height (3.11a), horizontal velocity (3.11b) and vertical velocity (3.11c) during the 10 minute BT analysis. Between the CLEAN and POLLUTED simulation, the RIJ was similar in both the intensity (3.11b), elevation (3.11a) as well as number of parcels following a RIJ flow. It is therefore hypothesized here that the smaller area of the DS winds in the POLLUTED simulation is explained by the fact that the mesovortex was not strong enough (Figure 3.11a) to force an UDD and hence this flow regime could not contribute to the DS winds at the surface.

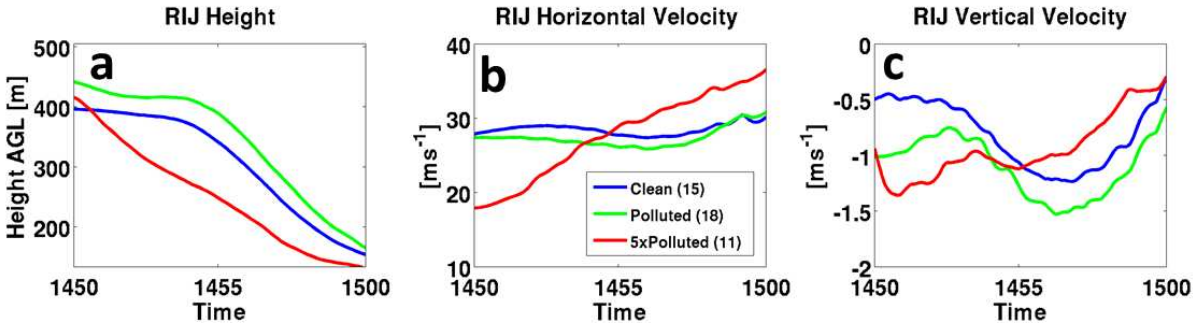

Figure 3.13: 1500 UTC mean back trajectory parcel characteristics of (a) height, (b) horizontal velocity and (c) vertical velocity for the Clean (blue), Polluted (green) and 5xPolluted (red) simulations during the last 10 minutes of the parcels descent. Numbers in the legend represent the number of parcels plotted.

The 5xPOLLUTED simulation also exhibited a RIJ, however descended faster to the surface due to the weaker cold pool (Figure 3.10c) which reduces the elevation of a RIJ (Weisman, 1992). However, unlike the CLEAN and POLLUTED simulations, the RIJ in the 5xPOLLUTED simulation occurred to the west of the elongated mesovortex (Figure 3.10c) and the parcels accelerated towards the low pressure below the mesovortex (Figure 3.12c).

The UDD flow characteristics between the CLEAN and 5xPOLLUTED simulations is further examined by comparing the horizontal wind speeds of the parcels as they descended to the surface following an UDD trajectory (Figure 3.14). In the 5xPOLLUTED simulation the parcels entered the mesovortex with higher horizontal velocity in association with the stronger vorticity (Figure 3.14b), turned cyclonically upon entering the precipitating downdraft and reached the surface with higher temperatures in comparison to the CLEAN simulation (not shown). Therefore, the acceleration of the parcels at higher levels contributed to the formation of DS winds at the surface indicating transfer of horizontal momentum from higher levels AGL to the surface. In contrast, in the CLEAN simulation, parcels entered the mesovortex at both lower altitudes and lower horizontal wind speeds (Figure 3.14a). The parcels accelerated to derecho-strength winds only after descending to the surface while experiencing higher evaporation rates (not shown).

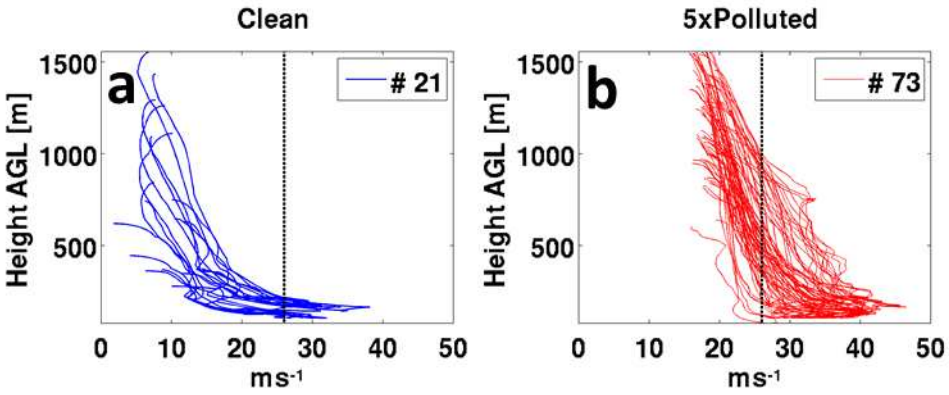

Figure 3.14: Horizontal wind speed of parcels during the decent following the UDD for the Clean (left) and 5xPolluted simulations (right). Numbers in the legend represent the number of parcels plotted. Dashed vertical line represents the threshold for DS winds ($26ms^{-1}$).

As was shown in Part I, the 5xPOLLUTED simulation produced larger rain droplets within the convective region at this time. These droplets evaporated less readily thereby enhancing the amount of precipitation reaching the surface and decreasing the evaporation potential. This also explains the weaker cold pool in the 5xPOLLUTED simulation (Figure 3.10c) and the stronger cold pool in the CLEAN simulation (Figure 3.10a).

UDDs associated with mesovortices are initiated by an upward pressure gradient perturbation due to the low pressure within the mesovortex (Bernardet and Cotton, 1998). However, within the 5xPOLLUTED simulation, the flow was found to horizontally accelerate as the parcels approached the mesovortex (Figure 3.14). The horizontal cross section of the perturbation Exner function within and around the region of the mesovortex is examined at several levels AGL for the three simulations (Figure 3.15). In RAMS, the perturbation Exner fields are calculated relative to a reference Exner profile which was determined according to the lowest grid point at sea level within the parent grid at the time of RAMS initialization (0000 UTC). The stronger mesovortex within the 5xPOLLUTED simulation was associated with a lower pressure perturbation and a larger horizontal perturbation pressure gradient at higher levels, which explains why the flow within the 5xPOLLUTED simulation horizontally accelerated as it approached the mesovortex. The horizontal pressure gradients were weaker in the CLEAN simulation, thereby explaining why the parcels entered the mesovortex at lower horizontal speeds. The weaker mesovotex within the POLLUTED simulation and the associated higher perturbation pressures explains why DS winds were not produced following an UDD flow.

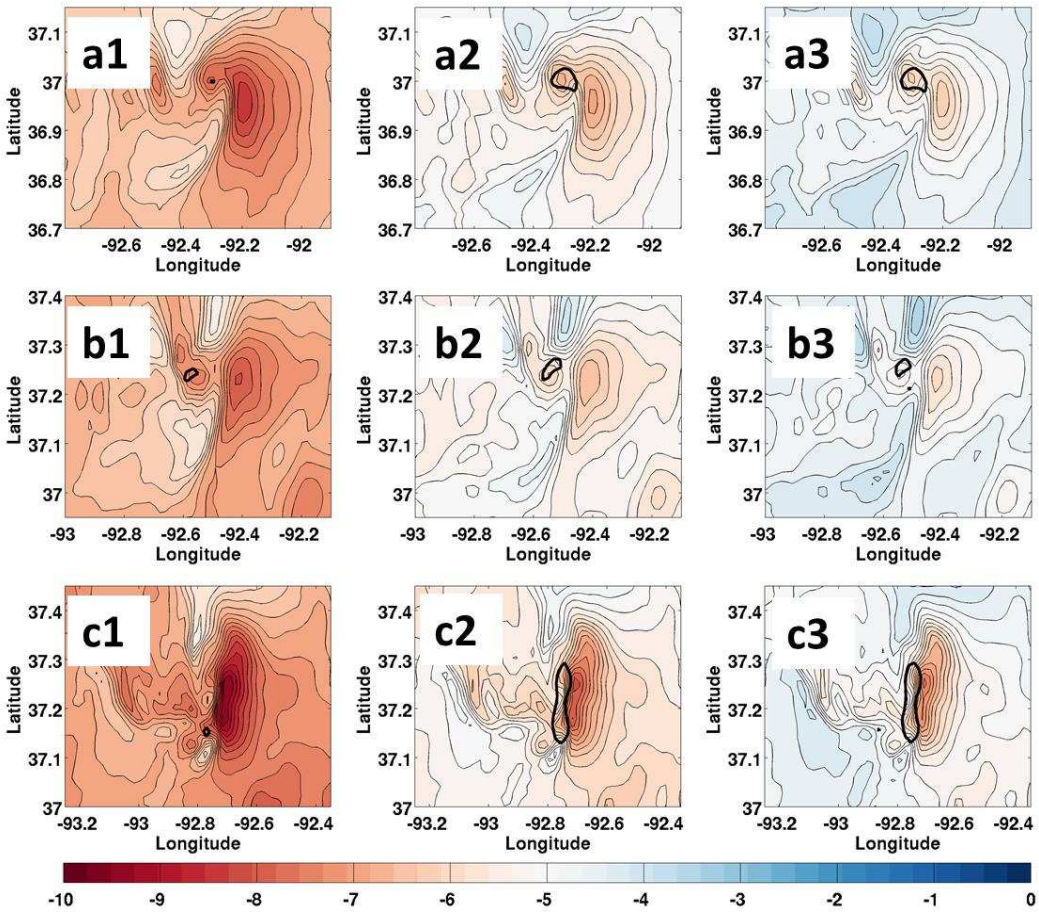

Figure 3.15: Perturbation Exner function (shaded) and isopleth of 0.01 s^{-2} (black contour) at the surface (left column), 1 km AGL (middle column) and 1.5km AGL (right column) for the three simulations: Clean (top row), Polluted (middle row) and 5xPolluted (bottom row) at 1500 UTC of the areas presented in Figure 3.10.

3.5. Discussion

The sensitivity of the simulated 8 May 2009 derecho to aerosol loading has been investigated by performing a numerical analysis of aerosol loading on an MCS. Due to the complex nature of the dynamics of an MCS, identifying the impact of increased aerosols on the strength of the convective outflow is challenging. This is because aerosols serving as CCN can modify the strength of a derecho (1) directly by modifying the intensity of the downdrafts through evaporative and/or melting effects; (2) indirectly by modifying the relationship between the horizontal vorticity generated in association with the environmental shear and that baroclinically-generated by the storm-produced cold pool; and (3) through impacts on the strength of the mesovortex due to changes in vertical relative vorticity attributed to the amount of baroclinically generated horizontal relative vorticity and stretching by the convective updraft. Previous numerical studies have shown that mesoscale storm dynamics and longevity are sensitive to changes in ice hydrometeor diameters through the changes in melting and evaporation rates, and thus, the strength of the storm-produced cold pool. van den Heever and Cotton (2004) found that decreasing hail diameter sizes increased cold pool strength due to an increase in melting and subsequent evaporation. Smaller hail hydrometeors increase the melting potential due to smaller terminal fall speeds and an increase in the integrated surface area exposed to melting. Similarly, Adams-Selin et al. (2013) found cold pool intensity to vary as a function of graupel size and density. Both studies demonstrated that smaller ice hydrometeors led to stronger cold pools. In Part I of this study, increases in aerosol concentration were found to produce larger rain drops and hail stones which contributed to an enhancement in the amount of convective precipitation produced by the storm. The smaller rain and hail diameters within the CLEAN simulation produces the stronger cold pools found in Part II of this study. However, the

strength of the cold pool was found to be sensitivity to both the size of the precipitating hydrometers as well as precipitation rates. Earlier in the storm's life, the strongest cold pool was found in the CLEAN simulation followed by the 5xPOLLUTED simulation and the weakest was found in the POLLUTED simulation. This was attributed to higher rain rates in the 5xPOLLUTED simulation which yielded more mass available to be melted and evaporated. Later in the storm's life, when the differences in the convective rain rates decreased among the simulations, a monotonic trend was found were increased aerosol concentration formed weaker cold pool due decrease in evaporation and melting of the larger precipitating hydrometers.

Changes in the cold pool strength impacts the formation of the RIJ (Weisman 1992), as well as the strength of gust front induced mesovortices (Atkins and St. Laurent, 2009b). A stronger mesovortex can potentially amplify the updraft strength as a rotating updraft experiences less entrainment (Snow, 1982), thereby allowing for greater condensation rates, larger amounts of supercooled water transported aloft and thus enhancing latent heat release and further enhancing the convective updraft, illustrating the dynamical feedback complexity of organized convection.

In order to understand the impact of aerosol loading on the simulated derecho, back trajectory analysis from the locations with strong surface winds were performed for all three of the simulations during different stages of the simulated MCS. Two main air flows were found to contribute to the formation of the DS winds: (1) the rear inflow jet (RIJ) and (2) strong downdrafts following an up-down downdraft trajectory. The findings that the DS winds were generated by both a RIJ and flow associated with a mesovortex is consistent with previous studies (Atkins and St. Laurent, 2009b). A schematic of the 3D flow driving the DS winds within the simulated 8 May 2009 derecho event is presented in Figure 3.16.

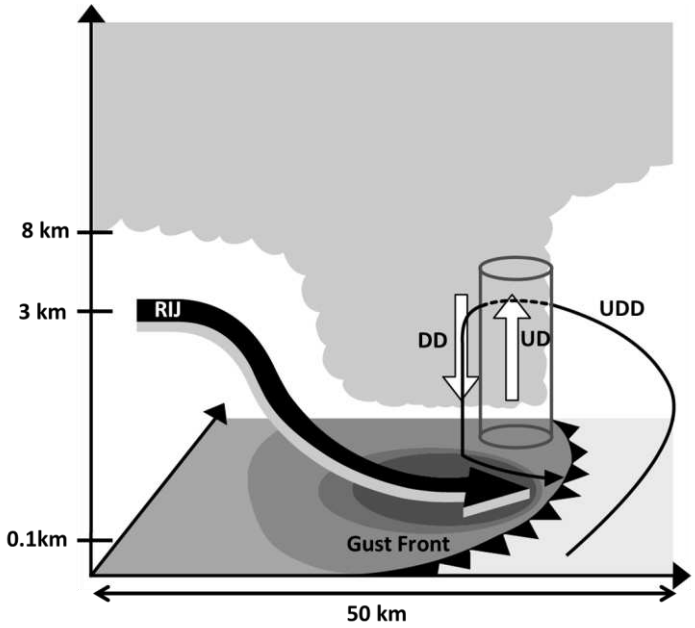

Figure 3.16: Schematic depiction summarizing the 3D flow of the Rear-Inflow Jet (RIJ) and Up-down downdraft (UDD), the mesovortex at the gust relative to the location of the cold pool (shaded in the X-Y plan) and gust front, the convective updraft (UD) and precipitating convective downdraft (DD).

Figure 3.16 illustrates the 3D flow close to the gust front (within 50 km) derived from the back-trajectory analysis presented here in Figures 3.6c,3.7c,3.8c and 3.12. The flow following the up-down downdrafts reaches the surface south of the mesovortex, consistent with the findings of Atkins and St. Laurent (2009b). It is important to note that the RIJ captured in the 60 minute back trajectory flow is focused near (~50 km) the convective line and does not include the entire flow of the RIJ which extends several hundred kilometers behind the convective line, as seen in Johnson and Hamilton (1988).

As in Part I, a time dependent signal was found between the derecho strength and aerosol loading due to the dynamics which produced the derecho event. During the developmental stage of MCS, the cold pool was the strongest in all three aerosol sensitivity simulations. The aerosol-

induced changes in the precipitation formation shown in Part I impacted the balance between the horizontal vorticity generated by the cold pool and that of the low-level environmental wind shear predicted by RKW-theory (Rotunno et al., 1988). In this study, this balance was found to be sensitive to aerosols loading through the impact on cold pool strength, which in turn, modified the predominant flow which produced the DS winds at the surface from a descending RIJ (in the CLEAN simulation) to an up-down downdraft (in the 5xPOLLUTED simulation). In the latter case, the weaker cold pool was associated with a more upright oriented convective updraft, and thus stronger mesovortex.

As the storm matured, changes in aerosol concentration impacted the formation of the mesovortex. It is hypothesized here that the change in the mesovortex intensity among the simulations is attributed to the amount of baroclinically-generated horizontal relative vorticity at lower levels in association with variations in cold pool strength. This horizontal vorticity is then tilted into the vertical. Furthermore, enhanced aerosol concentrations impact the amount of latent heat release within the convective updraft, thereby altering the amount of vertical relative vorticity generated by stretching.

The environment of the 8 May 2009 was unique, especially in regards to the amount of moisture available. Larger aerosol concentrations in a drier environment have been found to decrease the amount of precipitation produced by an MCS (Khain et al. 2005; Tao et al. 2007). It is hypothesized here that in a drier environment, the higher aerosol concentration in the 5xPOLLUTED simulation would have increased cloud droplet evaporation aloft and may not have produced the strong downdrafts due to condensate loading and melting which made the up-down downdraft so prolific in producing derecho-strength winds.

3.6. Conclusions

The microphysical effects of increased aerosol concentrations on the characteristics and intensity of a derecho were examined in this study by performing a numerical analysis of an MCS case study using a mesoscale cloud resolving model, RAMS. The case study chosen was the 8 May 2009 "Super-derecho" MCS. A set of three RAMS sensitivity simulations was conducted: CLEAN, POLLUTED and 5xPOLLUTED, in which the aerosol distribution, concentration and chemical composition differed based on the output of a 3D chemical model, GEOS-Chem. The CLEAN simulation contained only aerosol concentrations from non-anthropogenic sources, the POLLUTED of aerosols from both anthropogenic and non-anthropogenic sources and the 5xPOLLUTED the same distribution as in the POLLUTED simulation, but multiplied by a factor of five. Back trajectory analysis from grid points with derecho winds were performed for two periods within the storm, the initial and onset dissipation. Analysis of the sensitivity of the simulated derecho event to changes in aerosol concentration shows the following:

- Changes in aerosol concentrations did not impact the MCS longevity, propagation speed or direction, total precipitation or the formation of the derecho, however it did impact the distribution of convective vs stratiform precipitation (Part 1) and the derecho characteristics (intensity and area).
- Two main flows were found to produce the derecho event: a rear inflow jet (RIJ) and an up-down downdraft (UDD) associated with a mesovortex at the gust front.
- Aerosols acting as CCN were found to impact the derecho intensity directly by modifying the cold pool strength and downdraft speeds, and indirectly by altering the balance

between the horizontal vorticity generated by the cold pool and that of the environment, as well as the formation of the mesovotex at the gust front.

- Early in the MCS lifecycle, an increase in aerosol concentration resulted in a shift in the flow regime from being dominated by the RIJ to being predominately from a downburst following a pathway of an up-down downdraft, which exhibited stronger surface winds speeds over a smaller area.
- Later in the MCS lifecycle, the RIJ was similar within the aerosol sensitivity simulations and the changes in the derecho event were attributed to the up-down downdraft associated with the mesovortex. At this time, acceleration within the up-down downdraft in the highly polluted simulation was attributed to enhanced horizontal acceleration at higher altitudes as the flow approached the stronger mesovortex. Within the cleaner simulation, the flow was accelerated nearer the surface due to higher evaporation rates of hydrometeors. The mesovortex at this time was the weakest within the moderately polluted simulation and did not produce an up-down downdraft which could contribute to derecho-strength winds at the surface.

The findings of study are limited to this environment of this case study which included a strong LLJ and anomalously high PW values which supported invigoration of convective precipitation with increased aerosol concentration. The non-monotonic trends found in this study in the derecho characteristics to increased aerosol concentrations should be examined for other case studies with varying humidity.

4. Concluding Remarks

4.1. Summary

This dissertation describes a numerical analysis of a simulated case study MCS's sensitivity to changes in anthropogenic aerosol concentration using the Regional Atmospheric Modeling System (RAMS). The case study selected for this research was the 8 May 2009 "Super-Derecho" MCS, which produced both large amounts of precipitation as well as a derecho wind event. The dissertation is divided into two parts, Part I and Part II, which examined the sensitivity of the simulated MCS-produced precipitation and derecho characteristic's to increased anthropogenic aerosol concentrations, respectively. In order to represent a more realistic spatial distribution of aerosols in RAMS, aerosol concentrations from the 3D chemistry transport model, GEOS-Chem, were incorporated into RAMS. Twelve species from the GEOS-Chem model with varying hygroscopicity were incorporated as three different internally mixed aerosol groups based on the aerosol's hygroscopicity: hygroscopic, hydrophilic and hydrophobic aerosols. The grouping of the twelve aerosol species into three groups was motivated by reducing the RAMS computation time while still representing the varying nucleation potential of different aerosols types. Aerosol data from two GEOS-Chem simulations were used in this study. The first contained aerosols from natural sources and the second included both natural and anthropogenic sources. Three RAMS simulations were conducted, which differed only in their initial aerosol concentration and distribution from the GEOS-Chem aerosol data output. The first RAMS simulation "CLEAN" consisted of GEOS-Chem aerosols from natural resources only. The second RAMS simulation "POLLUTED" was initialized with GEOS-Chem aerosols from both natural and anthropogenic sources. The third simulation "5xPOLLUTED" was initialized with the GEOS-Chem aerosols from both sources, multiplied by a factor of five. This set up allowed

for the investigation of the impacts of anthropogenic aerosols and increased anthropogenic aerosols on a case study MCS.

In part I the impact of changes in aerosol concentrations on precipitation formation processes was analyzed by examining the distribution and characteristics of the different liquid and ice phase hydrometeors and their effects on the precipitation formation processes. Specifically, the study examined how changes in aerosol concentrations serving as potential CCN impacted the convective and stratiform-anvil regions of the MCS. Furthermore, the sensitivity of precipitation formation to aerosols was examined by comparing warm-rain and cold-rain production processes among the three simulations. A Lagrangian trajectory model was used in order to determine the air flow sources within the MCS's stratiform-anvil. This was done in order to analyze the impact of higher aerosol concentrations on the different airflows and in turn, to determine how aerosols impacted the stratiform precipitation.

In part II, the derecho characteristics of the simulated MCS were examined. The intensity of the derecho was determined according to both the near-surface wind speed as well as the area with derecho intensity winds. In order to understand the impact of changes in aerosol concentrations on these characteristics, first the dynamical pathway generating the derecho intensity winds was examined. Back-trajectory analysis using a Lagrangian trajectory model was performed for two different periods of the storm: genesis and dissipation. The back-trajectory analysis was performed from grid points near the surface with derecho strength winds. Once the different flows were identified, they were compared among the aerosol simulations in order to examine the sensitivity of these dynamical pathways to aerosol loading in the generation of strong surface winds.

Part I of this study adds to the current body of work outlining aerosol impacts on MCS precipitation by examining the impact of aerosols in a heterogeneous model framework and taking into account 12 different species of aerosols. Part II of this study offers the first evaluation of the impacts of aerosol concentration on the intensity and characteristics of surface winds of a derecho-producing MCS.

4.2. Main Conclusions

Increasing the concentration of aerosols serving as potential CCN within the simulated case study MCS did not substantially affect the storm's longevity, the amount of total precipitation produced by the storm, or the occurrence of the derecho event. However, changes in aerosol concentrations did modify the characteristics of both the precipitation and the severe wind event produced by the simulated MCS.

In Part I, it was found that the total domain precipitation was not significantly affected by aerosol pollution. Nonetheless, aerosol pollution enhanced precipitation in the convective region while suppressing precipitation from the stratiform-anvil. In the convective region, enhanced updrafts in the polluted simulations condensed more cloud water and transported greater amounts of supercooled cloud water to higher levels which enhanced collision-coalescence and riming rates. Therefore, the more polluted simulations yielded fewer yet larger raindrops and hailstones which reduced evaporation at lower levels, thereby enhancing the convective precipitation. Even though increased aerosol concentration reduced the collision coalescence efficiency between cloud droplets, precipitation was enhanced due to a higher collection efficiency of cloud droplets by rain and hail. The latter was attributed to fewer collecting hydrometeors with a larger number of cloud droplets available to be collected.

The increased convective precipitation in the polluted simulations was found to be time-dependent due to the changing environment of the MCS. During the genesis and mature stage of the MCS, a strong and deep Low Level Jet (LLJ) was present, supplying the storm with large amounts of moisture which reduced the competition for vapor to condense onto the larger concentrations of aerosols. Within the polluted simulations, the increase in convective precipitation occurred primarily during the genesis and mature stage of the MCS. Later in the storm, in the 5xPOLLUTED simulation, the enhanced warm-rain precipitation depleted cloud water content aloft, thereby decreasing riming efficiency.

During the majority of the analysis period, the greater aerosol concentrations reduced precipitation formation within the stratifrom-anvil. Back trajectory analysis showed that air feeding the stratiform-anvil came from two main airflows: (1) outflow from the convective cells, where air originated in the boundary layer and (2) slantwise slow ascending flow which originated in the free troposphere. In the polluted simulations, outflow of smaller ice particles from the convective cores into the stratiform-anvil, as well as the nucleation of smaller more numerous cloud droplets within the slow ascending updrafts, reduced both collision coalescence and riming within the stratiform-anvil region. As a consequence, the more polluted simulations produced the smallest precipitation from the stratiform-anvil.

In Part II, the impacts of aerosols on the derecho, or severe surface winds, were examined. Back trajectory analysis from points with strong surface winds was performed for all three of the simulations during two different stages of the simulated MCS. As in Part I, a time dependent signal of derecho wind characteristics to aerosol loading was found due to the dynamics which produced the derecho event. During the developmental stage of the MCS, the cold pool was the strongest in all three simulations and the changes in the precipitation formation

found in part I, modified the strength of the storm-produced cold pool. This in turn impacted the balance between the horizontal vorticity generated by the cold pool to that generated by the vertical wind shear of the environment. This balance, known as RKW theory (Rotunno et al, 1988), affects both convective intensity and the formation of a rear inflow jet (Weisman, 1992). The strongest cold pool formed in the simulation with no anthropogenic aerosols (CLEAN) due to enhanced melting and evaporation of the precipitation hydrometeors. The stronger cold pool led to an upshear tilt of the leading convective line, following the RKW theory. In the higher aerosol concentration simulation (5xPOLLUTED), a weaker cold pool promoted a more upright convection at the gust front. At this time, a moderate increase in aerosols (POLLUTED) formed the weakest cold pool due to a decrease in rain rates in comparison to the 5xPOLLUTED simulation and lower evaporation rates, in comparison to CLEAN. This led to the convective updraft to tilt downshear, following the RKW theory. Parcel back-trajectory analysis demonstrated that the orientation of the convection at the leading line shifted the dominant flow which formed the derecho winds at the surface. Within the CLEAN simulation, due to the upshear tilt of the convection, the primary flow was attributed to a descending RIJ. Within the 5xPOLLUTED simulation, due to an upright convective updraft, a stronger mesovortex formed and the primary flow followed an up-down downdraft. In the POLLUTED simulation, where the convective updraft was tilted downshear, both the up-down downdraft and the RIJ contributed to the formation of the derecho-strength winds at the surface. Trajectories following the path of the up-down downdraft produced stronger surface winds over a smaller region, while a stronger RIJ and cold pool produced slightly weaker winds but over a much larger area. These findings explain the monotonic relationship at this time between higher aerosol concentrations and stronger surface winds over a smaller area.

As the MCS matured, the cold pools weakened in all the simulations, and the formation of the strong derecho winds was found to be associated with the formation of mesovortices. During this time, a non-monotonic response of increased aerosol concentration and the derecho strength was found where within the 5xPOLLUTED simulation, the area with the derecho winds was larger while the area in the POLLUTED simulation was smaller in comparison with the CLEAN simulation. All three simulation's back-trajectories show that the parcel flow which generated the derecho winds was produced by a descending RIJ. Therefore, the non-monotonic trend in the derecho event at this time was attributed to the non-monotonic trend in the mesovortex intensity which impacted the formation of an up-down downdraft. The strongest mesovortex formed in the most polluted simulation, while the simulation with the least amount of aerosol concentration exhibited a weaker mesovortex. In the POLLUTED simulation, the mesovortex was the weakest amongst the three simulations. Therefore, only within the CLEAN and 5xPOLLUTED simulation back-trajectory flow follow an up-down downdraft path in association with the stronger mesovortices, in comparison with the POLLUTED simulation. Between the CLEAN and 5xPOLLUTED simulation, the mesovortex in the 5xPOLLUTED simulation was stronger, however both simulations produced similar wind speeds at the surface, which is attributed to horizontal accelerations of the parcels at different levels from different dynamical contributions. In the 5xPOLLUTED simulation, due to the stronger mesovortex and thus larger horizontal pressure gradients, the parcels entered the mesovortex with higher horizontal velocity, turned cyclonically upon entering the precipitating downdraft and reached the surface at higher temperatures in comparison to the CLEAN simulation. Therefore, the transfer of horizontal momentum enhanced the surface wind speeds in the 5xPOLLUTED simulation. In contrast, in the CLEAN simulation, parcels entered the mesovortex at both lower

altitudes and lower horizontal wind speeds. The parcels accelerated to derecho-strength winds only after descending to the surface while experiencing higher evaporation rates. The POLLUTED simulation exhibited neither.

Changes in aerosol concentration affect the redistribution of latent heat within the storm thereby potentially affecting the amount of baroclinically-generated horizontal vorticity which is available to be tilted into the vertical. Furthermore, convective invigoration in the polluted simulations was also found to changes in updraft velocities thereby increasing the vertical vorticity generated by stretching within the rotating updraft. The environments of each of the developing mesovortices were found to be different in terms of density potential temperature due to the impacts of aerosols on the intensity of the cold pool as well as evaporation and melting of stratiform precipitation. The cold pool influenced generation of baroclinic vorticity played a role in altering the intensity of the mesovotices in these simulations. The findings here suggest that changes in aerosol concentrations impact the formation and strength of mesovortices within an MCS.

4.3. Future Work

It was shown in this dissertation that changes in aerosol concentrations can impact the characteristics of both precipitation and a derecho wind event directly by modifying precipitation formation processes and indirectly by altering the dynamical balances within the storm. However, in this study, the GEOS-Chem aerosols were not radiatively active and primarily served as CCN. Past studies have shown that aerosol impacts on precipitation produced by an MCS may be buffered due to the direct effect of increased aerosol concentration (e.g Rosenfeld et al., 2008; Tao et al., 2012) and the presence of dust acting as both GCCN and IN (e.g Li et al.,

2009; Seigel et al., 2013), which can alter the precipitation formation mechanisms within an MCS. It would be of interest to examine the effects of enhanced anthropogenic aerosol concentrations on the precipitation of the 8 May 2009 MCS when dust is present and may serve as GCCN, CCN and IN. Furthermore, aerosols have a direct radiative forcing because they scatter and absorb solar and infrared radiation in the atmosphere. Therefore, higher aerosol concentrations can introduce changes in diabatic heating, and modify both warm-rain and cold-rain processes, primarily due to the effect on vertical velocity and supersaturation. Although MCSs are typically nocturnal, some MCSs form during the day, such as the June 29th MCS which produced a derecho event over Ohio Valley. In this case study, the MCS persisted after sunrise, and the direct effect of aerosols may therefore potentially impact the storm. For this reason, the effects of increased aerosol concentrations which are both radiatively active as well as serve as CCN should be investigated in order to examine a possible buffering effect, as seen in previous studies (e.g Seigel et al. 2013).

The question of the effects of greater anthropogenic aerosols could be further investigated by conducting further sensitivity simulations on this case study. A first suite of proposed simulations would allow for the interaction of the GEOS-Chem aerosols with the radiation scheme within RAMS. A second suite of simulations would include adding dust aerosols which can serve as CCN, GCCN and IN. This set of simulations would allow for the examination of the effects of greater aerosol concentrations in an environment with increased amounts of GCCN and IN. In order to understand the full picture of the impact of aerosols on an MCS-produced precipitation, these elements should be examined.

Part II of this study offers the first evaluation of the impacts of aerosol concentration on the intensity of the derecho by modifying the dynamical pathway promoting the generation of strong surface winds, as well as the intensity of mesovorticies forming at the gust outflow boundary. The findings of this study show that a moderate increase in aerosol concentrations led to a weakening of the derecho while a greater increase in concentrations produced an intensification of the derecho. In order to understand the non-monotonic trend between aerosol loading and the intensity of the derecho, high resolution idealized simulations should be conducted in which a larger suite of aerosol concentration profiles are examined.

Furthermore, the simulations within the study were performed in a heterogeneous model setup, which made the analysis of the tendencies within the momentum equations difficult. This is because the reference state used in the model was not representative of the actual environment of the storm. In order to further examine the sensitivity of the derecho event to changes in aerosol concentration, the acceleration terms within the momentum equations should be analyzed and compared along a trajectory. In order to understand how changes in aerosol concentrations led to the non-monotonic trend in the development of the mesovortices, vorticity budget analysis should be conducted. For the purpose of isolating the signal of the aerosol trend, it is suggested conducting these simulations in an idealized model framework.

5. References

Adams-Selin, R.D., van den Heever, S.C., Johnson, R.H., 2013. Impact of Graupel Parameterization Schemes on Idealized Bow Echo Simulations. Mon. Weather Rev. 141, 1241–1262. doi:10.1175/MWR-D-12-00064.1

Albrecht, B. a, 1989. Aerosols, Cloud Microphysics, and Fractional Cloudiness. Science 245, 1227–1230.

Alexander, G.D., Cotton, W.R., 1998. The Use of Cloud-Resolving Simulations of Mesoscale Convective Systems to Build a Mesoscale Parameterization Scheme. J. Atmos. Sci. 55, 2137–2161. doi:10.1175/1520-0469(1998)055<2137:TUOCRS>2.0.CO;2

Anderson, C.J., Arritt, R.W., 2001. Mesoscale Convective Systems over the United States during the 1997–98 El Niño. Mon. Weather Rev. 129, 2443–2457. doi:10.1175/1520-0493(2001)129<2443:MCSOTU>2.0.CO;2

Anderson, C.J., Arritt, R.W., 1998. Mesoscale Convective Complexes and Persistent Elongated Convective Systems over the United States during 1992 and 1993. Mon. Weather Rev. 126, 578–599. doi:10.1175/1520-0493(1998)126<0578:MCCAPE>2.0.CO;2

Andreae, M.O., Rosenfeld, D., Artaxo, P., Costa, a a, Frank, G.P., Longo, K.M., Silva-Dias, M. a F., 2004. Smoking rain clouds over the Amazon. Science 303, 1337–1342. doi:10.1126/science.1092779

Atkins, N.T., St. Laurent, M., 2009a. Bow Echo Mesovortices. Part II: Their Genesis. Mon. Weather Rev. 137, 1514–1532. doi:10.1175/2008MWR2650.1

Atkins, N.T., St. Laurent, M., 2009b. Bow Echo Mesovortices. Part I: Processes That Influence Their Damaging Potential. Mon. Weather Rev. 137, 1497–1513. doi:10.1175/2008MWR2649.1

Augustine, J. a., Caracena, F., 1994. Lower-Tropospheric Precursors to Nocturnal MCS Development over the Central United States. Weather Forecast. doi:10.1175/1520-0434(1994)009<0116:LTPTNM>2.0.CO;2

Berg, W., L'Ecuyer, T., van den Heever, S., 2008. Evidence for the impact of aerosols on the onset and microphysical properties of rainfall from a combination of satellite observations and cloud-resolving model simulations. J. Geophys. Res. 113, D14S23. doi:10.1029/2007JD009649

Bernardet, L.R., Cotton, W.R., 1998. Multiscale Evolution of a Derecho-Producing Mesoscale Convective System. Mon. Weather Rev. 126, 2991–3015. doi:10.1175/1520-0493(1998)126<2991:MEOADP>2.0.CO;2

Bey, I., Jacob, D.J., Yantosca, R.M., Logan, J. a., Field, B.D., Fiore, A.M., Li, Q.-B., Liu, H.-Y., Mickley, L.J., Schultz, M.G., 2001. Global Modeling of Tropospheric Chemistry with Assimilated Meteorology: Model Description and Evaluation. J. Geophys. Res. 106, 73–95.

doi:10.1029/2001JD000807

Bryan, G.H., Morrison, H., 2012. Sensitivity of a Simulated Squall Line to Horizontal Resolution and Parameterization of Microphysics. Mon. Weather Rev. 140, 202–225. doi:10.1175/MWR-D-11-00046.1

Chung, S.H., Seinfeld, J.H., 2002. Global distribution and climate forcing of carbonaceous aerosols. J. Geophys. Res. 107, 4407. doi:10.1029/2001JD001397

Churchill, D.D., Houze, R.A., 1984. Development and Structure of Winter Monsoon Cloud Clusters On 10 December 1978. J. Atmos. Sci. 41, 933–960. doi:10.1175/1520-0469(1984)041<0933:DASOWM>2.0.CO;2

Coniglio, M.C., Corfidi, S.F., Kain, J.S., 2012. Views on Applying RKW Theory: An Illustration Using the 8 May 2009 Derecho-Producing Convective System. Mon. Weather Rev. 140, 1023–1043. doi:10.1175/MWR-D-11-00026.1

Coniglio, M.C., Corfidi, S.F., Kain, J.S., 2011. Environment and Early Evolution of the 8 May 2009 Derecho-Producing Convective System. Mon. Weather Rev. 139, 1083–1102. doi:10.1175/2010MWR3413.1

Corfidi, S.F., Coniglio, M.C., Cohen, A.E., Mead, C.M., 2015. A proposed revision to the definition of "Derecho." Bull. Am. Meteorol. Soc. 150904101253006. doi:10.1175/BAMS-D-14-00254.1

Cotton, W.R., Bryan, G.H., van den Heever, S.C., 2010. Storm and Cloud Dynamics - The Dynamics of Clouds and Precipitating Mesoscale Systems, International Geophysics. doi:10.1016/S0074-6142(10)09918-3

Cotton, W.R., George, R.L., Wetzel, P.J., McAnelly, R.L., 1983. A Long-Lived Mesoscale Convective Complex. Part I: The Mountain–Generated Component. Mon. Weather Rev. doi:10.1175/1520-0493(1983)111<1893:ALLMCC>2.0.CO;2

Cotton, W.R., Lin, M.-S., McAnelly, R.L., Tremback, C.J., 1989. A Composite Model of Mesoscale Convective Complexes. Mon. Weather Rev. doi:10.1175/1520-0493(1989)117<0765:ACMOMC>2.0.CO;2

Cotton, W.R., Pielke Sr., R. a., Walko, R.L., Liston, G.E., Tremback, C.J., Jiang, H., McAnelly, R.L., Harrington, J.Y., Nicholls, M.E., Carrio, G.G., McFadden, J.P., 2003. RAMS 2001: Current status and future directions. Meteorol. Atmos. Phys. 82, 5–29. doi:10.1007/s00703-001-0584-9

Cotton, W.R., Weaver, J.F., Beitler, B.A., 1995. An Unusual Summertime Downslope Wind Event. Weather Forecast. 10, 786–797.

DeMott, P.J., Prenni, A.J., Liu, X., Kreidenweis, S.M., Petters, M.D., Twohy, C.H., Richardson, M.S., Eidhammer, T., Rogers, D.C., 2010. Predicting global atmospheric ice nuclei distributions and their impacts on climate. Proc. Natl. Acad. Sci. 107, 11217–11222. doi:10.1073/pnas.0910818107

Emanuel, K.A., 1994. Atmospheric Convection. Oxford University.

Evans, C., Weisman, M.L., Bosart, L.F., 2014. Development of an Intense, Warm-Core Mesoscale Vortex Associated with the 8 May 2009 "Super Derecho" Convective Event*. J. Atmos. Sci. 71, 1218–1240. doi:10.1175/JAS-D-13-0167.1

Fritsch, J.M., Kane, R.J., Chelius, C.R., 1986. The Contribution of Mesoscale Convective Weather Systems to the Warm-Season Precipitation in the United States. J. Clim. Appl. Meteorol. 25, 1333–1345. doi:10.1175/1520-0450(1986)025<1333:TCOMCW>2.0.CO;2

Fujita, T.T., 1978. Manual of downburst identi_cation for project NIMROD. Technical report, Dept. of Geophysical Sciences, University of Chicago, Chicago, IL.

Fujita, T.T., Wakimoto, R.M., 1981. Five Scales of Airflow Associated with a Series of Downbursts on 16 July 1980. Mon. Weather Rev. 109, 1438–1456. doi:http://dx.doi.org/10.1175/1520-0493(1981)109<1438:FSOAAW>2.0.CO;2

Grasso, L., Hillger, D.W., Schaaf, C.B., Wang, Z., Brummer, R., DeMaria, R., 2013. Use of MODIS 16-day albedos in generating GOES-R advanced baseline imager imagery. J. Appl. Remote Sens. 7. doi:10.1117/1.JRS.7.073584

Grasso, L.D., 1996. Numerical simulation of the May 15 and April 26, 1991 tornadic thunderstorm. Ph.D. dissertation, Colorado State University, 151 pp. [Available from Department of Atmospheric Science, Colorado State University, Fort Collins, CO 80523.].

Grasso, L.D., Lindsey, D.T., 2011. An example of the use of synthetic 3.9 μm GOES-12 imagery for two-moment microphysical evaluation. Int. J. Remote Sens. 32, 2337–2350. doi:10.1080/01431161003698294

Henze, D.K., Seinfeld, J.H., Ng, N.L., Kroll, J.H., Fu, T.-M., Jacob, D.J., Heald, C.L., 2008. Global modeling of secondary organic aerosol formation from aromatic hydrocarbons: high- vs low-yield pathways. Atmos. Chem. Phys. Discuss. 8, 2405–2420. doi:10.5194/acpd-7-14569-2007

Hinrichs, G., n.d. Amj_Hinrichs.Pdf. Am. Meterological J. 1888, 306–317.

Houze, R. a., Biggerstaff, M.I., Rutledge, S. a., Smull, B.F., 1989. Interpretation of Doppler Weather Radar Displays of Midlatitude Mesoscale Convective Systems. Bull. Am. Meteorol. Soc. doi:10.1175/1520-0477(1989)070<0608:IODWRD>2.0.CO;2

Houze, R.A., 2004. Mesoscale convective systems. Rev. Geophys. 42, RG4003. doi:10.1029/2004RG000150

Igel, M.R., Drager, A.J., van den Heever, S.C., 2014. A CloudSat cloud object partitioning technique and assessment and integration of deep convective anvil sensitivities to sea surface temperature. J. Geophys. Res. Atmos. 119, 10515–10535. doi:10.1002/2014JD021717

Jankov, I., Grasso, L.D., Sengupta, M., Neiman, P.J., Zupanski, D., Zupanski, M., Lindsey, D., Hillger, D.W., Birkenheuer, D.L., Brummer, R., Yuan, H., 2011. An Evaluation of Five

ARW-WRF Microphysics Schemes Using Synthetic GOES Imagery for an Atmospheric River Event Affecting the California Coast. J. Hydrometeorol. 12, 618–633. doi:10.1175/2010JHM1282.1

Jirak, I.L., Cotton, W.R., McAnelly, R.L., 2003. Satellite and Radar Survey of Mesoscale Convective System Development. Mon. Weather Rev. 131, 2428–2449. doi:10.1175/1520-0493(2003)131<2428:SARSOM>2.0.CO;2

Johns, R.H., 1982. A synoptic climatology of northwest flow severe weather outbreaks. Part I: Nature and significance. Mon. Wea. Rev. 110, 1653–1663.

Johns, R.H., Hirt, W.D., 1987. Derechos: Widespread Convectively Induced Windstorms. Weather Forecast. 2, 32–49. doi:10.1175/1520-0434(1987)002<0032:DWCIW>2.0.CO;2

Johnson, R.H., Hamilton, P.J., 1988. The Relationship of Surface Pressure Features to the Precipitation and Airflow Structure of an Intense Midlatitude Squall Line. Mon. Weather Rev. 116, 1444–1473. doi:10.1175/1520-0493(1988)116<1444:TROSPF>2.0.CO;2

Kane, R.J., Chelius, C.R., Fritsch, J.M., 1987. Precipitation Characteristics of Mesoscale Convective Weather Systems. J. Clim. Appl. Meteorol. doi:10.1175/1520-0450(1987)026<1345:PCOMCW>2.0.CO;2

Keene, K.M., Schumacher, R.S., 2013. The Bow and Arrow Mesoscale Convective Structure. Mon. Weather Rev. 141, 1648–1672. doi:10.1175/MWR-D-12-00172.1

Khain, A., Rosenfeld, D., Pokrovsky, A., 2005. Aerosol impact on the dynamics and microphysics of deep convective clouds. Q. J. R. Meteorol. Soc. 131, 2639–2663. doi:10.1256/qj.04.62

Klimowski, B.A., Hjelmfelt. M. R., Bunkers, M.J., 2004. Radar observations of the early evolution of bow echoes. Weather Forecast. 19, 727–734. doi:10.1175/1520-0434(2004)019<0727:ROOTEE>2.0.CO;2

Knupp, K.R., 1987. Downdrafts within High Plains Cumulonimbi. Part I: General Kinematic Structure. J. Atmos. Sci.

Lafore, J.P., Moncrieff, M.W., 1989. A Numerical Investigation of the Organization and Interaction of the Convective and Stratiform Regions of Tropical Squall Lines. J. Atmos. Sci. 46, 521–544. doi:10.1175/1520-0469(1989)046<0521:ANIOTO>2.0.CO;2

Leary, C.A., Houze, R.A., 1979. Melting and Evaporation of Hydrometeors in Precipitation from the Anvil Clouds of Deep Tropical Convection. J. Atmos. Sci. doi:10.1175/1520-0469(1979)036<0669:MAEOHI>2.0.CO;2

Lebo, Z.J., Morrison, H., 2014. Dynamical Effects of Aerosol Perturbations on Simulated Idealized Squall Lines. Mon. Weather Rev. 142, 991–1009. doi:10.1175/MWR-D-13-00156.1

Lee, S.S., Donner, L.J., Phillips, V.T.J., Ming, Y., 2008. Examination of aerosol effects on precipitation in deep convective clouds during the 1997 ARM summer experiment. Q. J. R.

Meteorol. Soc. 134, 1201–1220. doi:10.1002/qj.287

Letcher, T., Cotton, W.R., 2014. The Effect of Pollution Aerosol on Wintertime Orographic Precipitation in the Colorado Rockies Using a Simplified Emissions Scheme to Predict CCN Concentrations. J. Appl. Meteorol. Climatol. 53, 859–872. doi:10.1175/JAMC-D-13-0166.1

Li, G., Wang, Y., Lee, K.H., Diao, Y., Zhang, R., 2009. Impacts of aerosols on the development and precipitation of a mesoscale squall line. J. Geophys. Res. Atmos. 114, 1–18. doi:10.1029/2008JD011581

Lynn, B.H., Khain, A.P., Dudhia, J., Rosenfeld, D., Pokrovsky, A., Seifert, A., 2005. Spectral (Bin) Microphysics Coupled with a Mesoscale Model (MM5). Part II: Simulation of a CaPE Rain Event with a Squall Line. Mon. Weather Rev. 133, 59–71. doi:10.1175/MWR-2841.1

Maddox, R. a., 1980. Meoscale Convective Complexes. Bull. Am. Meteorol. Soc. doi:10.1175/1520-0477(1980)061<1374:MCC>2.0.CO;2

Maddox, R.A., 1983. Large-Scale Meteorological Conditions Associated with Midlatitude, Mesoscale Convective Complexes. Mon. Weather Rev. doi:10.1175/1520-0493(1983)111<1475:LSMCAW>2.0.CO;2

McAnelly, R.L., Cotton, W.R., 1986. Meso-β-scale Characteristics of an Episode of Meso-α-scale Convective Complexes. Mon. Weather Rev. doi:10.1175/1520-0493(1986)114<1740:MSCOAE>2.0.CO;2

Meyers, M.P., Walko, R.L., Harrington, J.Y., Cotton, W.R., 1997. New RAMS cloud microphysics parameterization. Part II: The two-moment scheme. Atmos. Res. 45, 3–39. doi:10.1016/S0169-8095(97)00018-5

Newton, C.W., 1950. STRUCTURE AND MECHANISM OF THE PREFRONTAL SQUALL LINE. J. Meteorol. 7, 210–222. doi:10.1175/1520-0469(1950)007<0210:SAMOTP>2.0.CO;2

Olsson, P.Q., Cotton, W.R., 1997a. Balanced and Unbalanced Circulations in a Primitive Equation Simulation of a Midlatitude MCC. Part I: Analysis of Balance. J. Atmos. Sci. 54, 457–478. doi:10.1175/1520-0469(1997)054<0479:BAUCIA>2.0.CO;2

Olsson, P.Q., Cotton, W.R., 1997b. Balanced and Unbalanced Circulations in a Primitive Equation Simulation of a Midlatitude MCC. Part II: Analysis of Balance. J. Atmos. Sci. 54, 479–497. doi:10.1175/1520-0469(1997)054<0479:BAUCIA>2.0.CO;2

Orlanski, I., 1975. A rational subdivision of scales for atmospheric processes. Am. Meteorol. Soc. 56, 527–530.

Parker, M.D., Johnson, R.H., 2000. Organizational Modes of Midlatitude Mesoscale Convective Systems. Mon. Weather Rev. 128, 3413–3436. doi:10.1175/1520-0493(2001)129<3413:OMOMMC>2.0.CO;2

Petters, M.D., Kreidenweis, S.M., 2007. and Physics A single parameter representation of

hygroscopic growth and cloud condensation nucleus activity. Atmos. Chem. Phys. 7, 1961–1971. doi:10.5194/acp-7-1961-2007

Przybylinksi, R.W., Schaumann, J.S., Cramer, D.T., Atkins, N.T., 2010. The 08 May 2009 Missouri Derecho : Radar Analysis and Warning Implications over Parts of Southwest Missouri, in: 25th Conf. on Severe Local Storms, Denver, CO, Amer. Meteor. Soc., 3B.1.

Rosenfeld, D., Lohmann, U., Raga, G.B., O'Dowd, C.D., Kulmala, M., Fuzzi, S., Reissell, A., Andreae, M.O., 2008. Flood or drought: how do aerosols affect precipitation? Science 321, 1309–13. doi:10.1126/science.1160606

Rotunno, R., Klemp, J.B., Weisman, M.L., 1988. A Theory for Strong, Long-Lived Squall Lines. J. Atmos. Sci. doi:10.1175/1520-0469(1988)045<0463:ATFSLL>2.0.CO;2

Saleeby, S.M., Cotton, W.R., 2008. A Binned Approach to Cloud-Droplet Riming Implemented in a Bulk Microphysics Model. J. Appl. Meteorol. Climatol. 47, 694–703. doi:10.1175/2007JAMC1664.1

Saleeby, S.M., Cotton, W.R., 2004. A Large-Droplet Mode and Prognostic Number Concentration of Cloud Droplets in the Colorado State University Regional Atmospheric Modeling System (RAMS). Part II: Sensitivity to a Colorado Winter Snowfall Event. J. Appl. Meteorol. 43, 182–195. doi:10.1175/JAM2312.1

Saleeby, S.M., van den Heever, S.C., 2013. Developments in the CSU-RAMS Aerosol Model: Emissions, Nucleation, Regeneration, Deposition, and Radiation. J. Appl. Meteorol. Climatol. 52, 2601–2622. doi:10.1175/JAMC-D-12-0312.1

Schmidt, J.M., Cotton, W.R., 1990. Interactions between Upper and Lower Tropospheric Gravity Waves on Squall Line Structure and Maintenance. J. Atmos. Sci. doi:10.1175/1520-0469(1990)047<1205:IBUALT>2.0.CO;2

Schmidt, J.M., Cotton, W.R., 1989. A High Plains Squall Line Associated with Severe Surface Winds. J. Atmos. Sci. doi:10.1175/1520-0469(1989)046<0281:AHPSLA>2.0.CO;2

Seigel, R.B., van den Heever, S.C., Saleeby, S.M., 2013. Mineral dust indirect effects and cloud radiative feedbacks of a simulated idealized nocturnal squall line. Atmos. Chem. Phys. 13, 4467–4485. doi:10.5194/acp-13-4467-2013

Smull, B.F., Houze, R.A., 1987. Rear Inflow in Squall Lines with Trailing Stratiform Precipitation. Mon. Weather Rev. 115, 2869–2889. doi:10.1175/1520-0493(1987)115<2869:RIISLW>2.0.CO;2

Snow, J.T., 1982. A Review of Recent Advances in Tornado Vortex Dynamics. Rev. Geophys. 20, 953–964.

Storer, R.L., van den Heever, S.C., 2013. Microphysical Processes Evident in Aerosol Forcing of Tropical Deep Convective Clouds. J. Atmos. Sci. 70, 430–446. doi:10.1175/JAS-D-12-076.1

Storer, R.L., van den Heever, S.C., Stephens, G.L., 2010. Modeling Aerosol Impacts on

Convective Storms in Different Environments. J. Atmos. Sci. 67, 3904–3915. doi:10.1175/2010JAS3363.1

Sui, C.-H., Li, X., 2005. A Tendency of Cloud Ratio Associated with the Development of Tropical Water and Ice Clouds. Terr. Atmos. Ocean. Sci. 16, 419–434.

Tao, W.K., Chen, J.P., Li, Z., Wang, C., Zhang, C., 2012. Impact of aerosols on convective clouds and precipitation. Rev. Geophys. 50. doi:10.1029/2011RG000369

Tao, W.-K., Li, X., Khain, A., Matsui, T., Lang, S., Simpson, J., 2007. Role of atmospheric aerosol concentration on deep convective precipitation: Cloud-resolving model simulations. J. Geophys. Res. 112. doi:10.1029/2007JD008728

Tao, W.-K., Simpson, J., Sui, C.H., Ferrier, B., Lang, S., Scala, J., Chou, M.D., Pickering, K., 1993. Heating, Moisture, and Water Budgets of Tropical and Midlatitude Squall Lines: Comparisons and Sensitivity to Longwave Radiation. J. Atmos. Sci. doi:10.1175/1520-0469(1993)050<0673:HMAWBO>2.0.CO;2

Tompkins, A.M., 2001. Organization of Tropical Convection in Low Vertical Wind Shears: The Role of Cold Pools. J. Atmos. Sci. 58, 1650–1672. doi:10.1175/1520-0469(2001)058<1650:OOTCIL>2.0.CO;2

Twomey, S., 1977. The Influence of Pollution on the Shortwave Albedo of Clouds. J. Atmos. Sci. doi:10.1175/1520-0469(1977)034<1149:TIOPOT>2.0.CO;2

Twomey, S., 1974. Pollution and the Planetary Albedo. Atmos. Environ. 8, 1251–1256. doi:10.1016/j.atmosenv.2007.10.062

van den Heever, S.C., Carrió, G.G., Cotton, W.R., DeMott, P.J., Prenni, A.J., 2006. Impacts of Nucleating Aerosol on Florida Storms. Part I: Mesoscale Simulations. J. Atmos. Sci. 63, 1752–1775. doi:10.1175/JAS3713.1

van den Heever, S.C., Cotton, W.R., 2007. Urban aerosol impacts on downwind convective storms. J. Appl. Meteorol. Climatol. 46, 828–850. doi:10.1175/JAM2492.1

van den Heever, S.C., Cotton, W.R., 2004. The Impact of Hail Size on Simulated Supercell Storms. J. Atmos. Sci. 61, 1596–1609. doi:10.1175/1520-0469(2004)061<1596:TIOHSO>2.0.CO;2

Velasco, I., Fritsch, J.M., 1987. Mesoscale Convective Complexes in the Americas. J. Geophys. Res. 92, 9591–9613. doi:10.1029/JD092iD08p09591

Wakimoto, R.M., Murphey, H. V., Davis, C.A., Atkins, N.T., 2006. High Winds Generated by Bow Echoes. Part II: The Relationship between the Mesovortices and Damaging Straight-Line Winds. Mon. Weather Rev. 134, 2813–2829. doi:http://dx.doi.org/10.1175/MWR3216.1

Wang, C., 2005. A modeling study of the response of tropical deep convection to the increase of cloud condensation nuclei concentration: 1. Dynamics and microphysics. J. Geophys. Res. 110, D21211. doi:10.1029/2004JD005720

Ward, D., Cotton, W., 2011. A Method for Forecasting Cloud Condensation Nuclei Using Predictions of Aerosol Physical and Chemical Properties from WRF/Chem. J. Appl. Meteorol. Climatol. 50, 1601–1615. doi:10.1175/2011JAMC2644.1

Ward, D.S., Eidhammer, T., Cotton, W.R., Kreidenweis, S.M., 2010. The role of the particle size distribution in assessing aerosol composition effects on simulated droplet activation. Atmos. Chem. Phys. 10, 5435–5447. doi:10.5194/acp-10-5435-2010

Weisman, M.L., 1993. The Genesis of Severe, Long-Lived Bow Echoes. J. Atmos. Sci. 50, 645–670. doi:10.1175/1520-0469(1993)050<0645:TGOSLL>2.0.CO;2

Weisman, M.L., 1992. The Role of Convectively Generated Rear-Inflow Jets in the Evolution of Long-Lived Mesoconvective Systems. J. Atmos. Sci. doi:10.1175/1520-0469(1992)049<1826:TROCGR>2.0.CO;2

Weisman, M.L., Evans, C., Bosart, L., 2013. The 8 May 2009 Superderecho: Analysis of a Real-Time Explicit Convective Forecast. Weather Forecast. 28, 863–892. doi:10.1175/WAF-D-12-00023.1

Weisman, M.L., Trapp, R.J., 2003. Low-Level Mesovortices within Squall Lines and Bow Echoes. Part I: Overview and Dependence on Environmental Shear. Mon. Weather Rev. 131, 2804–2823.

Xu, X., Xue, M., Wang, Y., 2015a. Mesovortices within the 8 May 2009 Bow Echo over the Central United States: Analyses of the Characteristics and Evolution Based on Doppler Radar Observations and a High-Resolution Model Simulation. Mon. Weather Rev. 143, 2266–2290. doi:10.1175/MWR-D-14-00234.1

Xu, X., Xue, M., Wang, Y., 2015b. The Genesis of Mesovortices within a Real-Data Simulation of a Bow Echo System. J. Atmos. Sci. 72, 1963–1986. doi:10.1175/JAS-D-14-0209.1

Yang, M.-J., Houze, R.A.J., 1995. Multicell Squall-Line Structure as a Manifestation of Vertically Trapped Gravity Waves. Mon. Weather Rev. 123, 641–661. doi:10.1175/1520-0493(1995)123<0641:MSLSAA>2.0.CO;2

Appendix A

Surface total aerosol concentration maps of the CLEAN and POLLUTED simulation and vertical cross section along 38N (the latitude which represents a portion of the meridional location of the MCS) at 0630 UTC, the genesis time of the MCS. The 5xPOLLUTED exhibited the same horizontal and vertical relative aerosol distribution as the POLLUTED simulation, however, multiplied by a factor of five. The surface maps show that location of the MCS genesis and development was defined by a transitional zone of lower to higher aerosol concentrations.

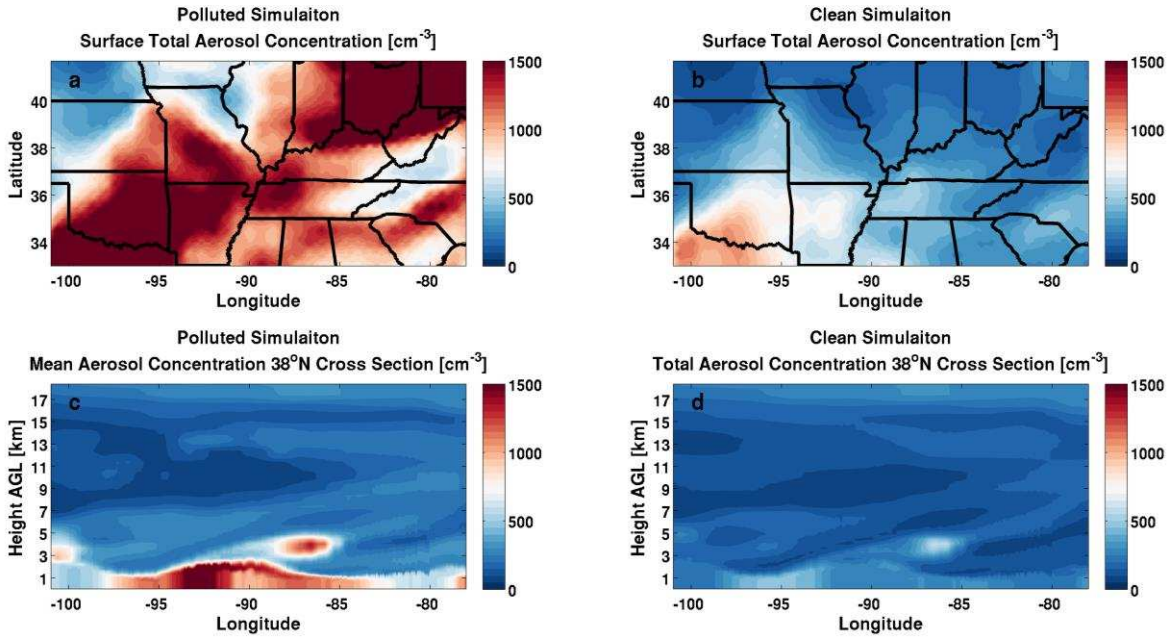

Figure A1: Total aerosol concentration at the surface at 0630 UTC for the (a) POLLUTED simulation and (b) CLEAN simulation and an example of a vertical cross plot along a constant latitude (38°N) for the (c) POLLUTED simulation and (d) CLEAN simulation.

While, the MCS initially developed in a region with lower aerosol concentration (western Kansas), the MCS and propagated east into a region which contained higher aerosol concentrations in both the CLEAN and POLLUTED simulations. Due to the added component of anthropogenic aerosols within the polluted simulation, the increase in aerosol concentration in eastern Kansas is more notable. The cross-section at 38N show that the higher aerosol concentrations are mainly within the boundary layer, and rapidly decrease above 3km AGL.